FACULDADE DE ENGENHARIA DA UNIVERSIDADE DO PORTO

Hydrogen ICE Fuel Injection System: Geometric Modelling, Flow Characterization and Engine Testing

Francisco Margato Gonçalves



Master's degree in Mechanical Engineering

Supervisor: Prof. Dr. Ing. Abel Rouboa

Second Supervisor: Prof. Dr. Ing. Karsten Wittek

October 9, 2026

© Francisco Gonçalves, 2026

Hydrogen ICE Fuel Injection System: Geometric Modelling, Flow Characterization and Engine Testing

Francisco Margato Gonçalves

Master's degree in Mechanical Engineering

October 9, 2026

Resumo

Os motores de combustão interna a hidrogénio necessitam de um sistema de alimentação capaz de controlar e distribuir um combustível gasoso de baixa densidade e elevada compressibilidade em condições de funcionamento transitórias. Esta dissertação estuda o sistema de alimentação de hidrogénio de um motor DEUTZ TCD 3.6 L4 convertido para ignição por faísca, com particular atenção à válvula proporcional 620 B, ao distribuidor rotativo 160 A e aos componentes que ligam o distribuidor às condutas de admissão.

Foi desenvolvido um modelo geométrico para descrever a área de sobreposição do distribuidor rotativo em função da sua posição angular. A geometria ideal apresentou uma área máxima de sobreposição de 72.10 mm^2. A válvula proporcional e o distribuidor rotativo foram posteriormente caracterizados experimentalmente utilizando ar comprimido e um medidor de caudal mássico Coriolis. O distribuidor apresentou uma área efetiva máxima, após correção do caudal residual, de 22.240 mm^2, demonstrando que a área geométrica de sobreposição e a área efetiva de escoamento são grandezas distintas. A válvula proporcional apresentou um início de abertura próximo de 8%, seguido de uma resposta aproximadamente linear da área efetiva. A área efetiva extrapolada para a abertura total foi de 3.513 mm^2, com um coeficiente de descarga de 0.716 e uma histerese reduzida.

Foram também realizados ensaios no motor a diferentes regimes de rotação e cargas para avaliar a influência da geometria da mangueira de ligação, da válvula de retenção, do bocal e do início de injeção. A configuração de referência operou com misturas pobres, verificando-se um aumento da eficiência térmica e uma redução do consumo específico de combustível com o aumento da carga. A redução do diâmetro interno da mangueira teve uma influência mais significativa do que o aumento do seu comprimento, tanto na dinâmica da linha de combustível como na pressão no cilindro. A válvula de retenção revelou também uma função importante no isolamento da linha de combustível relativamente às oscilações de pressão na admissão. A alteração do início de injeção modificou principalmente a posição temporal do fornecimento de combustível, enquanto o faseamento da combustão foi mantido através do ajuste do avanço de ignição.

De forma global, os resultados mostram que o sistema de alimentação deve ser considerado como um sistema dinâmico acoplado e que a geometria dos componentes, por si só, não é suficiente para representar o seu comportamento real. Os dados geométricos, experimentais de caracterização do escoamento e de motor obtidos neste trabalho constituem uma base experimental para o desenvolvimento e modelação futura do sistema.

Palavras-chave: Hidrogénio; motor de combustão interna; sistema de injeção; distribuidor rotativo; injeção de hidrogénio; ensaios de motor.

Abstract

Hydrogen internal combustion engines require a fuel delivery system capable of controlling and distributing a low density and highly compressible gaseous fuel under transient operating conditions. This dissertation investigates the hydrogen fuel delivery system of a converted DEUTZ TCD 3.6 L4 spark ignition engine, with particular focus on the proportional valve 620 B, the rotary distributor 160 A, and the components connecting the distributor to the intake ports.

A geometric model was developed to describe the overlap area of the rotary distributor as a function of its angular position. The ideal geometry resulted in a maximum overlap area of 72.10 mm^2. The proportional valve and rotary distributor were then characterized experimentally using compressed air and a Coriolis mass flow meter. The distributor reached a maximum leakage corrected effective flow area of 22.240 mm^2, showing that geometric overlap and effective flow area represent different quantities. The proportional valve presented an initial opening threshold of approximately 8%, followed by an almost linear effective area response. The extrapolated effective area at full opening was 3.513 mm^2, with a discharge coefficient of 0.716 and limited hysteresis.

Engine tests were subsequently performed over different speeds and loads to evaluate the influence of connection hose geometry, check valve and nozzle configuration, and start of injection. The baseline engine operated under lean conditions, with thermal efficiency increasing and brake specific fuel consumption decreasing as load increased. The engine comparisons showed that reducing the hose inner diameter had a stronger effect on fuel line dynamics and cylinder pressure than increasing its length. The check valve was found to play an important role in isolating the fuel line from intake pressure fluctuations. Changes in start of injection mainly shifted the fuel delivery event, while combustion phasing was maintained through spark timing calibration.

Overall, the results show that the fuel delivery system behaves as a coupled dynamic system and that component geometry alone is insufficient to describe its actual flow behaviour. The obtained geometric, experimental flow characterization, and engine data provide an experimental basis for further development and future numerical modelling of the system.

Keywords: Hydrogen; internal combustion engine; fuel delivery system; rotary distributor; hydrogen injection; engine testing.

The United Nations Sustainable Development Goals

The United Nations **SDG!**s (**SDG!**s) provide a global framework for achieving a better and more sustainable future for all. It includes 17 goals (https://sdgs.un.org/goals) addressing global challenges related to social, economic, and environmental sustainability.

The work developed in this dissertation is most directly related to SDG 7, SDG 9, and SDG 13. The investigation focuses on the geometric and experimental characterization of a hydrogen injection system for an internal combustion engine, together with the evaluation of different system configurations under real engine operating conditions. The resulting experimental knowledge contributes to the development and understanding of hydrogen engine technologies and provides a basis for their further improvement and numerical modelling. In addition, the development of hydrogen based propulsion technologies may support decarbonization strategies when hydrogen is produced through low-carbon energy pathways.

The specific Sustainable Development Goals considered in this work have the following names:

SDG 7 Ensure access to affordable, reliable, sustainable and modern energy for all

SDG 9 Build resilient infrastructure, promote inclusive and sustainable industrialization and foster innovation

SDG 13 Take urgent action to combat climate change and its impacts

SDG	Target	Contribution	Performance Indicators and Metrics
7	7.3	The experimental investigation of the hydrogen engine and its injection system contributes to the understanding of system parameters that affect engine operation and energy efficiency. The engine tests provide experimental information on the relation between operating conditions, hydrogen consumption, and thermal efficiency.	Thermal efficiency and brake specific fuel consumption evaluated over the engine operating map. Maximum measured thermal efficiency of 39.8%.
	7.a	The characterization of the hydrogen injection system supports research and technological development related to the use of hydrogen as an energy carrier in internal combustion engines. Experimental data were obtained for the main metering and distribution components and for the complete system during engine operation.	Experimental effective flow area characteristics of proportional valve 620 B and rotary distributor 160 A, together with engine test data over 11 operating points.
9	9.5	The work contributes to engineering research and technological development through the analytical characterization of the rotary distributor, experimental characterization of the main injection components, and evaluation of different system configurations on the engine. These results provide an experimental basis for the further development and validation of hydrogen injection systems and future numerical models.	Geometric model of distributor 160 A; experimental characterization of proportional valve 620 B and distributor 160 A; and comparative engine testing of hose geometry, check valve and nozzle configuration, and start of injection.
13	13.3	The work contributes to the development of technical knowledge related to hydrogen-based propulsion technologies that may support future climate change mitigation strategies. Hydrogen combustion does not produce carbon dioxide directly from the fuel; however, the overall climate benefit depends on the hydrogen production pathway. The experimental investigation therefore contributes indirectly to the development of technologies that can be integrated into low-carbon energy and transport systems.	Experimental characterization and engine testing of a hydrogen injection system, providing technical knowledge for the development of hydrogen internal combustion engine technologies.

Acknowledgements

I would like to express my sincere gratitude to my supervisor at the University of Porto, Professor Abel Rouboa, for his guidance, support, and for providing me with the opportunity to carry out this work in Germany.

I am also very grateful to my supervisor in Germany, Professor Karsten Wittek, for everything he taught me, for his continuous help throughout this work, and for the opportunities he provided during my stay. I would also like to thank him and his wife Ana Wittek for their kindness, hospitality, and for making me feel welcome from the beginning.

I would like to thank everyone at the laboratory for all their help, support, and, above all, for the friendship and good moments shared during my time there.

A special thanks goes to my family, particularly my father, mother, and sister, as well as to all my grandparents and the rest of my family, for their constant support throughout my academic journey.

Finally, I would like to thank all the friends who accompanied me throughout university, for the experiences, support, and memories shared along the way.

Francisco Margato Gonçalves

"If it moves and it shouldn't, use duct tape.
If it doesn't move and it should, use WD-40"

Unknown

Contents

1 Introduction **1**

1.1 Laboratory 1

1.2 Hydrogen Fueled Engines 2

1.3 Motivation 2

1.4 Project Scope 3

1.5 Dissertation Objectives 3

1.6 Dissertation Structure 4

2 State of the Art **5**

2.1 Internal Combustion Engines 5

2.1.1 Four stroke engine working cycle 6

2.1.2 Sequence of events in a four stroke SI engine 7

2.1.3 Thermochemistry of Internal Combustion Engines 8

2.1.4 Engine Performance Parameters 9

2.1.5 Exhaust Emissions 12

2.2 Hydrogen as a Fuel for Internal Combustion Engines 15

2.2.1 Physical and chemical properties relevant to combustion 15

2.2.2 Stoichiometry and Lambda Range 15

2.2.3 Hydrogen Storage and Safety Considerations 16

2.2.4 Combustion characteristics and Abnormal Phenomena 17

2.2.5 Current state of H2 ICE development 20

2.3 Fuel Injection Systems for Gaseous Fuels in ICE 22

2.3.1 Port Fuel Injection (PFI) 22

2.3.2 Direct Injection (DI) 22

2.3.3 Comparative Analysis of Injection Strategies 23

3 System Description **24**

3.1 The DEUTZ TCD 3.6 L4 Engine 24

3.1.1 Engine specifications and architecture 25

3.1.2 Adaptation for gaseous fuel operation 26

3.2 H_2/Syngas Injection System 27

3.2.1 System architecture and component chain 27

3.2.2 Operating principle: from supply to cylinder 28

3.3 Proportional Valve 28

3.4 Rotary Distributor 29

3.4.1 Distributor 160 A 30

3.5 Connection Hose 31

3.6 Nozzle 32

3.7 Instrumentation and Measurement Systems 33

3.7.1 Pressure and Temperature Measurement 33

3.7.2 Flow Rate, Crank Angle and Torque Measurement 33

3.7.3 Exhaust Gas Analysis 34

4 Geometric Characterization of the Rotary Distributor **35**

4.1 Operating Principle and System Architecture 35

4.2 Geometric Parameter Measurement 37

4.3 Derived Geometric Quantities and Overlap Area Profile 38

4.4 Effect of Machining on the Real Sector Geometry 39

5 Flow Characterization **40**

5.1 Proportional Valve Characterization 41

5.1.1 Effective Flow Area and Linearity 41

5.1.2 Valve Hysteresis 43

5.2 Distributor Characterization 44

5.2.1 Effective Flow Area over the Angular Range 44

5.3 Flow Characterization Summary 46

6 Engine Testing **47**

6.1 Engine Test Facilities 47

6.2 Engine Test Programme 48

6.2.1 VSR002 (Baseline Configuration) 49

6.2.2 VSR004 (Extended Hose Length on Cylinder 4) 49

6.2.3 VSR005 (Reduced Hose Diameter on Cylinder 4) 50

6.2.4 VSR006 (Removal of Check Valve on Cylinder 4) 51

6.2.5 VSR008 (Removal of Check Valve and Nozzle on Cylinder 4) 51

6.2.6 VSR009 (Modified Start of Injection Timing) 52

6.3 Comparative Analysis Structure 52

6.4 Individual Campaign Results 53

6.4.1 VSR002 (Baseline) 53

6.5 Hose Geometry Comparison: VSR002, VSR004 and VSR005 58

6.5.1 High Load: MP010 58

6.6 Check Valve and Nozzle Comparison: VSR002, VSR006 and VSR008 64

6.6.1 High Load: MP010 64

6.7 Injection Timing Comparison: VSR002 and VSR009 70

6.7.1 High Load: MP010 70

7 Conclusions and Future Work **76**

7.1 Conclusions 76

7.2 Future Work 78

References **80**

A Technical Drawings and CAD Models **83**

B Rotary Distributor Overlap Area Calculation Tool **89**

C Analytical Formulation for Effective Flow Area Characterization from Coriolis Measurements **97**

C.1 Measured Variables 97

C.2 Pressure, Density, and Flow Function 98

C.3 Effective Flow Area Calculation 99

C.3.1 Proportional Valve Effective Flow Area 99
C.3.2 Rotary Distributor Effective Flow Area 100
C.4 Proportional Valve Linearization 100
C.5 Valve Hysteresis Evaluation 101
C.6 Proportional Valve Characterization 102
C.7 Rotary Distributor Characterization 103

D Individual Engine Test Campaign Results **106**
D.1 VSR004 (Extended Hose Length) 106
D.2 VSR005 (Reduced Hose Diameter) 109
D.3 VSR006 (Without Check Valve) 113
D.4 VSR008 (Without Check Valve and Nozzle) 116
D.5 VSR009 (Modified Injection Timing) 120

E Additional Comparative Engine Test Results **124**
E.1 Hose Geometry Comparison 124
E.1.1 Low Load: MP001 124
E.1.2 Mid Load: MP005 127
E.2 Check Valve Comparison 130
E.2.1 Low Load: MP001 130
E.2.2 Mid Load: MP005 133
E.3 njection timing Comparison 136
E.3.1 Low Load: MP001 136
E.3.2 Mid Load: MP005 139

List of Figures

2.1 The Daimler-Maybach "Grandfather Clock" engine, displayed at the Mercedes-Benz Museum in Stuttgart. 6

2.2 Four stroke engine cycle. Adapted from [1]. 7

2.3 Examples of P-V diagrams illustrating the indicated work per cycle, for (a) a two stroke cycle engine; (b) a naturally aspirated four stroke cycle engine at part load; (c) a turbocharged four stroke cycle engine at high load. Adapted from [1]. . . . 7

2.4 Sequence of events in four stroke spark ignition engine operating cycle. Adapted from [1]. 8

2.5 Basic geometry of a reciprocating internal combustion engine. Adapted from [1]. 10

2.6 Typical variation of NO, CO, and HC emissions as a function of the relative air fuel ratio (λ). Adapted from [1]. 14

2.7 Typical cylinder and intake manifold pressure traces during a pre-ignition event (solid lines) compared to a regular cycle (dotted lines) [2]. 18

2.8 Typical cylinder and intake pressure traces for a backfiring cycle (solid lines) compared to regular pressure traces (dotted lines) [2]. 19

2.9 Typical cylinder pressure knocking traces [2]. 20

2.10 Toyota liquid hydrogen race car during the 24 Hours of Nürburgring 2026 endurance race. 21

3.1 DEUTZ TCD 3.6 L4. 25

3.2 Spark plug and piezoelectric pressure transducer location. 26

3.3 CAD of the modified cylinder head. 27

3.4 Schematic of the H_2/Syngas injection system architecture and component chain. . 28

3.5 Proportional valve mounted on the test bench. 29

3.6 Distributor 160 A mounted on the engine. 31

3.7 Hoses used in the injection system: natural gas hose (orange) and fuel hose (black). 32

3.8 Injection nozzle and check valve disassembled. 33

4.1 Distributor 160 A disassembled. 36

4.2 Schematic of the overlap area. 37

4.3 CAD model of the stator plate showing the geometric parameters r_1, r_2, and α. . 37

4.4 Computed overlap area profile $A(\theta_w)$ for distributor 160 A as a function of toothed wheel angle. 39

5.1 Experimental setup used for the flow characterization tests. 41

5.2 Effective flow area of proportional valve 620 B as a function of commanded position. 42

5.3 Opening and closing effective flow area characteristics and hysteresis of proportional valve 620 B. 43

5.4 Leakage corrected effective flow area of distributor 160 A as a function of input shaft angle. 45

6.1 External view of the engine test facility. 48

6.2 Engine monitoring and control room. 48

6.3 Gas supply and control system. 48

6.4 Engine test bench in the baseline configuration used for campaign VSR002. . . . 49

6.5 Extended connection hose installed on cylinder 4 for campaign VSR004. 50

6.6 Reduced diameter connection hose installed on cylinder 4 for campaign VSR005. 50

6.7 Check valve spring and spring pre-tensioner removed from the nozzle of cylinder 4 for campaign VSR006. 51

6.8 Connection hose on cylinder 4 with nozzle and check valve removed for campaign VSR008. 52

6.9 Contour map of brake specific fuel consumption as a function of engine speed and IMEP for campaign VSR002 (baseline configuration). 54

6.10 Contour map of brake specific NO_x emissions as a function of engine speed and IMEP for campaign VSR002 (baseline configuration). 55

6.11 Contour map of thermal efficiency as a function of engine speed and IMEP for campaign VSR002 (baseline configuration). 56

6.12 Contour map of lambda as a function of engine speed and IMEP for campaign VSR002 (baseline configuration). 57

6.13 Contour map of injected hydrogen mass per cycle as a function of engine speed and IMEP for campaign VSR002 (baseline configuration). 58

6.14 Comparison of the distributor upstream pressure traces for MP010. 59

6.15 Comparison of the injection line pressure traces on cylinder 4 for MP010. 60

6.16 Comparison of the intake manifold pressure traces on cylinder 4 for MP010. . . . 61

6.17 Comparison of the in-cylinder pressure traces on cylinder 4 for MP010. 62
6.18 Comparison of the exhaust manifold pressure traces on cylinder 4 for MP010. . . 63
6.19 Comparison of the distributor upstream pressure traces for MP010. 65
6.20 Comparison of the injection line pressure traces on cylinder 4 for MP010. 66
6.21 Comparison of the intake manifold pressure traces on cylinder 4 for MP010. . . . 67
6.22 Comparison of the in-cylinder pressure traces on cylinder 4 for MP010. 68
6.23 Comparison of the exhaust manifold pressure traces on cylinder 4 for MP010. . . 69
6.24 Comparison of the distributor upstream pressure traces for MP010. 71
6.25 Comparison of the injection line pressure traces on cylinder 4 for MP010. 72
6.26 Comparison of the intake manifold pressure traces on cylinder 4 for MP010. . . . 73
6.27 Comparison of the in-cylinder pressure traces on cylinder 4 for MP010. 74
6.28 Comparison of the exhaust manifold pressure traces on cylinder 4 for MP010. . . 75

A.1 Isometric CAD view of the proportional valve 620 B. 83
A.2 Sectional CAD view of the proportional valve 620 B. 84
A.3 Sectional technical drawing of the proportional valve 620 B. 84
A.4 Isometric CAD view of the rotary distributor 160 A. 85
A.5 Sectional CAD view of the rotary distributor 160 A. 85
A.6 Sectional technical drawing of the rotary distributor 160 A. 86
A.7 Technical drawing of the stator plate. 87
A.8 Technical drawing of the nozzle system. 88

B.1 Overlap area for three values of relative angular displacement δ. *Left:* perfect alignment ($\delta = 0°$, $A = A_{\max}$). *Centre:* partial overlap ($\delta = 15°$). *Right:* fully closed ($|\delta| \geq \alpha = 24°, A = 0$). 90
B.2 Geometry sheet of the calculation tool. 91

C.1 Proportional valve characterization data. 103
C.2 Proportional valve hysteresis characterization data. 103
C.3 Rotary distributor measurement data and results. 105

D.1 Contour map of brake specific fuel consumption as a function of engine speed and IMEP for campaign VSR004 (Extended Hose Length). 107
D.2 Contour map of brake specific NO_x emissions as a function of engine speed and IMEP for campaign VSR004 (Extended Hose Length). 108

D.3 Contour map of thermal efficiency as a function of engine speed and IMEP for campaign VSR004 (Extended Hose Length). 108

D.4 Contour map of lambda as a function of engine speed and IMEP for campaign VSR004 (Extended Hose Length). 109

D.5 Contour map of injected hydrogen mass per cycle as a function of engine speed and IMEP for campaign VSR004 (Extended Hose Length). 109

D.6 Contour map of brake specific fuel consumption as a function of engine speed and IMEP for campaign VSR005 (Reduced Hose Diameter). 111

D.7 Contour map of brake specific NO_x emissions as a function of engine speed and IMEP for campaign VSR005 (Reduced Hose Diameter). 111

D.8 Contour map of thermal efficiency as a function of engine speed and IMEP for campaign VSR005 (Reduced Hose Diameter). 112

D.9 Contour map of lambda as a function of engine speed and IMEP for campaign VSR005 (Reduced Hose Diameter). 112

D.10 Contour map of injected hydrogen mass per cycle as a function of engine speed and IMEP for campaign VSR005 (Reduced Hose Diameter). 113

D.11 Contour map of brake specific fuel consumption as a function of engine speed and IMEP for campaign VSR006 (Without Check Valve). 114

D.12 Contour map of brake specific NO_x emissions as a function of engine speed and IMEP for campaign VSR006 (Without Check Valve). 115

D.13 Contour map of thermal efficiency as a function of engine speed and IMEP for campaign VSR006 (Without Check Valve). 115

D.14 Contour map of lambda as a function of engine speed and IMEP for campaign VSR006 (Without Check Valve). 116

D.15 Contour map of injected hydrogen mass per cycle as a function of engine speed and IMEP for campaign VSR006 (Without Check Valve). 116

D.16 Contour map of brake specific fuel consumption as a function of engine speed and IMEP for campaign VSR008 (Without Check Valve and Nozzle). 118

D.17 Contour map of brake specific NO_x emissions as a function of engine speed and IMEP for campaign VSR008 (Without Check Valve and Nozzle). 118

D.18 Contour map of thermal efficiency as a function of engine speed and IMEP for campaign VSR008 (Without Check Valve and Nozzle). 119

D.19 Contour map of lambda as a function of engine speed and IMEP for campaign VSR008 (Without Check Valve and Nozzle). 119

D.20 Contour map of injected hydrogen mass per cycle as a function of engine speed and IMEP for campaign VSR008 (Without Check Valve and Nozzle). 120

D.21 Contour map of brake specific fuel consumption as a function of engine speed and IMEP for campaign VSR009 (Modified Injection Timing). 121

D.22 Contour map of brake specific NO_x emissions as a function of engine speed and IMEP for campaign VSR009 (Modified Injection Timing). 122

D.23 Contour map of thermal efficiency as a function of engine speed and IMEP for campaign VSR009 (Modified Injection Timing). 122

D.24 Contour map of lambda as a function of engine speed and IMEP for campaign VSR009 (Modified Injection Timing). 123

D.25 Contour map of injected hydrogen mass per cycle as a function of engine speed and IMEP for campaign VSR009 (Modified Injection Timing). 123

E.1 Comparison of the distributor upstream pressure traces for MP001. 125

E.2 Comparison of the injection line pressure traces on cylinder 4 for MP001. 125

E.3 Comparison of the intake manifold pressure traces on cylinder 4 for MP001. . . . 126

E.4 Comparison of the in-cylinder pressure traces on cylinder 4 for MP001. 126

E.5 Comparison of the exhaust manifold pressure traces on cylinder 4 for MP001. . . 127

E.6 Comparison of the distributor upstream pressure traces for MP005. 128

E.7 Comparison of the injection line pressure traces on cylinder 4 for MP005. 128

E.8 Comparison of the intake manifold pressure traces on cylinder 4 for MP005. . . . 129

E.9 Comparison of the in-cylinder pressure traces on cylinder 4 for MP005. 129

E.10 Comparison of the exhaust manifold pressure traces on cylinder 4 for MP005. . . 130

E.11 Comparison of the distributor upstream pressure traces for MP001. 131

E.12 Comparison of the injection line pressure traces on cylinder 4 for MP001. 131

E.13 Comparison of the intake manifold pressure traces on cylinder 4 for MP001. . . . 132

E.14 Comparison of the in-cylinder pressure traces on cylinder 4 for MP001. 132

E.15 Comparison of the exhaust manifold pressure traces on cylinder 4 for MP001. . . 133

E.16 Comparison of the distributor upstream pressure traces for MP005. 134

E.17 Comparison of the injection line pressure traces on cylinder 4 for MP005. 134

E.18 Comparison of the intake manifold pressure traces on cylinder 4 for MP005. . . . 135

E.19 Comparison of the in-cylinder pressure traces on cylinder 4 for MP005. 135

E.20 Comparison of the exhaust manifold pressure traces on cylinder 4 for MP005. . . 136

E.21 Comparison of the distributor upstream pressure traces for MP001. 137

E.22 Comparison of the injection line pressure traces on cylinder 4 for MP001. 137

E.23 Comparison of the intake manifold pressure traces on cylinder 4 for MP001. . . . 138

E.24 Comparison of the in-cylinder pressure traces on cylinder 4 for MP001. 138

E.25 Comparison of the exhaust manifold pressure traces on cylinder 4 for MP001. . . 139
E.26 Comparison of the distributor upstream pressure traces for MP005. 140
E.27 Comparison of the injection line pressure traces on cylinder 4 for MP005. 140
E.28 Comparison of the intake manifold pressure traces on cylinder 4 for MP005. . . . 141
E.29 Comparison of the in-cylinder pressure traces on cylinder 4 for MP005. 141
E.30 Comparison of the exhaust manifold pressure traces on cylinder 4 for MP005. . . 142

List of Tables

2.1 Representative properties of hydrogen, gasoline, and diesel under ambient reference conditions 15

3.1 Technical specifications of the DEUTZ TCD 3.6 L4 base engine 25

3.2 Instrumentation used during the experimental campaign 34

4.1 Measured geometric and kinematic parameters of the Distributor 160 A 38

4.2 Derived geometric quantities of the Distributor 160 A 38

6.1 Engine operating points used in each test campaign 48

B.1 Geometric parameters and derived quantities of the Distributor 160 A 92

B.2 Calculated Overlap Area Values as a Function of Wheel Angle 92

List of Acronyms

A	Geometric overlap area
A_s	Area of an annular sector
$A_{\max}$	Maximum geometric overlap area
A_{eff}	Effective flow area
$A_{\text{eff,closed}}$	Effective flow area at the closed distributor position
$A_{\text{eff,off}}$	Leakage corrected effective flow area
ATDC	After Top Dead Center
BDC	Bottom Dead Center
BMEP	Brake Mean Effective Pressure
BSFC	Brake Specific Fuel Consumption
BTDC	Before Top Dead Center
BTE	Brake Thermal Efficiency
C_d	Discharge coefficient
CA	Crank Angle
CA50	Crank Angle at 50% Mass Fraction Burned
CAD	Computer Aided Design
CH_4	Methane
CI	Compression Ignition
CO	Carbon monoxide
CO_2	Carbon dioxide
dCA	Degrees Crank Angle
DI	Direct Injection
ECU	Engine Control Unit
FMEP	Friction Mean Effective Pressure
H_2	Hydrogen
H_2O	Water
i	Internal gear ratio
ICE	Internal Combustion Engine
IMEP	Indicated Mean Effective Pressure
LHV	Lower Heating Value
LH_2	Liquid Hydrogen
m_a	Inducted air mass
$\dot{m}$	Mass flow rate
$\dot{m}_f$	Fuel mass flow rate
MEP	Mean Effective Pressure
MFB50	50% Mass Fraction Burned
MP	Measurement Point

N	Engine rotational speed
N_2	Nitrogen
NO	Nitrogen monoxide
NO_x	Nitrogen oxides
O_2	Oxygen
P	Brake power
p	Pressure
p_{amb}	Ambient pressure
p_{up}	Upstream absolute pressure
p_{dw}	Downstream absolute pressure
$p_{\text{r,up}}$	Upstream gauge pressure
$p_{\text{r,dw}}$	Downstream gauge pressure
PFI	Port Fuel Injection
PN	Particle Number
PR	Pressure ratio used in the compressible flow calculation
PR_{meas}	Measured downstream to upstream pressure ratio
PR_{crit}	Critical pressure ratio
r_c	Geometric compression ratio
r_1	Inner radius of the annular sector
r_2	Outer radius of the annular sector
R	Specific gas constant
R^2	Coefficient of determination
rpm	Revolutions Per Minute
SI	Spark Ignition
SOI	Start of Injection
T	Engine torque
T_{gas}	Gas temperature
TDC	Top Dead Center
V	Cylinder volume
V_c	Clearance volume
V_d	Displaced volume
W_i	Indicated work per cycle
x_b	Mass fraction burned
α	Sector angular width
$\Delta\alpha$	Angular overlap between rotor and stator windows
δ	Relative angular displacement between rotor and stator windows
γ	Ratio of specific heats
η_m	Mechanical efficiency
η_v	Volumetric efficiency
λ	Relative air fuel ratio
ϕ	Equivalence ratio
ρ_{up}	Upstream air density
$\rho_{a,i}$	Intake manifold air density
ψ	Compressible flow function
θ_w	Toothed wheel angular position
θ_r	Rotor angular position
$\Delta\theta_{w,\text{inj}}$	Distributor injection window in the toothed wheel reference

Chapter 1

Introduction

The global energy sector is undergoing a transition towards lower greenhouse gas emissions and reduced dependence on fossil fuels. Despite this transition, internal combustion engines (ICEs) remain an important technology for heavy duty, off road, industrial, and stationary power applications due to their high power density, reliability, and established manufacturing infrastructure. In this context, hydrogen (H_2) represents a potential alternative energy carrier for reducing the carbon emissions associated with conventional combustion engines.

The use of gaseous fuels in engines originally designed for liquid fuel injection introduces additional challenges for the fuel delivery system. Hydrogen is characterized by a low density, high diffusivity, wide flammability range, and high laminar flame speed. These properties require a fuel system capable of supplying the required fuel quantity while maintaining adequate control of the injection event and mixture formation.

This dissertation investigates a mechanically controlled hydrogen fuel delivery system developed for a converted industrial engine. The work combines experimental flow characterization of the main fuel metering and distribution components with engine testing under different fuel system configurations. The objective is to characterize the behaviour of the proposed system and to assess how selected hardware and injection parameters influence fuel delivery, pressure dynamics, mixture preparation, and engine operation.

1.1 Laboratory

The research presented in this dissertation was conducted at the Piston Machine Laboratory (*Labor für Kolbenmaschinen*, KMH) of Hochschule Heilbronn (HHN), Germany, within the framework of an international collaboration with the Faculty of Engineering of the University of Porto (FEUP). The laboratory provides the experimental infrastructure required for the development and testing of industrial internal combustion engines operating with gaseous fuels. The available facilities include engine test cells, data acquisition systems, and dedicated equipment for the preparation and control of gaseous fuel supply systems.

The experimental facilities at KMH enabled both the component flow characterization and the subsequent engine test campaigns performed in this work.

1.2 Hydrogen Fueled Engines

The use of hydrogen in spark ignition (SI) engines offers the possibility of achieving high thermal efficiency while eliminating carbon dioxide emissions associated with the fuel itself at the point of combustion. Under sufficiently lean operating conditions, hydrogen combustion can also achieve low nitrogen oxide (NO_x) emissions. However, the transition from liquid to gaseous fuel injection introduces important challenges related to mixture preparation, engine breathing, and combustion stability.

The low volumetric energy density of gaseous hydrogen means that, in Port Fuel Injection (PFI) systems, part of the intake volume that would otherwise be occupied by air is displaced by fuel. This can reduce the air mass available for combustion and therefore limit engine power density. Hydrogen also presents a wide flammability range, low ignition energy, and a high flame propagation rate. These properties can increase the sensitivity of the engine to abnormal combustion phenomena, including pre-ignition and intake backfire, depending on the mixture, temperature, and operating conditions.

The fuel delivery system must therefore provide adequate control of both the supplied hydrogen quantity and the timing of the fuel delivery event. The ability to deliver the required fuel mass within the available crank angle (CA) window is important for mixture formation, cylinder filling, combustion stability, and repeatable engine operation.

1.3 Motivation

The use of hydrogen in internal combustion engines requires a fuel delivery system capable of accurately controlling and distributing a gaseous fuel over a wide range of engine operating conditions. Compared with liquid fuels, the low density and high compressibility of hydrogen make the flow behaviour of the delivery system particularly sensitive to restrictions, component geometry, and pressure wave propagation.

The fuel delivery concept investigated in this work combines a proportional metering valve with a mechanical rotary distributor. The performance of this system depends not only on the individual flow capacity of these components, but also on the interaction between the distributor, connection hoses, check valves, nozzles, and intake system. Changes in these elements can modify the transient pressure response and the temporal delivery of hydrogen, with possible consequences for mixture formation and cylinder operation.

Experimental characterization is therefore required to determine the flow behaviour of the main components and to assess the sensitivity of the complete system to relevant hardware and operating parameters. The resulting knowledge supports the evaluation of the proposed hydrogen

delivery concept and the identification of configurations that provide stable and repeatable fuel delivery during engine operation.

1.4 Project Scope

The scope of this dissertation comprises the experimental characterization of the hydrogen fuel delivery system developed for a converted DEUTZ TCD 3.6 L4 engine and the evaluation of selected system modifications during engine operation.

The first part of the work consists of the flow characterization of the Mengesteller[1] 620 B proportional valve and the Verteiler[2] 160 A rotary distributor using compressed air. The proportional valve is characterized in terms of effective flow area, linearity, and hysteresis, while the distributor effective flow area is determined as a function of its input shaft angle.

The second part comprises a series of engine test campaigns in which selected parameters of the hydrogen delivery system are modified. The investigated changes include the length and internal diameter of the connection hose, the presence of the check valve and nozzle, and the start of injection. Their influence is evaluated through fuel system, intake manifold, exhaust manifold, and in-cylinder pressure measurements, together with the main engine operating and performance parameters.

The work is focused on the experimental characterization of the investigated fuel delivery components and on the assessment of the selected fuel system configurations over the investigated engine speed and load range.

1.5 Dissertation Objectives

The main objectives of this dissertation are:

- To derive a geometric model describing the variation of the overlap area within the mechanical rotary distributor as a function of its angular position.
- To experimentally characterize the flow behaviour of the proportional valve and the mechanical rotary distributor, including the relationship between operating position and effective flow area and, for the proportional valve, its linearity and hysteresis.
- To evaluate the influence of connection hose geometry, check valve and nozzle configuration, and start of injection on the pressure dynamics of the hydrogen delivery system and on the resulting engine operation.
- To assess the main mixture, performance, and emission parameters over the investigated engine speed and load range.

[1] *Mengesteller* is the German term for *fuel metering unit*.
[2] *Verteiler* is the German term for *distributor*.

1.6 Dissertation Structure

This dissertation is organized into seven chapters. Chapter 1 introduces the motivation, scope, and objectives of the work. Chapter 2 presents the relevant background on internal combustion engines, hydrogen combustion, and gaseous fuel injection systems. Chapter 3 describes the engine, hydrogen fuel delivery system, and experimental instrumentation. Chapter 4 presents the geometric characterization of the rotary distributor, while Chapter 5 describes the experimental flow characterization of the proportional valve and rotary distributor. Chapter 6 presents the engine test programme and the comparison of the investigated fuel delivery system configurations. Finally, Chapter 7 summarizes the main conclusions and presents recommendations for future work.

Chapter 2

State of the Art

This chapter establishes the theoretical foundation and reviews the existing literature necessary to contextualize the experimental study of a rotary gas distributor and hydrogen fuel delivery system for internal combustion engines.

It begins by addressing the operational principles of internal combustion engines, focusing on the four stroke cycle, performance indicators, and the nature of combustion and emissions in spark ignition systems. Following this baseline, the study examines the application of hydrogen as a fuel, highlighting how its properties influence the combustion process and the current state of research regarding its use on ICEs.

The third part of this review focuses on fuel delivery technologies, particularly Port Fuel Injection (PFI) and Direct Injection (DI).

2.1 Internal Combustion Engines

Internal combustion engines (ICE) are energy conversion systems that transform the chemical energy of a fuel oxidizer mixture into mechanical work through a sequence of thermodynamic processes occurring within a variable volume combustion chamber [1]. The developmental history of these units began in the late 19th century, with significant milestones including the spark ignition engine developed by Nicolaus Otto in 1876 and the compression ignition engine invented by Rudolf Diesel in 1892. A primary example of early engineering is the high speed engine developed by Gottlieb Daimler and Wilhelm Maybach, known as the "Grandfather Clock" due to its vertical orientation, as shown in Figure 2.1.

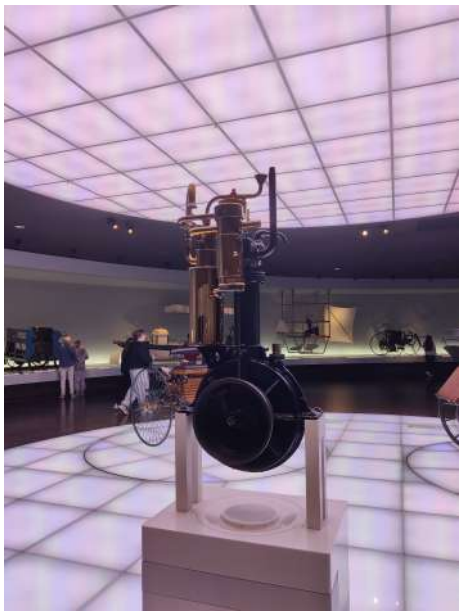


Figure 2.1: The Daimler-Maybach "Grandfather Clock" engine, displayed at the Mercedes-Benz Museum in Stuttgart.

These systems are fundamentally categorized by their ignition mechanism: Spark Ignition (SI) engines, in which combustion is initiated by an electrical discharge at the spark plug, and Compression Ignition (CI) engines, where fuel is injected into high temperature air to undergo spontaneous autoignition [1, 2]. Modern adaptations of these architectures focus on carbon free energy carriers like hydrogen to mitigate environmental impacts while utilizing existing industrial manufacturing frameworks [3, 4].

2.1.1 Four stroke engine working cycle

The four stroke cycle is the operating principle adopted by most reciprocating internal combustion engines. One complete cycle requires two crankshaft revolutions (720°), during which each cylinder produces one power stroke [1]. The cycle consists of four successive strokes, illustrated in Figure 2.2.

1. **Intake Stroke:** The cycle begins at Top Dead Center (TDC). As the piston moves towards Bottom Dead Center (BDC), the intake valve opens and fresh air or an air fuel mixture enters the cylinder due to the pressure difference between the intake system and the cylinder.

2. **Compression Stroke:** After reaching BDC, both valves remain closed while the piston moves towards TDC. The trapped charge is compressed, increasing its pressure and temperature before combustion.

3. **Expansion (Power) Stroke:** Combustion is initiated close to TDC. The combustion products expand and force the piston towards BDC, producing the useful work delivered to the crankshaft.

4. **Exhaust Stroke:** The exhaust valve opens before BDC, allowing the rapid release of combustion gases during the blowdown process. The piston then moves towards TDC, expelling the remaining exhaust gases and completing the cycle.

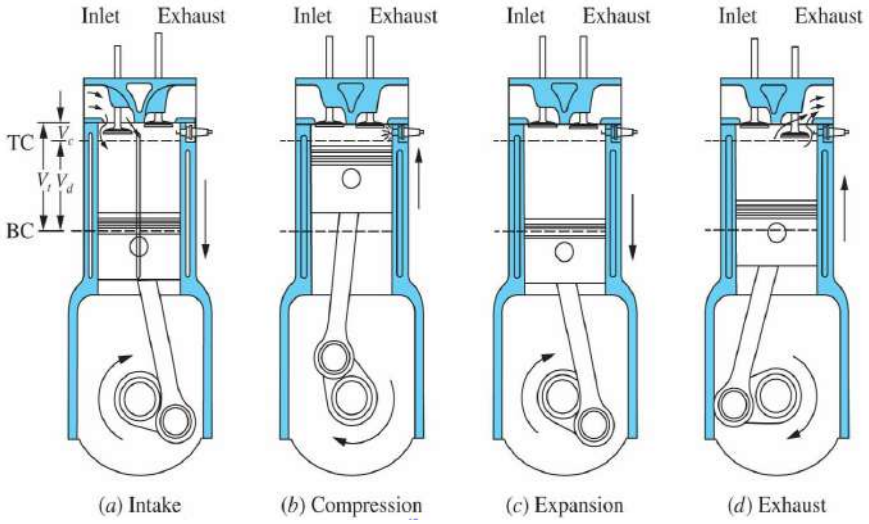


Figure 2.2: Four stroke engine cycle. Adapted from [1].

The evolution of the in-cylinder pressure during the complete engine cycle can be represented by the pressure volume (P–V) diagram shown in Figure 2.3. The enclosed area represents the indicated work produced during one cycle, while the different processes correspond to intake, compression, combustion and expansion, and exhaust. The pressure–volume diagram also provides the basis for determining the indicated work of the cycle, which is used to calculate the Indicated Mean Effective Pressure discussed in Section 2.1.4.3.

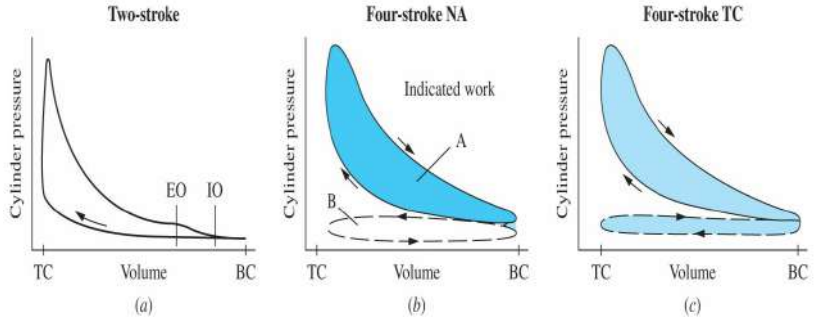


Figure 2.3: Examples of P-V diagrams illustrating the indicated work per cycle, for (a) a two stroke cycle engine; (b) a naturally aspirated four stroke cycle engine at part load; (c) a turbocharged four stroke cycle engine at high load. Adapted from [1].

2.1.2 Sequence of events in a four stroke SI engine

The sequence and timing of the mechanical and thermodynamic events determine the combustion process and engine performance. In spark ignition engines, combustion is initiated by an electrical

discharge at the spark plug, typically between 10° and 40° before Top Dead Center (BTDC) [1]. After ignition, a flame kernel is formed and develops into a turbulent flame front that propagates through the combustion chamber. Since flame propagation requires a finite time, combustion is completed over approximately 40° to 60° crank angle degrees.

Engine efficiency depends on the combustion phasing. Maximum efficiency is generally achieved when approximately 50% of the fuel mass has burned (MFB50) between 8° and 10° after Top Dead Center (ATDC), providing a favourable balance between expansion work and peak cylinder pressure [1, 4]. In Figure 2.4 it's represented the sequence of events in four stroke spark ignition engine operating cycle, with cylinder pressure p (solid line, firing cycle; dashed line, motored cycle), cylinder volume V/V_{max}, and mass fraction burned x_b are plotted against crank angle.

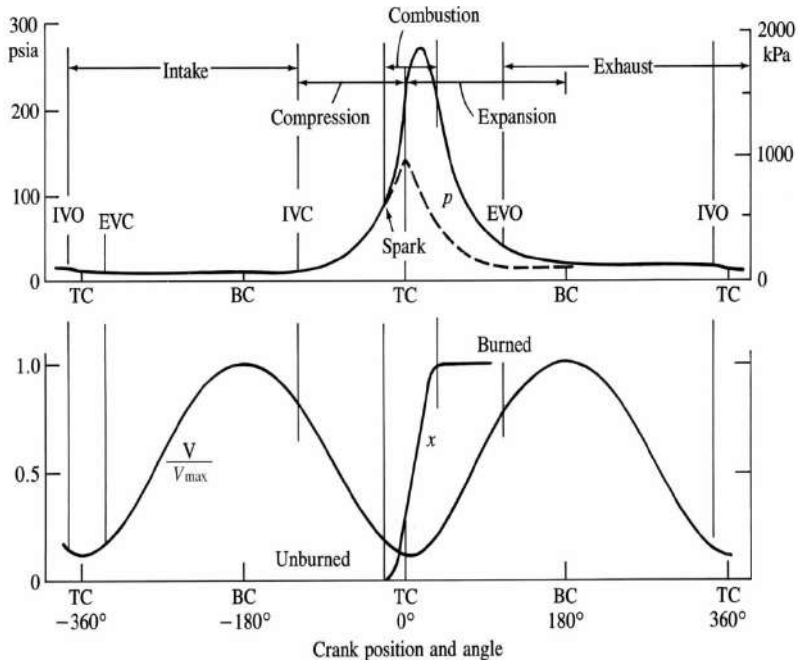


Figure 2.4: Sequence of events in four stroke spark ignition engine operating cycle. Adapted from [1].

2.1.3 Thermochemistry of Internal Combustion Engines

Combustion is governed by the stoichiometric relationship between the fuel and the oxidizer. Air is approximated as a mixture containing 21% oxygen (O_2) and 79% nitrogen (N_2) by volume. Consequently, each mole of oxygen is accompanied by 3.77 moles of nitrogen [1]. For a generic hydrocarbon fuel, represented by C_aH_b, the stoichiometric combustion reaction is

$$C_aH_b + \left(a + \frac{b}{4}\right)(O_2 + 3.77N_2) \rightarrow aCO_2 + \frac{b}{2}H_2O + 3.77\left(a + \frac{b}{4}\right)N_2 \tag{2.1}$$

The mixture composition is commonly described by the relative air fuel ratio (λ) or, equivalently, by the equivalence ratio ($\phi = 1/\lambda$).

For hydrogen combustion, the absence of carbon simplifies the overall reaction and water becomes the primary combustion product. However, nitrogen oxides may still be formed because atmospheric nitrogen reacts with oxygen at high combustion temperatures.

The chemical energy available from the fuel is expressed by its Lower Heating Value (LHV), which represents the energy released during complete combustion excluding the latent heat associated with water vapour condensation [3].

2.1.4 Engine Performance Parameters

Engine performance is evaluated using standardized parameters that enable comparisons between engines with different sizes, operating conditions, and configurations. These parameters describe the engine's ability to produce work, convert the chemical energy of the fuel into useful mechanical power, and exchange gases during the operating cycle [1].

2.1.4.1 Geometric Compression Ratio (r_c)

The geometric compression ratio is one of the main design parameters of an internal combustion engine, as it directly influences the thermal efficiency of the cycle. It is defined as the ratio between the maximum cylinder volume, corresponding to the piston at Bottom Dead Center (BDC), and the minimum cylinder volume, corresponding to the piston at Top Dead Center (TDC), as illustrated in Figure 2.5 [1].

$$r_c = \frac{V_d + V_c}{V_c} \tag{2.2}$$

where V_d is the displaced volume and V_c is the clearance volume.

Increasing the compression ratio improves the theoretical thermal efficiency of the cycle. In spark ignition engines, however, the maximum compression ratio is limited by the onset of abnormal combustion, particularly knock [1]. The engine used in the present work operates with a geometric compression ratio of 12.15:1, selected for hydrogen operation [3].

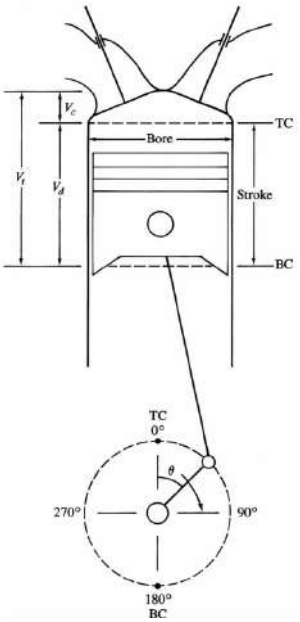


Figure 2.5: Basic geometry of a reciprocating internal combustion engine. Adapted from [1].

2.1.4.2 Torque and Power

Torque (T) represents the rotational effort produced by the engine, while power (P) corresponds to the rate at which this work is delivered [1]. During engine testing, brake torque is measured using a dynamometer coupled to the crankshaft. In the present work, an eddy current brake is used to control the engine load while simultaneously measuring the output torque [3].

Brake power is calculated from the measured torque and engine speed according to

$$P = 2\pi NT \tag{2.3}$$

where N is the crankshaft rotational speed expressed in revolutions per second.

The maximum brake power that can be produced depends on the amount of fresh charge inducted into the cylinder and on the efficiency of the combustion process [1].

2.1.4.3 Mean Effective Pressure (MEP)

Mean Effective Pressure (MEP) is a performance parameter that relates the work produced during one engine cycle to the engine displaced volume. Unlike power, it is independent of engine size, making it suitable for comparing different engines and operating conditions [1].

The indicated work corresponds to the area enclosed by the compression and expansion processes in the pressure volume diagram presented in Figure 2.3. This indicated work can be expressed as the integral of the cylinder pressure over the volume variation throughout the cycle.

The Indicated Mean Effective Pressure (IMEP) is therefore defined as

$$IMEP = \frac{W_i}{V_d} = \frac{1}{V_d} \oint p\,dV \tag{2.4}$$

where W_i is the indicated work per cycle and V_d is the displaced volume.

Although IMEP is expressed in units of pressure, it does not represent the actual pressure inside the cylinder at any instant. Instead, it is an equivalent constant pressure that would produce the same indicated work if it acted uniformly on the piston during the expansion stroke [1, 5].

Three forms of mean effective pressure are commonly distinguished:

- **Indicated Mean Effective Pressure (IMEP):** Represents the work produced by the combustion process inside the cylinder.
- **Brake Mean Effective Pressure (BMEP):** Represents the useful work available at the crankshaft after mechanical losses.
- **Friction Mean Effective Pressure (FMEP):** Represents the work required to overcome mechanical friction, pumping losses, and auxiliary components [1].

These quantities are related by

$$BMEP = IMEP - FMEP \tag{2.5}$$

The mechanical efficiency of the engine is defined as

$$\eta_m = \frac{BMEP}{IMEP} \tag{2.6}$$

which represents the fraction of the indicated work delivered as useful brake work.

2.1.4.4 Efficiency and Fuel Consumption

Brake Thermal Efficiency (BTE) expresses the fraction of the fuel chemical energy converted into useful brake power. Based on the Lower Heating Value (LHV), it is defined as

$$BTE = \frac{P}{\dot{m}_f LHV} \tag{2.7}$$

where $\dot{m}_f$ is the fuel mass flow rate [1].

Brake Specific Fuel Consumption (BSFC) represents the fuel mass required to produce one unit of brake power and is given by

$$BSFC = \frac{\dot{m}_f}{P} \tag{2.8}$$

Since both parameters are inversely related, an increase in brake thermal efficiency results in a reduction of brake specific fuel consumption [1, 6].

2.1.4.5 Volumetric Efficiency and Turbocharging

Volumetric efficiency (η_v) quantifies the effectiveness of the intake process by comparing the actual mass of air trapped inside the cylinder with the theoretical mass occupying the displaced volume at the intake manifold density [1].

$$\eta_v = \frac{m_a}{\rho_{a,i} V_d} \tag{2.9}$$

where m_a is the inducted air mass and $\rho_{a,i}$ is the intake manifold air density.

Turbocharging increases the intake air density by recovering energy from the exhaust gases to drive a compressor. The higher intake density allows a greater mass of air to enter the cylinder, increasing the amount of fuel that can be burned during each cycle without changing the engine displacement [1, 7].

For port fuel injected hydrogen engines, turbocharging also compensates for the reduction in volumetric efficiency caused by the displacement of intake air by gaseous hydrogen, thereby recovering a significant portion of the power loss associated with hydrogen operation [2, 3].

2.1.5 Exhaust Emissions

The combustion process in internal combustion engines generates gaseous pollutants whose composition depends on the fuel properties, combustion temperature, local mixture composition, and relative air fuel ratio (λ). The primary regulated emissions from spark ignition engines are carbon monoxide (CO), unburned hydrocarbons (HC), nitrogen oxides (NOx), and particulate matter (PM) [1]. Since hydrogen does not contain carbon, hydrogen fueled engines do not produce carbon based emissions from the fuel itself. Consequently, the main regulated pollutant is NOx, while only trace amounts of CO and HC may originate from the combustion of lubricating oil [2].

2.1.5.1 Pollutant Formation Mechanisms

Carbon monoxide is formed under fuel rich conditions ($\lambda < 1$), where the oxygen available is insufficient to completely oxidize carbon into carbon dioxide [1]. Hydrocarbon emissions mainly result from unburned fuel trapped in crevice volumes, flame quenching near cold combustion chamber walls, and fuel absorbed by the lubricating oil film [1]. For hydrogen engines, these mechanisms are largely absent because the fuel contains no carbon, leaving lubricating oil as the primary source of residual HC and CO emissions [2, 4].

Nitrogen oxides are produced from the reaction between atmospheric nitrogen and oxygen at high combustion temperatures. In spark ignition engines, NO is the dominant species, while NO_2 is formed through subsequent oxidation reactions. Thermal NOx formation becomes significant above approximately 1800 K and is commonly described by the extended Zeldovich mechanism [1, 8]:

$$N_2 + O \rightleftharpoons NO + N \tag{2.10}$$

$$N + O_2 \rightleftharpoons NO + O \tag{2.11}$$

$$N + OH \rightleftharpoons NO + H \tag{2.12}$$

The influence of the relative air fuel ratio on the formation of the main pollutants is shown in Figure 2.6. NOx emissions reach their highest values close to slightly lean conditions ($\lambda \approx 1.1$), where both oxygen availability and combustion temperature are sufficiently high to promote thermal NO formation. Rich mixtures reduce NOx because of the lower oxygen concentration, while very lean mixtures lower the combustion temperature and suppress the Zeldovich reactions [1, 8].

Carbon monoxide emissions decrease as the mixture approaches stoichiometric conditions due to the increased availability of oxygen for complete oxidation. Under lean conditions, CO emissions remain at very low levels. Hydrocarbon emissions generally reach their minimum near stoichiometric operation and increase under both rich and very lean conditions because of incomplete combustion and flame quenching.

These emission characteristics explain the operating strategy commonly adopted in hydrogen spark ignition engines, where lean combustion is used to limit NOx formation while maintaining high thermal efficiency [2, 3].

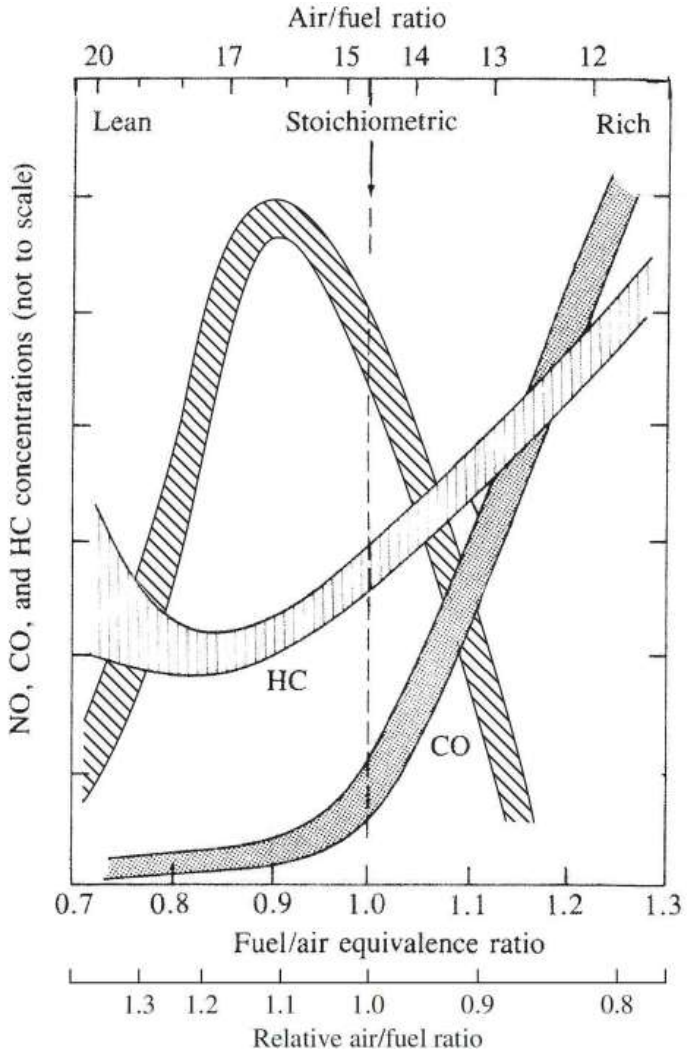


Figure 2.6: Typical variation of NO, CO, and HC emissions as a function of the relative air fuel ratio (λ). Adapted from [1].

2.1.5.2 European Regulatory Framework

The development of alternative fuel ICEs is driven by stringent environmental legislation. The European Green Deal mandates a 90% reduction in transport-related emissions by 2050 to achieve climate neutrality [9]. Furthermore, the REPowerEU strategy targets the production and import of 20 million tonnes of renewable hydrogen by 2030 to decarbonize heavy-duty transport and industrial sectors [10].

Compliance with the Euro 7 standards requires significant advancements in combustion phasing and aftertreatment systems, as these regulations impose stricter limits on NOx (e.g., 60 mg/km for SI engines) and particulate number (PN) to mitigate urban air pollution [11].

2.2 Hydrogen as a Fuel for Internal Combustion Engines

The transition toward hydrogen (H_2) as a primary energy carrier for internal combustion engines is driven by the requirement to achieve climate neutrality in the transport sector. Hydrogen is a carbon free fuel that through complete oxidation primarily yields water vapor effectively eliminating tailpipe emissions of carbon dioxide and carbon monoxide as well as unburned hydrocarbons [2].

2.2.1 Physical and chemical properties relevant to combustion

The combustion behavior of hydrogen is governed by a set of physicochemical properties that distinguish it from conventional liquid and gaseous fuels. These properties are summarized in Table 2.1 which illustrates the comparison between hydrogen and conventional hydrocarbon fuels.

Table 2.1: Representative properties of hydrogen, gasoline, and diesel under ambient reference conditions

Property	Unit	Hydrogen	Gasoline	Diesel
Molecular Weight	g/mol	2.016	60–150	150–250
Density	kg/m^3	0.08	720–760	820–845
Lower Heating Value (LHV)	MJ/kg	119.7	44.8	42.5
Stoichiometric Air–Fuel Ratio	-	34.3	14.7	≈14.5
Laminar Flame Speed	cm/s	185	37–43	20–80
Minimum Ignition Energy	mJ	0.02	0.24	0.24
Mass Diffusivity in Air	cm^2/s	≈0.61	-	-
Autoignition Temperature	°C	585	260–460	≈250

The values presented for gasoline and diesel are representative, since both fuels consist of mixtures of hydrocarbons and their properties vary with composition. Parameters such as laminar flame speed, minimum ignition energy, and autoignition temperature also depend on the temperature, pressure, and mixture composition.

Hydrogen possesses an exceptionally wide flammability range enabling stable operation across an air fuel equivalence ratio (λ) from 0.13 up to 10.0. This flexibility allows for ultra lean combustion strategies which reduce peak firing temperatures and enhance thermal efficiency. The high mass specific energy density of 119.7 MJ/kg is another advantage although the low volumetric density requires significant air displacement in the intake manifold for Port Fuel Injection (PFI) systems leading to power losses compared to gasoline operation [3].

2.2.2 Stoichiometry and Lambda Range

The stoichiometric air fuel ratio for hydrogen is determined by the mass balance of the complete oxidation reaction:

$$H_2 + 0.5(O_2 + 3.77N_2) \rightarrow H_2O + 1.885N_2 \tag{2.13}$$

The stoichiometric value is approximately 34.3 by mass [1]. The actual air fuel equivalence ratio (λ) is utilized to quantify the mixture strength where λ is the ratio of the actual air fuel ratio to the stoichiometric one [9]:

$$\lambda = \frac{(A/F)_{actual}}{(A/F)_s} \tag{2.14}$$

The wide range of lambda facilitates unthrottled operation where engine load is controlled by the fuel quantity rather than intake throttling [2].

2.2.3 Hydrogen Storage and Safety Considerations

The remarkably low density of hydrogen in its ambient state necessitates high pressure gaseous storage solutions to achieve a sufficient energy density for automotive and heavy duty transport applications [12, 13]. Current on board systems primarily rely on composite storage containers pressurized at either 350 or 700 bar to provide an adequate driving range without excessive volume requirements [12, 13]. These containers typically utilize carbon fiber reinforced plastic shells with high performance liners to maintain structural integrity under extreme mechanical stress while minimizing system weight compared to traditional steel tanks [2]. However, the volumetric energy density of hydrogen at 700 bar remains substantially lower than that of liquid gasoline, which imposes significant packaging challenges for vehicle integration [1, 12]. Additionally the compression of hydrogen to these high pressures requires a substantial energy input often exceeding 7% of the lower heating value of the fuel to reach the necessary storage density [2]. A recent example is the BMW iX5 Hydrogen which utilizes various carbon fiber reinforced plastic tanks to contain hydrogen at 700 bar while maintaining structural integrity [14].

Storage in the liquid state (LH2) is characterized by higher volumetric energy density compared to gaseous storage making it a competitive solution for heavy duty transport and aerospace applications [9, 12]. Hydrogen liquefaction occurs at cryogenic temperatures of approximately 20 K (-253 °C) and the resulting fluid is contained in specialized vacuum insulated vessels designed to minimize thermal energy transfer from the environment [2, 12]. A primary technical challenge of LH2 systems is the unavoidable heat leak from the surroundings which causes a fraction of the fuel to evaporate in a phenomenon known as boil off [2]. This leads to a continuous pressure rise within the tank requiring either active fuel consumption or controlled venting to the atmosphere to maintain structural limits [2]. Furthermore the liquefaction process is energy intensive consuming approximately 30% of the lower heating value of the hydrogen fuel [2]. Despite these thermodynamic penalties LH2 occupies a volume nearly 700 times smaller than hydrogen in its gaseous state at standard conditions enabling significantly greater energy storage within fixed spatial constraints [2, 12].

Beyond conventional gaseous and liquid states hydrogen can be stored in a solid state through chemical bonding within the lattice of specific metals and alloys [15]. This method of storage is technically possible because hydrogen can be adsorbed on the surface of a metal and subsequently absorbed into the crystalline structure after dissociation into its atomic form [2]. The selection of suitable materials is essential as the gas diffuses through most substances and reacts with the metal

lattice primarily at defects or grain boundaries [15]. Material embrittlement due to direct contact with hydrogen primarily affects ferritic steels with a body centered cubic lattice whereas this effect is not significantly observed in metals with a face centered cubic lattice such as aluminum alloys [15]. Consequently while certain materials such as titanium and high nickel alloys are highly sensitive to hydrogen others such as aluminum and copper based alloys are recognized for their compatibility and are utilized in the construction of hydrogen containment and distribution components [2, 15].

Regarding safety considerations it is often assumed that a hydrogen tank will explode in an accident. However the physical properties of the gas mitigate this risk because hydrogen has high diffusivity and low density which cause it to disperse vertically and rapidly into the atmosphere upon release [2, 12]. This rapid buoyancy can reduce the persistence of a flammable cloud near ground level in open environments compared with liquid fuels that can pool near the source of a leak [2, 12].

2.2.4 Combustion characteristics and Abnormal Phenomena

Hydrogen engines commonly employ qualitative load control, where the engine output is adjusted by varying the fuel mass flow rate ($\dot{m}_f$) while maintaining an approximately constant air flow through an unthrottled intake system [2]. This approach is similar to the load control strategy used in compression ignition engines and reduces pumping losses associated with throttled operation. The brake power (P) is defined by the energy input and efficiency according to the following equation:

$$P = \dot{m}_f LHV \eta_{th} \tag{2.15}$$

where $\dot{m}_f$ is the fuel mass flow rate and LHV is the lower heating value while η_{th} represents the thermal efficiency. Despite these advantages the low minimum ignition energy and high flame speeds of hydrogen promote the occurrence of abnormal combustion phenomena.

2.2.4.1 Pre-ignition

Pre-ignition is a abnormal combustion phenomenon characterized by the ignition of the fresh fuel air charge during the compression stroke before the intended spark discharge occurs. This event is primarily caused by the remarkably low minimum ignition energy of hydrogen which allows unintended heat sources to initiate the chemical reaction [2]. The principal triggers include localized hot spots within the combustion chamber such as overheated spark plug electrodes or exhaust valves as well as residual gas and oil ash particles remaining from previous cycles [3].

The consequences of pre-ignition are severe because the resulting pressure rise occurs while the piston is still moving toward top dead center. This leads to a significant amount of negative compression work and a dramatic reduction in the indicated mean effective pressure. Furthermore pre-ignition subjects engine components to peak cylinder pressures that far exceed those of regular combustion cycles, as illustrated in Figure 2.7. Mitigation strategies involve utilizing cold

rated spark plugs to prevent electrode overheating and employing sodium filled exhaust valves for enhanced heat dissipation [2]. Additionally the transition to direct injection systems permites fuel delivery later in the cycle which effectively bypasses the conditions required for pre-ignition [16].

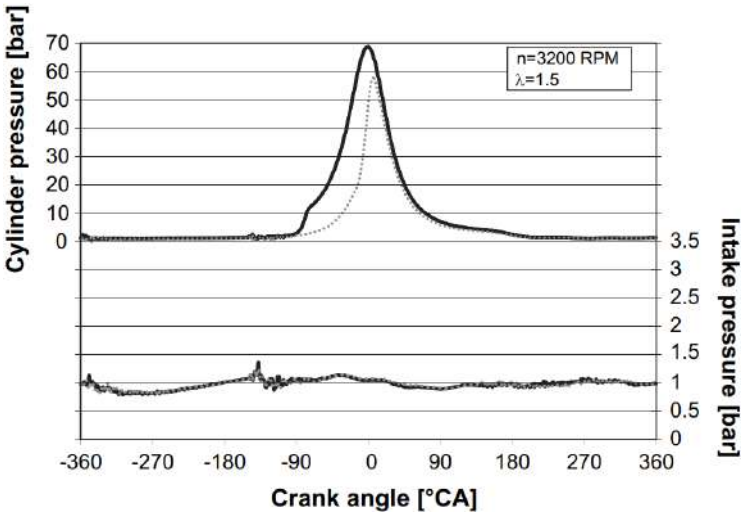


Figure 2.7: Typical cylinder and intake manifold pressure traces during a pre-ignition event (solid lines) compared to a regular cycle (dotted lines) [2].

2.2.4.2 Backfire

Backfire refers to the combustion of the hydrogen air mixture within the intake runner or manifold during the induction stroke while the intake valve is still open. This phenomenon is a critical constraint for port fuel injection systems and is typically triggered by the ignition of the incoming charge upon contact with hot residual gases or hot surfaces during the valve overlap period [17]. Factors such as high residual gas temperatures and inappropriate injection timing are the primary drivers for this anomaly [2].

The effects of backfire include sudden pressure spikes in the induction system, as shown in Figure 2.8 which can damage the intake manifold and the fuel injectors. Furthermore the combustion of fuel in the intake manifold results in a substantial loss of volumetric efficiency and engine power since less fresh mixture reaches the cylinder. To mitigate backfire it is essential to employ timed injection strategies that ensure the intake port is free of hydrogen at the start of the intake stroke [4]. This allows an initial period of pure air to cool the internal surfaces. While retarding the start of injection is effective the total elimination of backfire is most reliably achieved through direct injection where fuel is only introduced after the intake valve has closed [9].

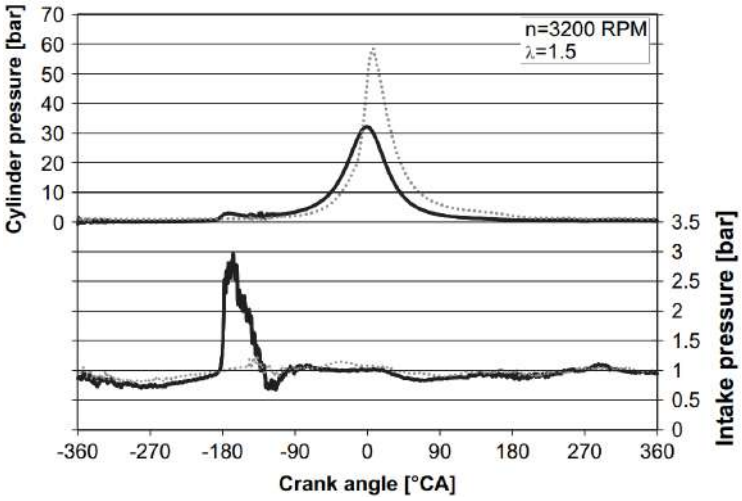


Figure 2.8: Typical cylinder and intake pressure traces for a backfiring cycle (solid lines) compared to regular pressure traces (dotted lines) [2].

2.2.4.3 Knock

Knock in hydrogen engines involves the spontaneous autoignition of the unburned end gas ahead of the advancing flame front. Hydrogen's high burning velocity and wide flammability range promote rapid energy release leading to intense high frequency pressure oscillations [1]. Triggers for knock include high compression ratios and elevated temperatures at high loads which accelerate the chemical kinetics of the end gas [8].

The physical manifestation of knock includes a sharp metallic noise and high frequency oscillations that cause increased mechanical and thermal stress on the piston crown and cylinder head. Over time these oscillations can lead to material fatigue or catastrophic failure of the piston rings and lands. Figure 2.9 demonstrates typical cylinder pressure knocking traces. Mitigation approaches focus on controlling the end gas state through spark timing retardation which lowers peak pressures and temperatures [2]. Lean burn strategies and exhaust gas recirculation are also highly effective as they dilute the mixture and reduce the peak combustion temperatures responsible for autoignition [12].

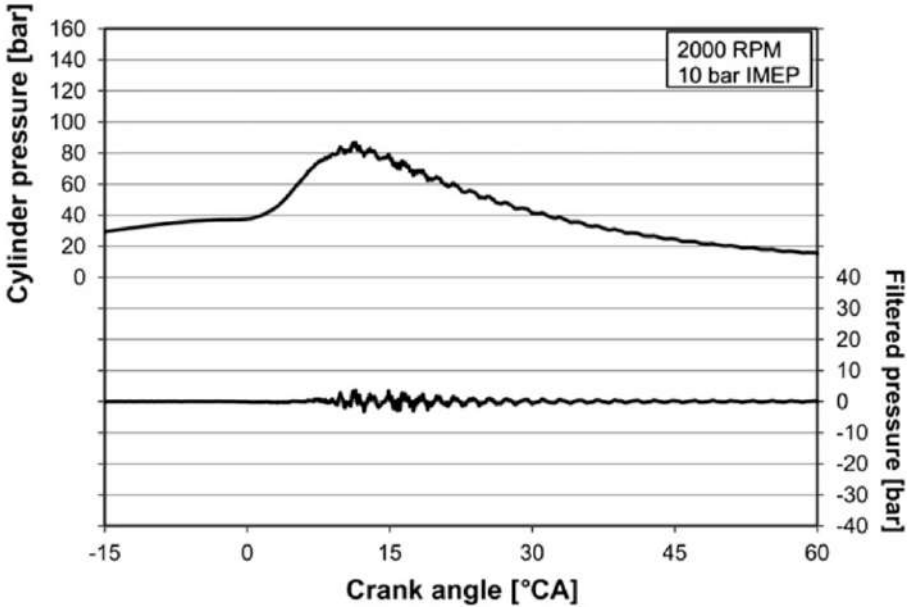


Figure 2.9: Typical cylinder pressure knocking traces [2].

2.2.5 Current state of H2 ICE development

Historically conversions of engines to hydrogen were attempted as early as the 1930s by Rudolf Erren who used separate valves for hydrogen injection to overcome backfire issues in early systems [2].

The industrial development of hydrogen internal combustion engines (H2 ICE) has gained significant momentum as a robust solution for decarbonizing sectors where battery electric systems face practical limitations, such as heavy-duty transportation, marine propulsion, and stationary power generation [8, 9, 12]. Unlike fuel cells, which require high purity hydrogen and expensive catalyst materials, H2 ICE technology utilizes mature manufacturing chains and offers higher volumetric power density [8, 12]. Recent progress indicates that these engines can achieve brake thermal efficiencies of up to 45%, making them increasingly competitive with conventional diesel powertrains [2, 8].

In the heavy duty sector, the transition is driven by the requirement for high payload capacity and fast refueling times, which are currently unattainable with battery technologies for long haul logistics [9, 12]. Direct Injection (DI) has emerged as the frontrunner for high performance applications, as it eliminates backfire and restores volumetric efficiency by injecting fuel after intake valve closure [2, 18, 19]. Furthermore, the aerospace industry is actively investigating hydrogen as an energy carrier for future aircraft. The Airbus ZEROe programme has evaluated both hydrogen combustion and fuel cell propulsion concepts, with hydrogen fuel cell electric propulsion selected in 2025 as the principal development pathway [12].

Strategic research is now focused on achieving near zero nitrogen oxide (NOx) emissions through advanced in-cylinder management rather than complex aftertreatment systems [8, 20].

Recent studies highlight a control hierarchy where oxygen enrichment and ultra lean combustion ($\lambda > 2.0$) serve as the ultimate enablers for zero NOx operation [2, 4, 12]. Additionally, the implementation of hybrid hydrogen-gasoline strategies is being explored to enhance cold start performance and stability at low loads while maintaining full power at high speeds through gasoline operation [4, 21]. These technological advancements are supported by a rapidly expanding global hydrogen infrastructure, particularly within the European Union's regulatory framework, which targets the integration of renewable hydrogen into 10% of total energy needs by 2050 [12].

The application of hydrogen internal combustion technology has extended into high performance motorsports as an accelerated platform for testing component durability and combustion stability under extreme thermal and mechanical loads [2, 8]. Toyota Gazoo Racing has emerged as a primary proponent of this development through the GR Yaris H2 prototype which participated in World Rally Championship (WRC) stages to evaluate the robustness of gaseous hydrogen systems in variable rally environments [22]. Furthermore the transition toward liquid hydrogen (LH2) storage has been pioneered in the GR Yaris, Figure 2.10, during consecutive participations in the 24 Hours of Nürburgring endurance races [23]. The utilization of LH2 provides significant advantages in terms of volumetric energy density and refueling speed which are critical for the demanding requirements of endurance racing [2, 12]. These technological milestones culminated in the debut of the GR H2 Racing Concept a liquid hydrogen prototype designed for the future hydrogen class at the 24 Hours of Le Mans [24]. This progress demonstrates the capability of hydrogen internal combustion engines to deliver high power density and competitive range while maintaining the characteristic acoustic profile and driver engagement of traditional powertrains in elite racing categories [4, 9].



Figure 2.10: Toyota liquid hydrogen race car during the 24 Hours of Nürburgring 2026 endurance race.

Industrial implementation of hydrogen technology is also currently being pursued by major heavy duty manufacturers. For instance MAN Energy Solutions provides hydrogen units for power generation and marine applications while MAN Truck and Bus has introduced the hTGX truck for

long haul logistics [25, 26]. In the off road sector JCB has received regulatory approval for hydrogen fueled construction machinery proving the robustness of spark ignited hydrogen technology [27]. Modern infrastructure support is expanding in regions such as Germany where dedicated funding schemes for hydrogen refueling stations and commercial fleets are active [28].

2.3 Fuel Injection Systems for Gaseous Fuels in ICE

The delivery of gaseous fuels into internal combustion engines requires specialized hardware to manage high volumetric flow rates and the compressibility of the working fluid [16]. Unlike liquid fuels gaseous hydrogen necessitates systems that can accommodate its low mass density and high diffusivity to ensure stable combustion and optimal performance [2]. The primary technical challenge involves balancing the mixture strength and timing to maximize power density while avoiding abnormal combustion phenomena [17].

2.3.1 Port Fuel Injection (PFI)

Port Fuel Injection is the most prevalent strategy for hydrogen engines due to its lower complexity and the ease of retrofitting existing spark ignition architectures [4]. In this configuration hydrogen is injected into the intake runner upstream of the intake valve at relatively low pressures typically not exceeding 0.5 MPa [2].

The formation of a highly homogeneous mixture is a principal advantage of PFI systems because of the high diffusivity of hydrogen and the extended mixing time available in the intake port [2, 12]. However the gaseous fuel occupies a significant portion of the intake volume approximately 30% under stoichiometric conditions [1, 9]. This air displacement results in a substantial reduction in volumetric efficiency and a theoretical power loss ranging from 15% up to 20% [3, 4]. Furthermore PFI systems are inherently susceptible to backfire because an ignitable mixture is present in the intake manifold during the induction stroke [17].

2.3.2 Direct Injection (DI)

Direct Injection systems deliver hydrogen directly into the combustion chamber after the intake valve has closed [18]. This strategy requires fuel delivery systems capable of providing injection pressures ranging from 2 MPa in low pressure systems to 40 MPa to ensure adequate fuel mass delivery within the limited time window of the compression stroke [16].

The utilization of DI provides a significant increase in power density by eliminating the air displacement effect in the intake system [9, 19]. Investigations indicate that DI engines can achieve peak indicated mean effective pressures that are significantly higher than PFI counterparts often exceeding 1.3 MPa [2, 19]. Additionally DI completely eliminates the risk of backfire since no fuel is present in the intake ports during the valve overlap period. This configuration also facilitates mixture stratification which can be utilized to stabilize lean combustion and potentially reduce heat transfer losses through the cylinder walls [8]. Despite these benefits the technology faces

challenges related to the low lubricity and viscosity of hydrogen which can increase frictional wear in the injector components and reduce overall system durability [16].

2.3.3 Comparative Analysis of Injection Strategies

The choice between PFI and DI involves trade offs in terms of hardware cost and engine performance [2]. PFI systems offer robust operation and simplified mixture preparation but are limited by lower power output and the risk of abnormal combustion [9]. Conversely DI systems enable higher power densities and greater efficiency through unthrottled operation across the entire load range [18, 19]. Some modern designs investigate dual injection to combine the homogeneity of PFI at low loads with the knock resistance and power potential of DI at high loads [4, 9].

Chapter 3

System Description

This chapter describes the engine, hydrogen injection system, and experimental instrumentation used in this work. The main engine characteristics are first presented, followed by the layout and operation of the hydrogen injection system, including the proportional valve, rotary distributor, connection hoses, check valves, and nozzles. The measurement equipment used to monitor the injection system, intake and exhaust conditions, in-cylinder pressure, engine performance, and emissions is then described.

3.1 The DEUTZ TCD 3.6 L4 Engine

The experimental platform is based on a series production industrial diesel engine, specifically the DEUTZ TCD 3.6 L4 shown in Figure 3.1. This power unit is an inline four cylinder, four stroke engine used in industrial and agricultural machinery [3].



Figure 3.1: DEUTZ TCD 3.6 L4.

3.1.1 Engine specifications and architecture

The engine architecture features a grey cast iron cylinder crankcase and head. The gas exchange process is managed by one intake and one exhaust valve per cylinder, driven by a bottom mounted camshaft via a valvetrain consisting of hydraulic tappets, pushrods, and rocker arms [3]. The induction system includes a turbocharger with a wastegate and charge air cooling to manage intake density. In its original configuration, fuel delivery is achieved through a common rail direct injection system. The main technical specifications of the base engine are summarized in Table 3.1.

Table 3.1: Technical specifications of the DEUTZ TCD 3.6 L4 base engine

Parameter	**Value**	**Unit**
Cylinder arrangement	Inline 4	-
Displacement	3621	cm^3
Bore $\times$ Stroke	98 $\times$ 120	mm
Connecting rod length	184.5	mm
Original compression ratio	17.2:1	-
Maximum power	100 at 2300 rpm	kW
Maximum torque	500 at 1600 rpm	Nm
Aspiration	Turbocharged	-

3.1.2 Adaptation for gaseous fuel operation

To enable operation with gaseous fuels such as hydrogen, the engine underwent specific hardware modifications to account for the different combustion characteristics of gas compared to diesel[3].

The primary modification is the reduction of the geometric compression ratio from 17.2:1 to 12.15:1. This is achieved by reworking the piston crown geometry to incorporate a rotationally symmetrical bowl, reducing the susceptibility to knocking combustion and limiting peak cylinder pressure [3].

For hydrogen operation, the original compression ignition system was replaced by a spark ignition (SI) system. This required the installation of spark plugs in the cylinder head. The spark plugs were mounted in the positions previously occupied by the diesel injectors, as shown in Figure 3.2. Fuel delivery was consequently transferred from direct diesel injection to Port Fuel Injection (PFI), as illustrated in Figure 3.3. In this configuration, gaseous fuel is delivered cyclically to the intake ports through the mechanical rotary distributor.

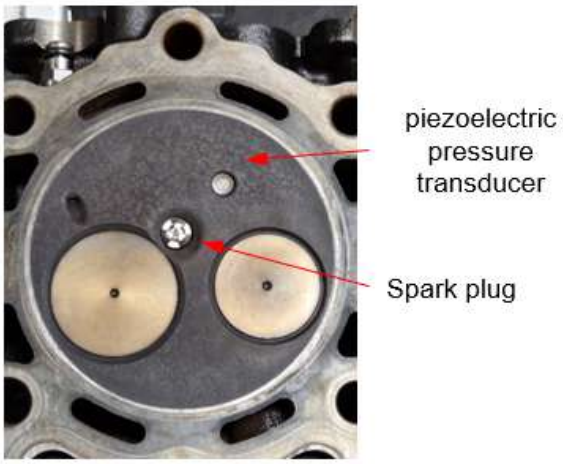


Figure 3.2: Spark plug and piezoelectric pressure transducer location.

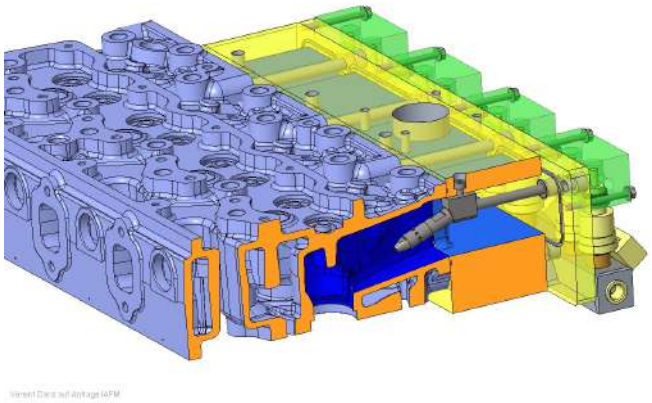


Figure 3.3: CAD of the modified cylinder head.

3.2 H_2/Syngas Injection System

The fuel delivery system provides controlled and synchronized metering of gaseous hydrogen or syngas to the engine cylinders. This system replaces the original diesel injection architecture of the engine to accommodate the specific requirements of gaseous fuels.

3.2.1 System architecture and component chain

The injection subsystem, represented schematically in Figure 3.4 consists of a sequential chain of components that regulate the pressure and mass flow of the fuel. The delivery path begins at the high pressure gas storage, where the pressure is reduced to an operational level between 10 and 15 bar by mechanical regulators [3]. A Coriolis mass flow meter is integrated into the supply line to measure the fuel mass flow rate.

Downstream of the flow meter, an electronic proportional valve serves as the main actuator for load control. This valve is connected to the engine control unit (ECU), which adjusts the flow area based on the required fuel mass. The final stage of the chain is the mechanical rotary distributor, which routes the fuel to the individual intake ports through flexible hoses and terminal nozzles.

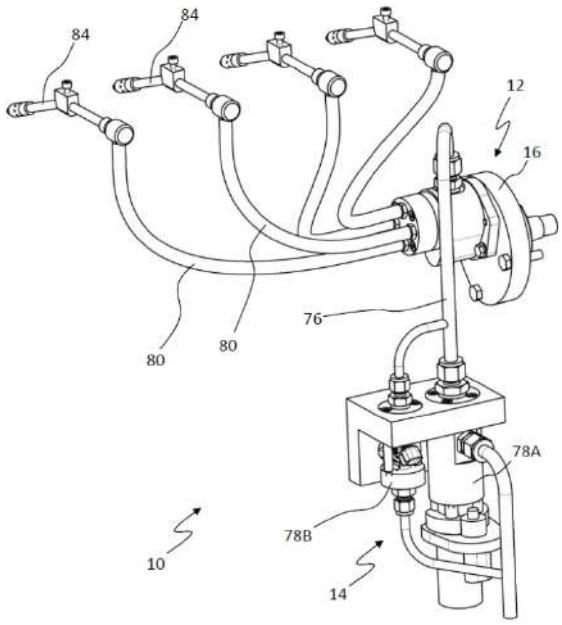


Figure 3.4: Schematic of the H_2/Syngas injection system architecture and component chain.

3.2.2 Operating principle: from supply to cylinder

The system operates through the synchronization between electronic load control and mechanical fuel distribution. The ECU calculates the necessary fuel mass flow for a given operating point based on parameters such as engine speed and manifold pressure. This calculation determines the position of the proportional valve, which regulates the amount of gas entering the distributor chamber.

The mechanical rotary distributor has an internal 3:1 gear ratio that's driven by the engine front gear train at half the crankshaft speed. This mechanical link ensures a relationship between the engine gas exchange process and the fuel delivery window. Inside the distributor, a rotating graphite disc features a single opening that periodically overlaps four stationary ports. This overlap releases the pressurized fuel to each cylinder in accordance with the engine firing order (1-3-4-2). The resulting injection profile is defined by the internal geometry of the distributor sectors, ensuring that fuel is delivered during the intake stroke for the PFI operation.

3.3 Proportional Valve

The Proportional Valve, Figure 3.5, is a electronic actuated metering device designed for low pressure gas injection. The assembly features a flat seat design incorporating a valve plate made of graphite.

The primary role of the proportional valve is to regulate the fuel mass flow supplied to the distributor according to the engine control strategy. The valve varies its effective flow area, A_{eff}, as a function of the commanded position.

Under the investigated operating conditions, the pressure ratio across the valve remains below the critical pressure ratio and the flow is therefore choked. In this regime, the mass flow is independent of downstream pressure and is primarily determined by the upstream gas conditions and the effective flow area of the valve [3]. The relationship between commanded position and effective flow area, together with the valve linearity and hysteresis, is determined experimentally in Chapter 5.

To provide a comprehensive overview of its internal architecture and assembly requirements, the complete set of technical drawings and CAD representations is documented in Appendix A.

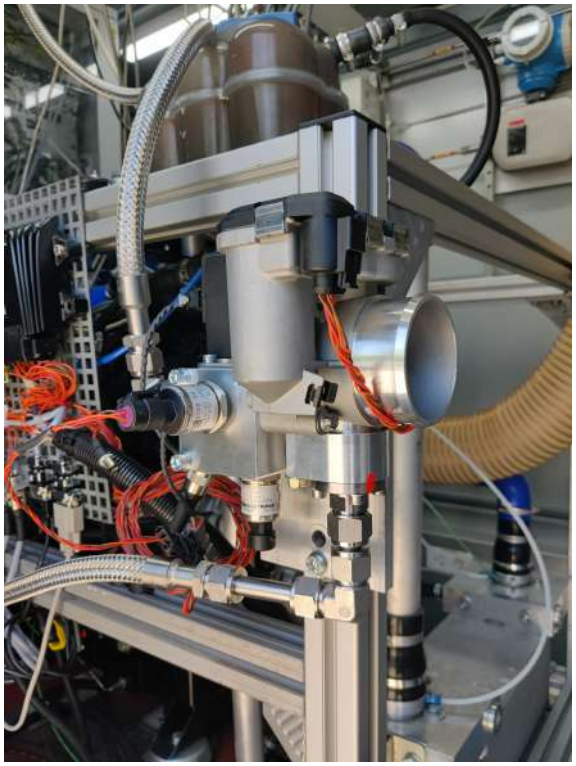


Figure 3.5: Proportional valve mounted on the test bench.

3.4 Rotary Distributor

The sealing and distribution interface relies on a rotating graphite disc in axial contact with a stationary steel plate. Graphite was selected as the rotor material due to its self lubricating properties and low friction coefficient, which minimize wear and mechanical losses at the high rotational frequencies required for engine synchronization [3]. The distribution of fuel is governed by the geometric overlap between a single window in the rotor and four matched annular sector windows in the stator. The resulting flow area profile is strictly triangular, a direct consequence of the linear geometry of the sectors, providing a symmetric and repeatable mass flow delivery to each cylinder.

3.4.1 Distributor 160 A

The Distributor 160 A, Figure 3.6, represents the optimized mechanical distribution unit for the DEUTZ TCD 3.6 engine project. This implementation features four stationary ports equally spaced at 90° intervals in the distributor reference, which maps to 180° dCA in the crankshaft reference frame. With a sector angular width (α) of 24°, the system defines an injection window duration of 96° dCA. This geometry ensures a non simultaneous overlap condition, satisfying the requirement that only one cylinder port is active at any given time, therefore preventing fuel cross flow and maintaining the integrity of the individual injection events.

The mechanical rotary distributor is installed at the location previously occupied by the diesel pump, facilitating the retrofitting process by utilizing an existing engine architecture. This positioning allows the distributor to use the mechanical power directly from the engine's gear train through an interface with a toothed wheel connected to the crankshaft.

To ensure the delivery of fuel in coordination with the engine's cycle, the distributor's internal components are synchronized with the crankshaft rotation. For a four stroke operating cycle, the fuel injection pulse for each cylinder must occur once every 720° dCA, requiring the distributor rotor to complete one full revolution per engine cycle (a ratio of 0.5 relative to the crankshaft).

To achieve this specific rotational frequency while maintaining compatibility with the engine's drive train, the distributor incorporates an internal gear reduction ratio of 3:1. This reduction mechanism, in this case using a planetary gear system, compensates for the rotational speed of the input drive gear provided by the engine.

Detailed drawings and views are available in Appendix A.



Figure 3.6: Distributor 160 A mounted on the engine.

3.5 Connection Hose

Flexible hoses provide the flow connection between the mechanical rotary distributor and the individual cylinder nozzles. Their flow behaviour was investigated to determine the influence of hose geometry on the hydrogen delivery system. The standard configuration uses a natural gas hose with an internal diameter of 9 mm and a length of 460 mm. For the comparative engine tests, the cylinder 4 line was also tested with a second similar hose connected in series, resulting in approximately twice the standard length, and with a 6 mm internal diameter fuel hose of the standard length. Figure 3.7 shows the two hose types used during the tests.



Figure 3.7: Hoses used in the injection system: natural gas hose (orange) and fuel hose (black).

3.6 Nozzle

The terminal nozzles represent the final stage of the fuel delivery chain and direct the hydrogen into the intake ports. Each standard nozzle incorporates a check valve intended to prevent reverse flow from the intake port into the hydrogen delivery line and to isolate the fuel line from intake pressure fluctuations [3].

To evaluate the influence of these components on the fuel line pressure dynamics and engine operation, the standard configuration was compared with the nozzle without its internal check valve and with a configuration in which both the check valve and nozzle were removed from the cylinder 4 branch. The nozzle and check valve are shown in Figure 3.8.



Figure 3.8: Injection nozzle and check valve disassembled.

3.7 Instrumentation and Measurement Systems

The experimental tests were performed using the instrumentation listed in this section. The measurement system was used to acquire the operating parameters required for the characterization of the proportional valve and the rotary distributor as well as the engine experimental campaign. The instrumentation used throughout the experimental campaign is summarized in Table 3.2.

3.7.1 Pressure and Temperature Measurement

Then in-cylinder pressure was measured using a water cooled piezoelectric pressure transducers (Kistler 6041A) connected to charge amplifiers (Kistler 5064B). The instantaneous intake and exhaust port pressures were measured using piezoresistive pressure transducers (Kistler 4007B and Kistler 4049A). Absolute and gauge pressures in the fuel supply system were measured using Keller PAA-33X and Keller PR-33X pressure sensors, respectively. Coolant, intake air and exhaust gas temperatures were measured using Type-K (NiCr-Ni) thermocouples.

3.7.2 Flow Rate, Crank Angle and Torque Measurement

Fuel mass flow rate was measured using a Coriolis flow meter (Endress+Hauser Promass A300). Intake air mass flow rate was measured using a thermal mass flow meter (ABB Sensyflow FMT700-P). Crankshaft position was measured using a Kistler 2614C11 crank angle encoder that has a resolution of 0.1 dCA. Engine torque was measured using an HBM T40 torque flange coupled to an eddy current dynamometer.

3.7.3 Exhaust Gas Analysis

Nitrogen oxide (NO_x) emissions were measured using an Ecophysics CLD700 chemiluminescence analyser. In case of syngas operation the fuel composition is monitored using an MRU VARIOluxx gas analyser, allowing the measurement of the main gas species, including H_2, CO, CO_2 and CH_4.

Table 3.2: Instrumentation used during the experimental campaign

Measured quantity	**Instrument**	**Model**	**Specification**
Cylinder pressure	Kistler	6041A	0–250 bar, ±0.2 bar
Charge amplifier	Kistler	5064B	Signal conditioning
Intake port pressure	Kistler	4007B	0–10 bar, ±0.2 bar
Exhaust port pressure	Kistler	4049A	0–10 bar, ±0.2 bar
Fuel pressure	Keller	PAA-33X / PR-33X	0–100 bar, 0.1% FS
Temperature	Type-K thermocouple	NiCr–Ni	233–1473 K, ±2.5 K
Fuel mass flow rate	Endress+Hauser	Promass A300	0–33 kg/h, ±0.2%
Air mass flow rate	ABB	Sensyflow FMT700-P	0–1200 kg/h, ±0.25%
Crank angle	Kistler	2614C11	0.1 dCA resolution
Torque	HBM	T40	1 kNm, ±0.1%
NO_x concentration	Ecophysics	CLD700	0–10000 ppm, ±1%
Gas composition	MRU	VARIOluxx	H_2, CO, CO_2, CH_4

Chapter 4

Geometric Characterization of the Rotary Distributor

The rotary distributor, designated model 160 A, is the central component of the H_2 injection system and is responsible for sequential fuel delivery to each engine cylinder. Its geometric overlap area is not constant but varies continuously with the rotational position of the graphite rotor, making the characterization of this variation important for the interpretation of the experimental flow characterization and numerical simulation.

This chapter presents the geometric parameters of distributor 160 A, the derived overlap area profile, and the principal results of the characterization. The complete mathematical derivation of the overlap area model, including all intermediate equations and the spreadsheet implementation, is documented in Appendix B.

4.1 Operating Principle and System Architecture

The distributor operates on the principle of a rotating disc valve, consisting of a graphite rotor with a single partial annular sector window and a fixed stator with four corresponding outlet windows, one for each cylinder and equally spaced at 90° intervals. Fuel flow to a given cylinder is possible only when the rotor window overlaps the corresponding stator window. Outside the overlap region, the respective outlet is geometrically closed. The rotor is driven by the engine crankshaft through an internal 3:1 gear reduction, completing one full revolution per engine cycle (720° of crank angle in the four stroke configuration), so that injection events to the four cylinders are equally spaced at 180° of crank angle.

Figure 4.1 shows the distributor 160 A, illustrating the assembly of the graphite rotor, stator body, and toothed wheel. The toothed wheel is the only externally accessible rotating element and provides the angular reference for all geometric characterization work.

The opening and closing sequence is illustrated schematically in Figure 4.2. As the rotor advances from the fully closed position, the geometric overlap between the rotor and stator windows increases linearly until full alignment is reached, after which it decreases symmetrically back to



Figure 4.1: Distributor 160 A disassembled.

zero. For the ideal sharp edged sector geometry, this results in the triangular overlap area profile discussed quantitatively in Section 4.3.

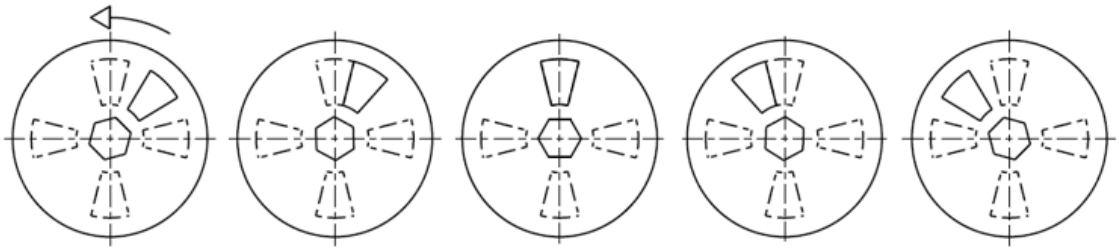


Figure 4.2: Schematic of the overlap area.

4.2 Geometric Parameter Measurement

The geometric parameters of the partial annular sector window were measured directly on the CAD model. The inner radius r_1 and outer radius r_2 were obtained on the respective arc faces of the sector, and the sector angular width α was measured between the two radial planar faces, with the measurement axis coincident with the axis of rotation.

Figure 4.3 shows the CAD model of the stator plate, indicating the geometric parameters r_1, r_2, and α. These three parameters fully define the ideal partial annular sector geometry and, together with the distributor kinematics, determine the derived quantities presented in this chapter.

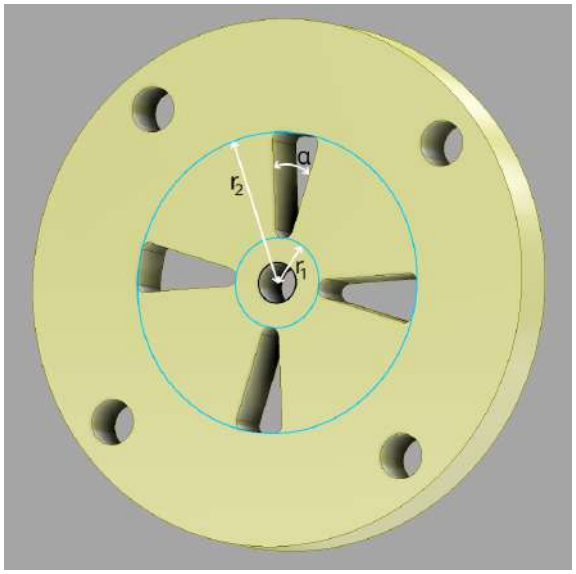


Figure 4.3: CAD model of the stator plate showing the geometric parameters r_1, r_2, and α.

Table 4.1 lists the measured geometric parameters together with the kinematic parameters of the assembly.

Table 4.1: Measured geometric and kinematic parameters of the Distributor 160 A

Parameter	Symbol	Unit	Value
Partial annular sector (window) geometry			
Inner radius	r_1	mm	6.0
Outer radius	r_2	mm	19.5
Sector angular width	α	deg	24.0
Number of stator outlet windows	N	–	4
Kinematic parameters			
Internal gear ratio (wheel : rotor)	i	–	3
Engine cycle (four-stroke)	Ψ	dCA	720
Cylinder firing interval	$\Delta\theta_{\mathrm{CA}}$	dCA	180

4.3 Derived Geometric Quantities and Overlap Area Profile

From the measured parameters in Table 4.1, the quantities relevant to the geometric description of the distributor and the experimental flow characterization are derived analytically, as detailed in Appendix B.

Table 4.2: Derived geometric quantities of the Distributor 160 A

Quantity	Symbol	Unit	Value
Flow area			
Maximum overlap area (ideal)	$A_{\max}$	mm^2	72.10
Maximum overlap area (measured)	$A_{\max,\mathrm{real}}$	mm^2	70.78
Deviation from ideal	ε_A	%	1.83
Equivalent reference diameter	D_{ref}	mm	9.58
Injection window (toothed wheel reference)			
Injection window duration	$\Delta\theta_w$	deg	144
Peak alignment position	$\theta_{w,\mathrm{peak}}$	deg	72
Half-window width	$\alpha \cdot i$	deg	72
Injection window (crank angle reference)			
Injection window duration (CA)	$\Delta\theta_{\mathrm{CA,inj}}$	dCA	96
Half-window width (CA)	α/ratio	dCA	48
Angular period between injections	P_{CA}	dCA	180

The overlap area profile $A(\theta_w)$ computed from these parameters is plotted in Figure 4.4. For the ideal sector geometry, the profile is a symmetric isosceles triangle spanning the toothed wheel interval $[0^\circ, 144^\circ]$, with the maximum geometric overlap area $A_{\max} = 72.10\ \mathrm{mm}^2$ occurring at $\theta_w = 72^\circ$, corresponding to full alignment between the rotor and stator windows. This linear variation results from the relationship between the relative angular displacement of two identical annular sector windows and their overlapping angular width.

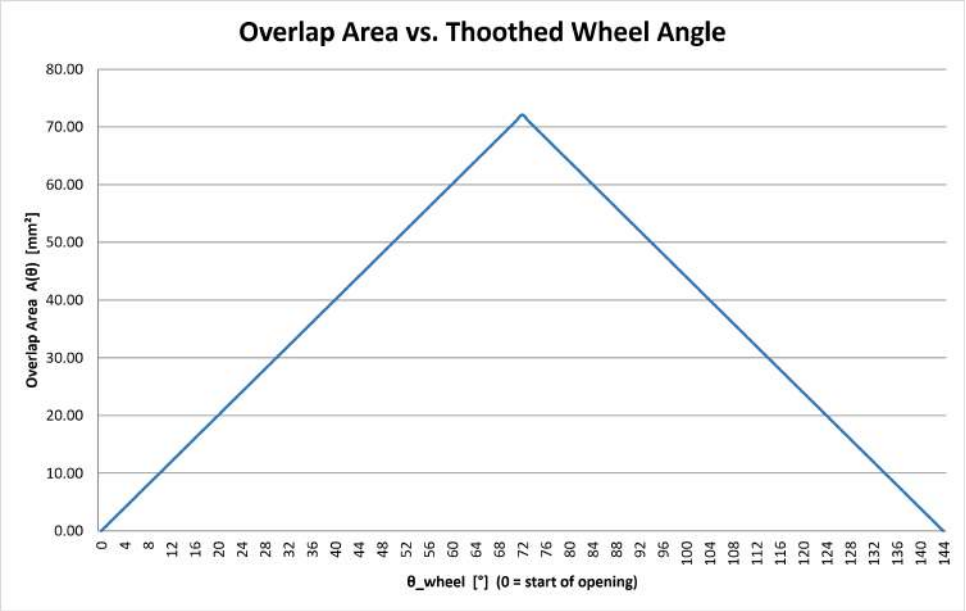


Figure 4.4: Computed overlap area profile $A(\theta_w)$ for distributor 160 A as a function of toothed wheel angle.

The geometric overlap area presented here should not be confused with the experimentally determined effective flow area, A_{eff}. The latter also reflects the actual flow behaviour through the distributor and is determined experimentally in Chapter 5.

4.4 Effect of Machining on the Real Sector Geometry

The analytical model described in Appendix B and used to derive the results in Table 4.2 assumes a geometrically perfect partial annular sector with sharp radial edges. In practice, the stator windows contain slightly rounded edges as a consequence of the machining process, which introduces rounded corners at the junctions between the radial faces and the inner and outer arcs. As a result, the real open area at full alignment is marginally smaller than the ideal computed value A_{max}.

The real maximum overlap area was determined by direct measurement of the sector profile and is reported in Table 4.2. The deviation from the ideal value is approximately *1.83%*. This discrepancy is sufficiently small to be considered negligible for the purposes of flow characterization calculation and numerical simulation.

Chapter 5

Flow Characterization

This chapter presents the experimental characterization of the two main components responsible for hydrogen metering and distribution: the proportional valve 620 B and the mechanical rotary distributor 160 A. The objective is to determine the relationship between the operating position of each component and its effective flow area, A_{eff}, and to assess the behaviour of the components over their respective operating ranges.

Both components were characterized using compressed air. The mass flow rate was measured with a Coriolis mass flow meter, while the pressures upstream and downstream of each component and the gas temperature were recorded for each measurement point. The complete experimental procedure, together with the equations used to determine the pressure ratio, gas density, isentropic flow function, and effective flow area, is presented in Appendix C. The present chapter therefore focuses on the analysis of the resulting component characteristics.

The experimental setup used for these measurements is shown in Figure 5.1.

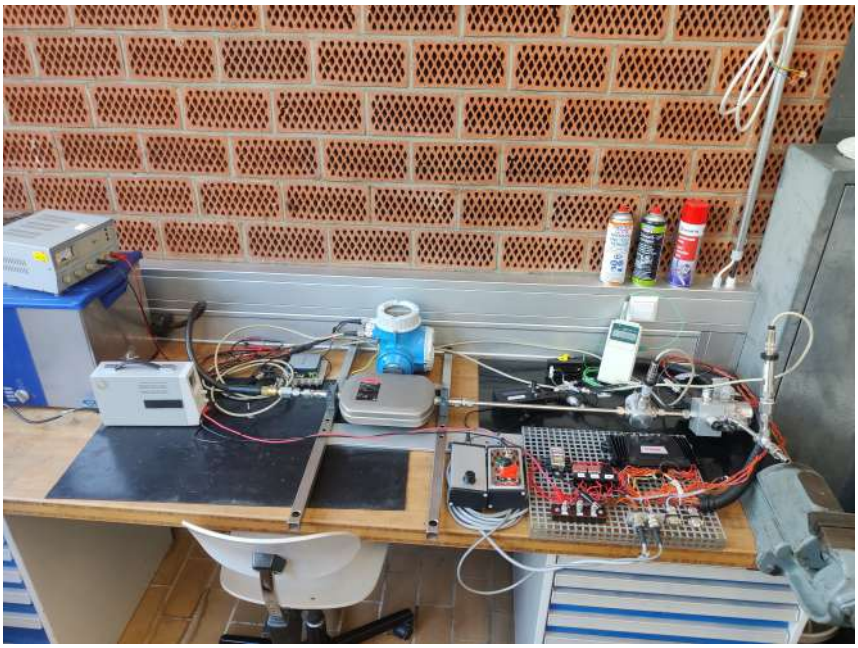


Figure 5.1: Experimental setup used for the flow characterization tests.

5.1 Proportional Valve Characterization

The proportional valve was characterized by progressively changing the relative valve position commanded by the TRIJEKT ECU and measuring the corresponding air mass flow rate. The measurements were performed at an ambient pressure of approximately 0.999 bar and an air temperature of 27 °C. Over the active measurement range, the absolute upstream pressure decreased from approximately 10.78 bar to 8.94 bar as the valve opening increased, while the downstream pressure remained close to ambient pressure.

The measured downstream to upstream pressure ratio remained between approximately 0.093 and 0.118. This is considerably below the critical pressure ratio of approximately 0.528 for air under the assumptions used in the calculation procedure. Consequently, the proportional valve was operated under choked flow conditions throughout the characterization. The treatment of this flow regime and its implementation in the effective area calculation are described in Appendix C.

5.1.1 Effective Flow Area and Linearity

The resulting effective flow area as a function of the commanded valve position is presented in Figure 5.2.

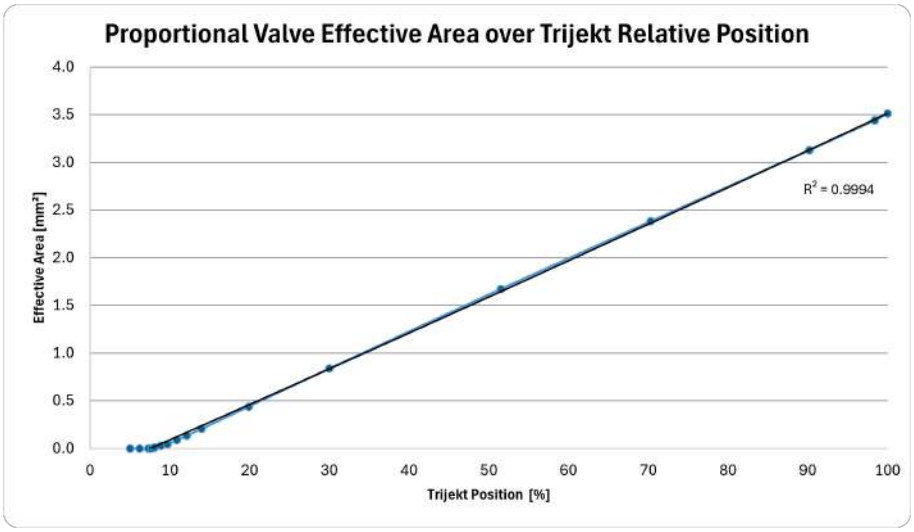


Figure 5.2: Effective flow area of proportional valve 620 B as a function of commanded position.

At the lowest commanded positions, the valve remains effectively closed. Between 5 and 7.7% position, the calculated effective area remains close to zero. A measurable increase begins at approximately 8% valve position, with $A_{\text{eff}} = 0.0097$ mm^2 at 8.1% and 0.0273 mm^2 at 8.9%. This behaviour identifies a small initial operating region in which changes in the commanded position produce only a limited change in flow area.

Beyond this opening region, the effective area increases almost linearly with valve position. The linear regression used in the calculation tool, based on the measurements between 10.9 and 98.4% valve position, provides a coefficient of determination of approximately $R^2 = 0.99993$. The measured effective area increases from 0.089 mm^2 at 10.9% to 3.441 mm^2 at 98.4%. The corresponding measured air mass flow rate at 98.4% is approximately 25.85 kg/h under the test conditions.

The high value of R^2 shows that the relationship between commanded position and effective area can be represented accurately by a linear relation once the initial opening region has been exceeded. Extrapolation of this fit to 100% valve position gives an effective area of

$$A_{\text{eff},100} = 3.513 \text{ mm}^2.$$

The same linear fit reaches zero effective area at a commanded position of approximately 8.4%, which is consistent with the opening threshold observed in the experimental measurements. This offset is relevant when the commanded valve position is converted into an effective flow area, since a zero command to area relation cannot be assumed over the complete position range.

The geometric reference area used in the calculation tool is 4.909 mm^2. Comparison with the extrapolated effective area at full opening results in a discharge coefficient of

$$C_d = 0.716.$$

The effective area at full opening therefore corresponds to approximately 71.6% of the geometric area. The value below unity is consistent with the difference between the geometric passage area and the flow capacity of the real component.

5.1.2 Valve Hysteresis

In addition to the main opening characteristic, the proportional valve was tested in both increasing and decreasing position directions in order to evaluate the dependence of the effective flow area on the direction of valve movement. The resulting opening and closing characteristics, together with the corresponding hysteresis, are presented in Figure 5.3.

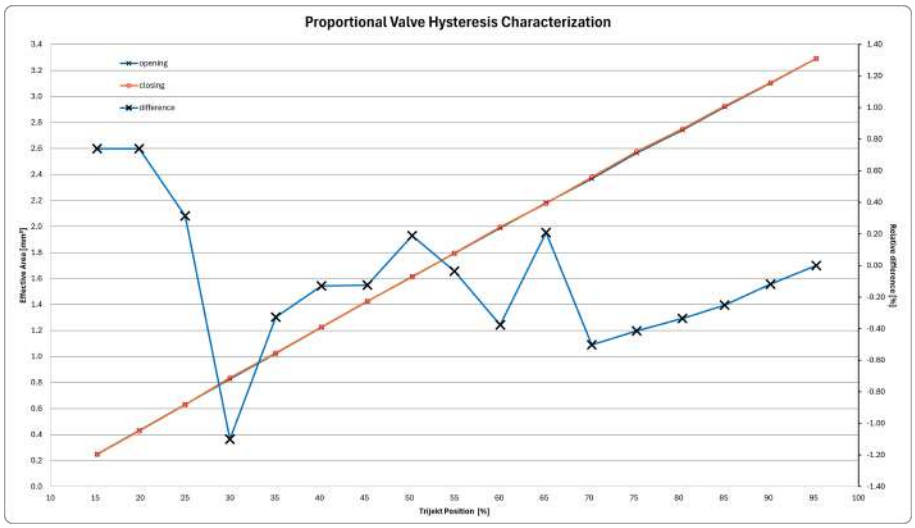


Figure 5.3: Opening and closing effective flow area characteristics and hysteresis of proportional valve 620 B.

The opening and closing curves remain very close over the complete measured range. For example, at 30% valve position, A_{eff} is 0.827 mm^2 during opening and 0.836 mm^2 during closing. The maximum absolute relative difference between the two directions is approximately 1.10%, also occurring at 30% valve position.

Across the 17 positions for which opening and closing measurements are directly compared, the mean absolute relative difference is approximately 0.35%. Furthermore, the sign of the difference changes across the operating range rather than showing a systematic offset between opening and closing.

These results indicate that hysteresis is small relative to the total effective area range. The commanded valve position can therefore be related to the effective flow area with little dependence on whether the operating point is approached from a higher or lower position. The main feature that must be considered in the proportional valve characteristic is consequently the initial opening offset, followed by the approximately linear active operating range.

5.2 Distributor Characterization

The rotary distributor was characterized by changing its input shaft angle and recording the corresponding air mass flow and pressure conditions. The test was performed at an ambient pressure of approximately 1.003 bar and an air temperature of 23 °C. The angular sweep extended from the closed position to 180° input shaft angle.

Unlike the proportional valve, the pressure ratio across the distributor changes substantially as the passage opens and closes. At the restricted positions close to the beginning of the angular sweep, the measured pressure ratio remains below the critical value and the flow is choked. At 30°, the measured pressure ratio is approximately 0.490, whereas at 33° it increases to approximately 0.578. The distributor therefore changes from choked to non-choked flow between these two measurement points.

The non-choked condition remains through the central part of the characteristic up to 153°, where the measured pressure ratio is approximately 0.598. At 156°, the measured pressure ratio decreases to approximately 0.509, falling below the critical pressure ratio as the distributor approaches the closed condition.

The same effective area expression is used for all measurement points. The distinction between choked and non-choked conditions is introduced through the pressure ratio used in the isentropic flow function, ψ. When the measured pressure ratio falls below the critical value, the critical pressure ratio is used, otherwise, the measured pressure ratio is retained. The complete calculation procedure is described in Appendix C.

5.2.1 Effective Flow Area over the Angular Range

A finite air flow was measured when the distributor was in its closed position. The corresponding effective leakage area used as the reference in the calculation is approximately 1.361 mm^2. This value is subtracted from the calculated effective area to obtain the leakage corrected characteristic, $A_{\text{eff,off}}$, as explained in Appendix C.The use of this constant correction assumes that the closed position leakage contribution remains approximately constant over the angular sweep.

Figure 5.4 presents the resulting leakage corrected effective area as a function of distributor input shaft angle.

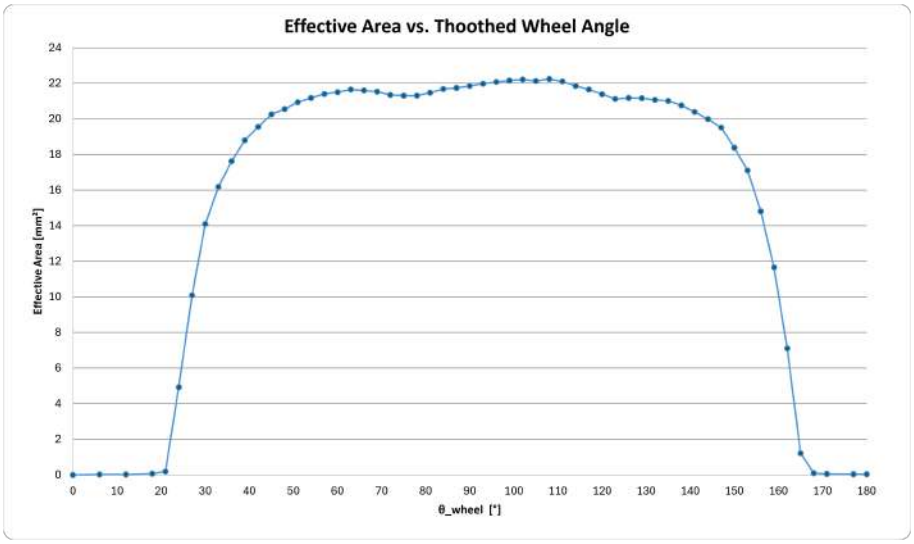


Figure 5.4: Leakage corrected effective flow area of distributor 160 A as a function of input shaft angle.

The distributor remains close to its closed condition during the first part of the angular sweep. At 21°, the corrected effective area is only 0.193 mm^2. A rapid increase in effective area then occurs between 21° and approximately 45°. The effective area increases to 4.925 mm^2 at 24°, 10.094 mm^2 at 27°, 14.098 mm^2 at 30°, and 20.260 mm^2 at 45°.

After the initial opening region, the characteristic becomes considerably flatter. From approximately 54° through the central part of the angular range, the corrected effective area remains close to 21–22 mm^2. The maximum experimentally determined value is

$$A_{\text{eff,off,max}} = 22.240 \text{ mm}^2,$$

which occurs at an input shaft angle of 108°. The air mass flow rate at this point is approximately 39.14 kg/h under the applied test conditions. The experimentally determined effective flow area should not be interpreted as the geometric overlap area presented in Chapter 4. The effective area represents the flow capacity of the real component under the applied test conditions and therefore includes the influence of the actual flow through the distributor passages.

The broad region around the maximum shows that, within the central high area region, relatively small changes in input shaft angle produce only small changes in effective flow area. This contrasts with the opening and closing regions, where the effective area changes rapidly with angle. The resulting characteristic therefore contains three distinct regions: an initial opening transition, a broad high area region, and a final closing transition.

Beyond approximately 135°, the effective area begins to decrease more rapidly. It falls from 21.01 mm^2 at 135° to 17.11 mm^2 at 153° and 14.82 mm^2 at 156°. A further reduction to 7.12 mm^2 occurs at 162° and to 1.22 mm^2 at 165°. By 168°, the leakage corrected area has decreased to approximately 0.093 mm^2 and subsequently remains close to zero until the end of the angular sweep.

The transition between choked and non-choked conditions follows the same general evolution. Choked flow occurs when the distributor opening is strongly restricted near the beginning and end of the angular window, while the central high area region operates under non-choked conditions. No discontinuity in the effective area characteristic is observed at the transition between these regimes, and the calculated area evolves continuously with input shaft angle.

The measured characteristic therefore provides a direct relationship between the distributor input shaft angle and its effective flow area. In particular, the rapid area variation at the opening and closing edges means that the angular position is most influential in these regions, whereas the central part of the characteristic is less sensitive to small angular variations.

5.3 Flow Characterization Summary

The component tests identify two different flow characteristics within the hydrogen delivery system. The proportional valve presents an initial opening threshold at approximately 8% commanded position followed by a highly linear effective area response. The extrapolated effective area at full opening is 3.513 mm^2, corresponding to a discharge coefficient of 0.716 for the geometric area considered in the calculation. The opening and closing measurements also show limited hysteresis, with a maximum absolute relative difference of approximately 1.10%.

The rotary distributor presents a strongly angle dependent characteristic during opening and closing, separated by a broad high area region. After correction for the closed position leakage, the maximum effective area is 22.240 mm^2 at 108° input shaft angle. The distributor also operates under both choked and non-choked flow conditions during a complete angular sweep, with the transition determined by the instantaneous pressure ratio across the component.

These results provide the experimentally determined relationships between the control or angular position of each component and its effective flow area. The proportional valve characteristic defines the metering response of the system, while the distributor characteristic defines the variation in flow capacity associated with its rotational position.

Chapter 6

Engine Testing

This chapter presents the experimental engine test campaign conducted to evaluate the hydrogen delivery system under different operating conditions and hardware configurations. The engine test facilities and the experimental programme are first described, including the operating points and the modifications introduced in each test campaign.

The baseline configuration is then analysed over the investigated engine speed and load range through the main mixture, performance, and emission parameters. This is followed by direct comparisons of the effects of connection hose geometry, check valve and nozzle configuration, and start of injection on the pressure dynamics of the fuel delivery system and on the resulting engine operation.

6.1 Engine Test Facilities

The experimental campaign was carried out using the engine test bench available at the Piston Machine Laboratory. The facility consists of a modular containerized test cell designed for internal combustion engine testing under controlled operating conditions.

The engine is coupled to an eddy current dynamometer, allowing operation at constant engine speed while varying the load. Engine coolant, lubricating oil, and charge air temperatures are regulated by dedicated conditioning units, while heat rejection is provided by an external dry cooler to maintain stable operating conditions throughout the tests.

The test bench is operated from a dedicated control room equipped with the data acquisition and monitoring system used to record and supervise the engine operating parameters in real time.

Fuel supply cylinders and the associated gas supply and control system are installed outside the facility. Safety measures include automated shutdown procedures and a ventilation system designed to prevent the accumulation of combustible gases.

Figure 6.1 presents the engine test bench used during the experimental campaign. The monitoring and data acquisition room, from which all experiments were controlled, is shown in Figure 6.2. The hydrogen and syngas cylinders together with the gas supply and control system are presented in Figure 6.3, where the external dry cooler can also be observed in the background.



Figure 6.1: External view of the engine test facility.



Figure 6.2: Engine monitoring and control room.



Figure 6.3: Gas supply and control system.

6.2 Engine Test Programme

A total of nine test campaigns, designated VSR001 through VSR009, were conducted on the DEUTZ TCD 3.6 L4 engine with distributor 160 A and proportional valve 620 B installed. Each campaign was performed at eleven operating points (MP001–MP011), covering engine speeds of 1200, 1500, and 1800 rpm at target indicated mean effective pressures between 3 and 12 bar, as defined in Table 6.1.

For the hardware comparison campaigns, the modifications were applied to cylinder 4, while cylinder 1 remained in the baseline configuration and provided a direct reference. VSR009 differed from this approach because the start of injection was changed without a cylinder 4 specific hardware modification.

Table 6.1: Engine operating points used in each test campaign

Measuring point	Engine speed [rpm]	Target IMEP [bar]
MP001	1200	3
MP002	1200	6
MP003	1200	9
MP004	1500	3
MP005	1500	6
MP006	1500	9
MP007	1500	12
MP008	1800	3
MP009	1800	6
MP010	1800	9
MP011	1800	12

Of the nine campaigns, VSR001, VSR003, and VSR007 were conducted for diagnostic purposes and are not included in the main analysis of this dissertation. VSR001 was performed with a different distributor model and serves as an internal laboratory reference. VSR003 was a configuration check in which the connection hoses of two cylinders were swapped to assess whether

the installation direction had any measurable effect on engine behaviour. No significant difference was observed.

VSR007 employed a check valve spring with a stiffness significantly higher than the reference, which resulted in cylinder 4 receiving insufficient fuel throughout the test. The dataset is therefore not representative of the intended operating condition. The remaining six campaigns form the basis of the experimental analysis presented in this chapter.

6.2.1 VSR002 (Baseline Configuration)

VSR002 constitutes the baseline test campaign. The injection system was assembled in its nominal configuration, with the standard connection hose on all four cylinders, check valves and nozzles installed, and a start of injection of SOI $= -340\,\mathrm{dCA}$ relative to combustion TDC, defined as $0\,\mathrm{dCA}$ in the injection timing reference. In the 0–720 dCA representation used for the pressure traces in this chapter, the combustion TDC of cylinder 4 corresponds to approximately $360\,\mathrm{dCA}$. Figure 6.4 shows the engine as configured for this campaign. All subsequent campaigns are compared against this baseline.

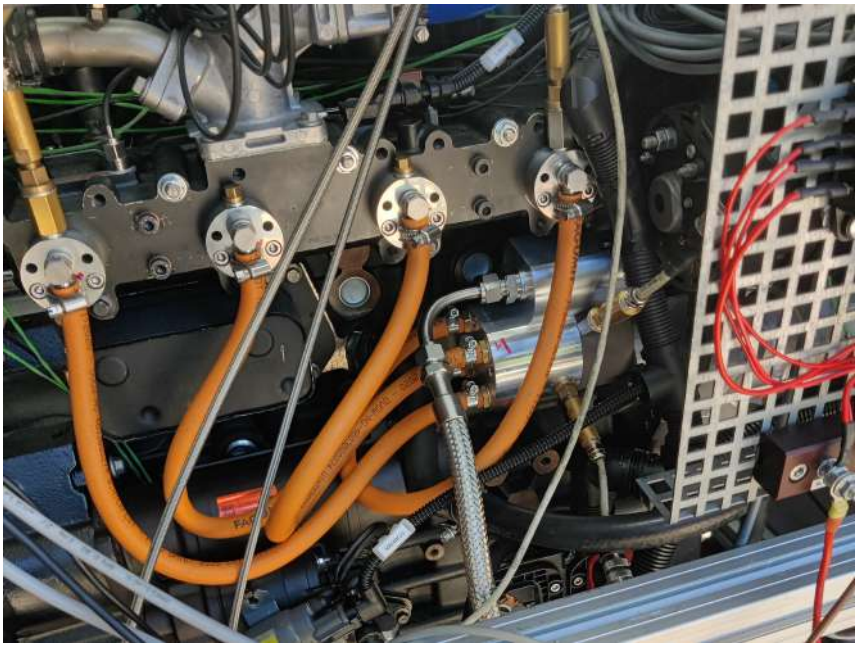


Figure 6.4: Engine test bench in the baseline configuration used for campaign VSR002.

6.2.2 VSR004 (Extended Hose Length on Cylinder 4)

In VSR004, the connection hose on cylinder 4 was extended with another similar hose making it twice the standard length, while all other system components and settings remained identical to VSR002. The purpose of this test was to assess the effect of increased hose length and internal volume on the injection pressure dynamics and the resulting combustion behaviour of cylinder 4. Figure 6.5 shows the modified hose installation on cylinder 4 as fitted during this campaign.



Figure 6.5: Extended connection hose installed on cylinder 4 for campaign VSR004.

6.2.3 VSR005 (Reduced Hose Diameter on Cylinder 4)

VSR005 replaced the standard hose on cylinder 4 with a hose of smaller inner diameter, keeping hose length and all other parameters equal to VSR002. Reducing the inner diameter increases the pneumatic resistance of the connection, which modifies the flow rate and pressure dynamics upstream of the nozzle. Figure 6.6 shows the reduced diameter hose installed during this campaign.

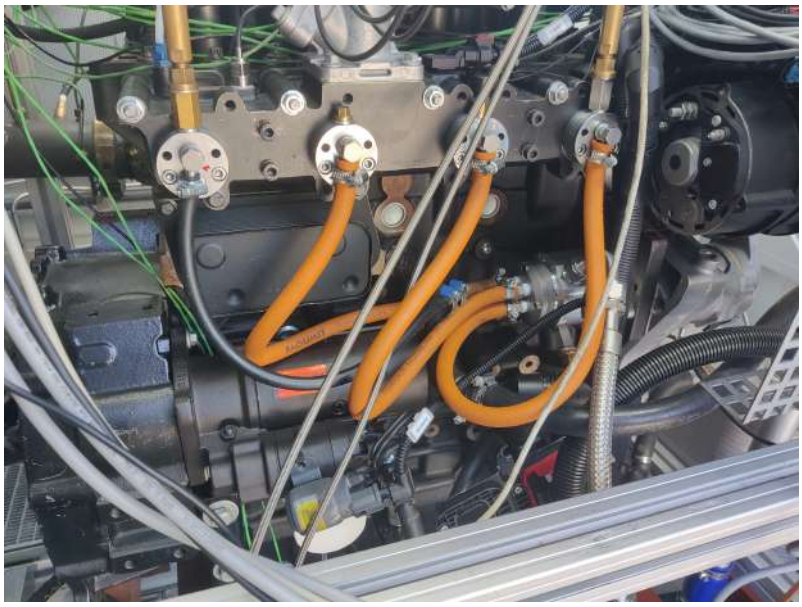


Figure 6.6: Reduced diameter connection hose installed on cylinder 4 for campaign VSR005.

6.2.4 VSR006 (Removal of Check Valve on Cylinder 4)

In VSR006, the check valve on the nozzle of cylinder 4 was removed, leaving the nozzle in place. In the baseline configuration, the check valve provides pressure isolation between the hydrogen delivery line and the intake port and restricts reverse flow from the intake side into the fuel line. Its removal therefore allows stronger pressure communication between the intake port and the hydrogen line. The nozzle and hose dimensions were unchanged from the baseline. Figure 6.7 shows the check valve spring and spring pre-tensioner that were removed for this campaign.



Figure 6.7: Check valve spring and spring pre-tensioner removed from the nozzle of cylinder 4 for campaign VSR006.

6.2.5 VSR008 (Removal of Check Valve and Nozzle on Cylinder 4)

VSR008 extended the configuration of VSR006 by additionally removing the nozzle from cylinder 4, leaving the connection hose open directly into the intake port. This eliminates both the flow restriction of the nozzle orifice and the sealing function of the check valve simultaneously. The comparison between VSR002, VSR006, and VSR008 therefore allows the individual contributions of the nozzle restriction and the check valve to be assessed. Figure 6.8 shows the open hose end on cylinder 4 as tested in this campaign.



Figure 6.8: Connection hose on cylinder 4 with nozzle and check valve removed for campaign VSR008.

6.2.6 VSR009 (Modified Start of Injection Timing)

VSR009 investigated the effect of injection timing by shifting the start of injection from SOI $=$ $-340\,\mathrm{dCA}$ (baseline) to SOI $= -300\,\mathrm{dCA}$, corresponding to a later injection event closer to combustion TDC. All hardware components were identical to the baseline VSR002 configuration on all four cylinders. No modification was made to cylinder 4 specifically. This campaign therefore provides a direct assessment of injection phasing on engine performance and emissions, independent of any hardware change.

6.3 Comparative Analysis Structure

The six relevant campaigns are analyzed through three defined comparisons, each targeting a specific system parameter. To keep the main discussion concise, the cross campaign comparison presented in this chapter is focused on measuring point MP010 (1800 rpm, 9 bar IMEP), representing a high load operating condition where the effects of the investigated modifications are more evident. This point corresponds to the highest target IMEP investigated at all three engine speeds. The corresponding comparisons at low and medium load, represented by MP001 and MP005, are provided in Appendix E. The three comparisons are:

- **Hose geometry:** VSR002 vs. VSR004 vs. VSR005: effect of hose length and diameter on injection dynamics and combustion.
- **Check valve and nozzle:** VSR002 vs. VSR006 vs. VSR008: effect of removing the anti return valve and the nozzle restriction.
- **Injection timing:** VSR002 vs. VSR009: effect of the start of injection timing on the fuel delivery and engine response.

6.4 Individual Campaign Results

To keep the discussion concise, only the results obtained for the baseline configuration, VSR002, are presented in the main text. The graphs corresponding to the other test campaigns show only limited variation relative to the baseline results and are therefore provided in Appendix D. This approach allows the main trends to be discussed without extending this work with repetitive figures.

6.4.1 VSR002 (Baseline)

The results obtained for the baseline configuration, VSR002, are presented in Figures 6.9 to 6.13. The contour maps include brake specific fuel consumption, brake specific NO_x emissions, thermal efficiency, lambda, and injected hydrogen mass per cycle, represented as functions of engine speed and IMEP.

The contour maps provide a continuous representation of the measured quantities over the investigated operating range. However, the discussion is primarily based on the experimental operating points indicated by the black markers, while the intermediate regions result from interpolation. Consequently, small local variations in the contour lines should not be interpreted as additional measured behaviour.

Figure 6.9 shows a clear reduction in brake specific fuel consumption as the engine load increases. At 1200 rpm, BSFC decreases from 124.4 g/kWh at 3 bar IMEP to 82.9 g/kWh at 6 bar and 78.3 g/kWh at 9 bar. A similar behaviour is observed at the other engine speeds, with the minimum measured value of 75.4 g/kWh occurring at 1500 rpm and 12 bar IMEP. At 1800 rpm, BSFC decreases from 159.7 g/kWh at 3 bar to 78.5 g/kWh at 12 bar.

For a given load, increasing engine speed generally leads to higher BSFC, particularly at low load. At 3 bar IMEP, for example, BSFC increases from 124.4 g/kWh at 1200 rpm to 133.3 g/kWh at 1500 rpm and 159.7 g/kWh at 1800 rpm. This behaviour is consistent with an increased relative contribution of friction and other internal mechanical losses at higher engine speeds, particularly when the engine load is low. The effect becomes considerably smaller at higher IMEP. At 9 bar, the measured values are 78.3, 78.6, and 82.8 g/kWh at 1200, 1500, and 1800 rpm, respectively. The results therefore indicate that the most favourable fuel consumption region is located at medium to high load and moderate engine speed.

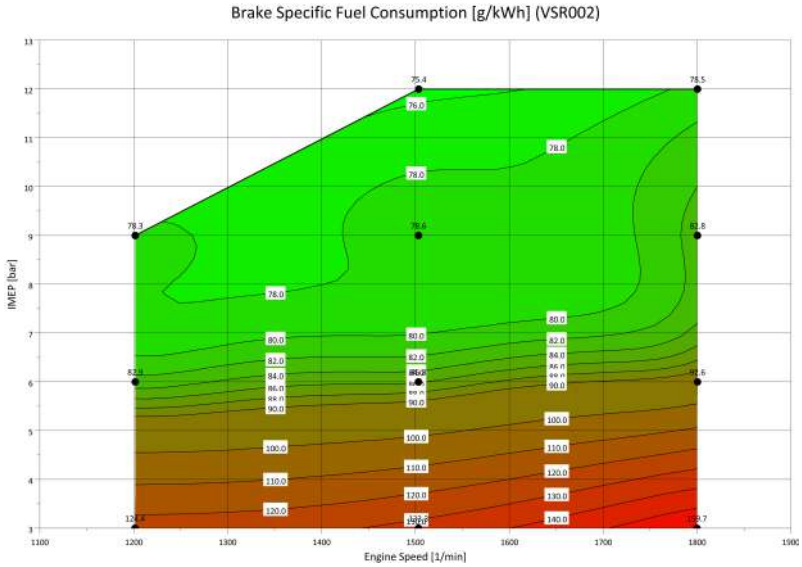


Figure 6.9: Contour map of brake specific fuel consumption as a function of engine speed and IMEP for campaign VSR002 (baseline configuration).

The brake specific NO_x emissions presented in Figure 6.10 remain low over most of the investigated operating range. Values between approximately 0.0 and 0.3 g/kWh are obtained at the majority of the measured operating points. The main exception occurs at 1200 rpm and 9 bar IMEP, where a value of 4.2 g/kWh is measured. A second increase is observed at 1500 rpm and 12 bar IMEP, where the value reaches 1.1 g/kWh. At 1800 rpm, even at 12 bar IMEP, the measured value remains at 0.2 g/kWh.

Comparison with Figure 6.12 shows that the increase in NO_x coincides with operation at lower lambda values. The highest NO_x value, obtained at 1200 rpm and 9 bar IMEP, corresponds to $\lambda = 2.1$, while the point at 1500 rpm and 12 bar corresponds to $\lambda = 2.3$. In contrast, the very lean operating points generally produce substantially lower NO_x emissions. This behaviour is physically consistent with the strong dependence of thermal NO_x formation on combustion temperature: moving from very lean operation towards lower lambda values can increase combustion temperature and consequently promote NO_x formation. Nevertheless, the 4.2 g/kWh value is considerably higher than the neighbouring measured points and should therefore be treated as a specific experimental result rather than using the interpolated region to infer the same behaviour over a wider operating range.

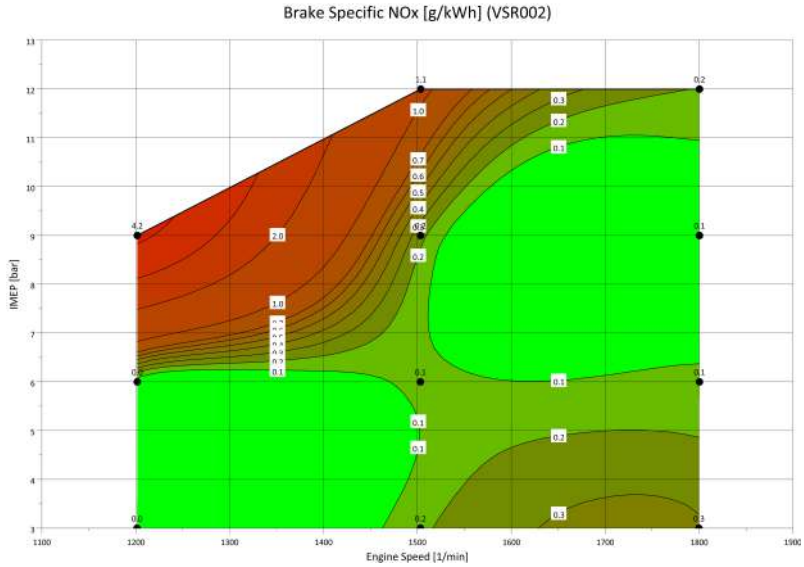


Figure 6.10: Contour map of brake specific NO_x emissions as a function of engine speed and IMEP for campaign VSR002 (baseline configuration).

The thermal efficiency map in Figure 6.11 presents the inverse trend to that observed for BSFC. At 1200 rpm, thermal efficiency increases from 24.2% at 3 bar IMEP to 36.2% at 6 bar and 38.3% at 9 bar. At 1500 rpm, the corresponding increase is from 22.5% at 3 bar to 35.0% at 6 bar, 38.2% at 9 bar, and a maximum measured value of 39.8% at 12 bar. At 1800 rpm, efficiency increases from 18.8% at 3 bar to 38.2% at 12 bar.

The increase in efficiency with IMEP is consistent with the reduction in the relative contribution of mechanical losses as the engine load increases. The influence of engine speed is also more pronounced at low load. At 3 bar IMEP, efficiency decreases from 24.2% at 1200 rpm to 18.8% at 1800 rpm, whereas at 9 bar the corresponding values decrease only from 38.3% to 36.2%. Therefore, the results identify the higher load region, particularly around 1500 rpm, as the region of highest thermal efficiency within the tested operating map.

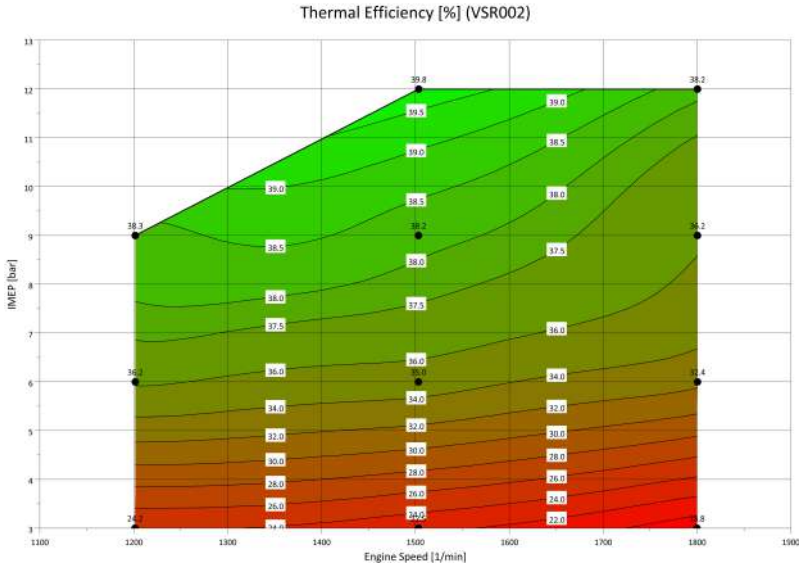


Figure 6.11: Contour map of thermal efficiency as a function of engine speed and IMEP for campaign VSR002 (baseline configuration).

Figure 6.12 shows that the engine operates under lean conditions throughout the complete measured operating range. At 3 bar IMEP, lambda remains almost independent of engine speed, with values between 5.1 and 5.2. Increasing the engine load produces a clear reduction in lambda. At 1200 rpm, lambda decreases from 5.1 at 3 bar to 3.0 at 6 bar and 2.1 at 9 bar. At 1500 rpm, the corresponding values are 5.2, 3.3, 2.6, and 2.3 between 3 and 12 bar IMEP. At 1800 rpm, lambda decreases from 5.2 at 3 bar to 2.7 at 12 bar.

This trend is consistent with the increase in hydrogen quantity required to increase engine load. As more hydrogen is supplied relative to the available air, the mixture becomes less lean, although all measured operating points remain lean relative to stoichiometric operation. A speed effect is also visible at medium and high load. For example, at 9 bar IMEP, lambda increases from 2.1 at 1200 rpm to 2.6 at 1500 rpm and 3.0 at 1800 rpm. The present results establish this variation experimentally, although the lambda map alone is not sufficient to determine whether it results from changes in the cylinder air charge, volumetric efficiency, or other operating parameters.

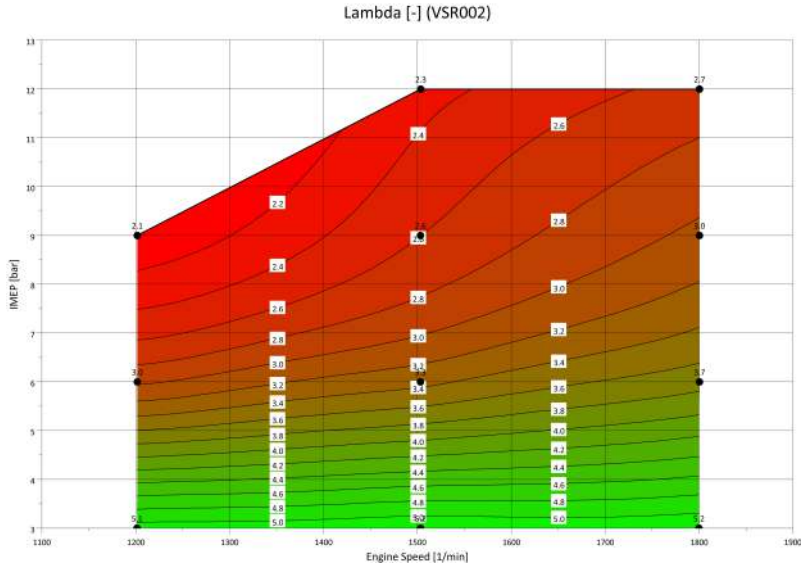


Figure 6.12: Contour map of lambda as a function of engine speed and IMEP for campaign VSR002 (baseline configuration).

The injected hydrogen mass shown in Figure 6.13 increases primarily with engine load. At 1200 rpm, the measured mass increases from 5.7 mg/cycle at 3 bar IMEP to 10.1 mg/cycle at 6 bar and 15.6 mg/cycle at 9 bar. At 1500 rpm, the values increase from 6.1 mg/cycle at 3 bar to 10.3, 15.0, and 20.1 mg/cycle at 6, 9, and 12 bar IMEP, respectively. A similar progression is obtained at 1800 rpm, where the injected mass increases from 6.7 mg/cycle at 3 bar to 20.6 mg/cycle at 12 bar.

The approximately proportional increase in injected hydrogen mass with IMEP is consistent with the additional fuel energy required to produce higher indicated work per cycle. In comparison, the effect of engine speed is considerably smaller and is not fully monotonic at every load. At 9 bar IMEP, for example, the values are 15.6, 15.0, and 15.8 mg/cycle at 1200, 1500, and 1800 rpm, respectively. Therefore, the results support a strong dependence on load but do not support a simple monotonic relationship between injected mass per cycle and engine speed over the complete operating range. The increase in hydrogen mass with load is also consistent with the simultaneous reduction in lambda observed in Figure 6.12.

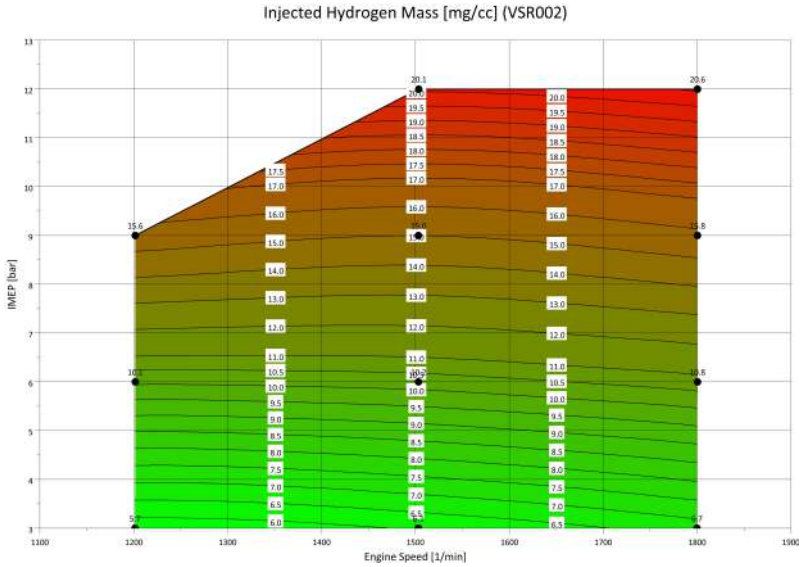


Figure 6.13: Contour map of injected hydrogen mass per cycle as a function of engine speed and IMEP for campaign VSR002 (baseline configuration).

Overall, the five maps present a consistent description of the baseline configuration. Increasing engine load requires a higher injected hydrogen mass and is accompanied by a reduction in lambda, while brake specific fuel consumption decreases and thermal efficiency increases. The influence of engine speed is more pronounced at low load, where higher BSFC and lower efficiency are observed at the highest tested speed. The NO_x results remain low over most of the operating range, with the main increase occurring at the operating points with the lowest lambda values. Taken together, these results indicate that the baseline configuration operates predominantly under very lean conditions, with the most favourable efficiency and fuel consumption obtained in the medium to high load region of the tested map.

6.5 Hose Geometry Comparison: VSR002, VSR004 and VSR005

The effect of the connection hose geometry is evaluated by comparing the baseline configuration VSR002 with VSR004, in which the hose length of cylinder 4 was increased, and VSR005, in which a smaller inner diameter was used. The comparison is performed at MP010 (1800 rpm and 9 bar IMEP) and considers the pressure upstream of the distributor, the cylinder 4 injection line, the intake and exhaust manifolds near cylinder 4, and the in-cylinder pressure. The pressure traces are presented over a complete 720 dCA engine cycle in Figures 6.14 to 6.18.

6.5.1 High Load: MP010

The distributor upstream pressure shown in Figure 6.14 presents a similar periodic behaviour for the three configurations. The pressure varies within a relatively narrow range over the 720 dCA

cycle, with repeated structures separated by approximately 180 dCA as a consequence of the sequential fuel delivery to the four cylinders.

VSR002 and VSR005 remain relatively close over most of the cycle, whereas VSR004 generally exhibits a slightly lower upstream pressure. However, the overall waveform remains similar for all configurations. Since this measurement is located upstream of the distributor, the signal represents the behaviour of the common fuel supply and cannot be associated exclusively with cylinder 4.

The relatively small differences between the three campaigns indicate that changing the cylinder 4 hose geometry does not substantially alter the overall pressure dynamics upstream of the distributor. From a system perspective, this is favourable, since the modifications remain predominantly local to the cylinder branch rather than causing a major disturbance in the common fuel supply.

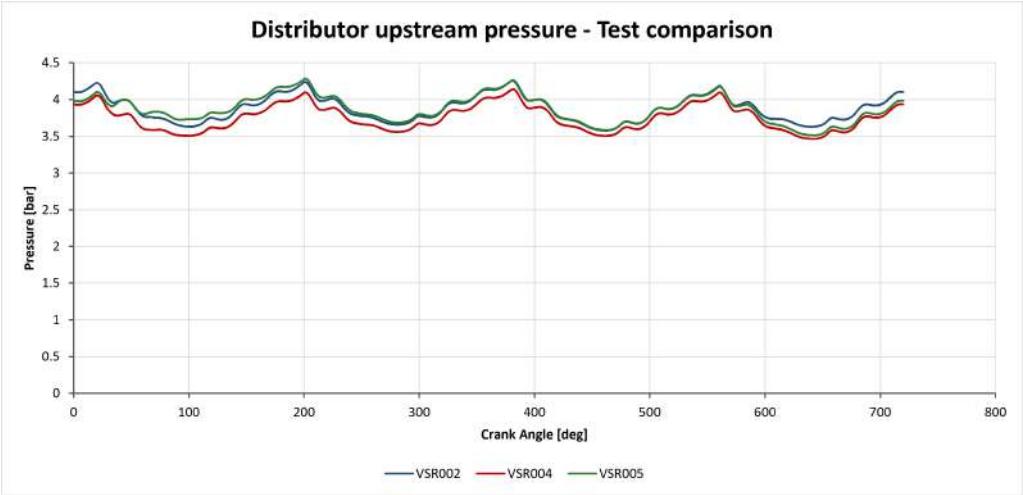


Figure 6.14: Comparison of the distributor upstream pressure traces for MP010.

The strongest effect of hose geometry is observed in the injection line pressure shown in Figure 6.15. All three configurations show a rapid pressure increase at the beginning of the fuel delivery event, but the subsequent evolution differs considerably.

VSR002 reaches approximately 2.8 bar and maintains an elevated pressure over a relatively long crank angle interval. VSR004 presents a slightly lower initial peak and a lower pressure level during the same period. VSR005 produces the highest initial peak, close to 3.0 bar, followed by an earlier and more pronounced decrease to approximately 1.9 bar before the pressure gradually recovers.

These differences show that both hose length and diameter influence the transient response of the hydrogen delivery line. Increasing the hose length changes the internal volume and the propagation of pressure waves, whereas reducing the inner diameter increases the flow restriction and modifies the dynamic response of the gas column. The effect is stronger for VSR005, where the reduced diameter produces a larger deviation from the baseline pressure trace.

A larger pressure fluctuation is not necessarily beneficial, since a higher local pressure does not directly imply a higher hydrogen flow. In a more restrictive line, pressure can increase upstream of the restriction while the instantaneous mass flow is simultaneously reduced. Large transient variations can therefore make the fuel delivery less uniform and may influence mixture preparation and combustion repeatability.

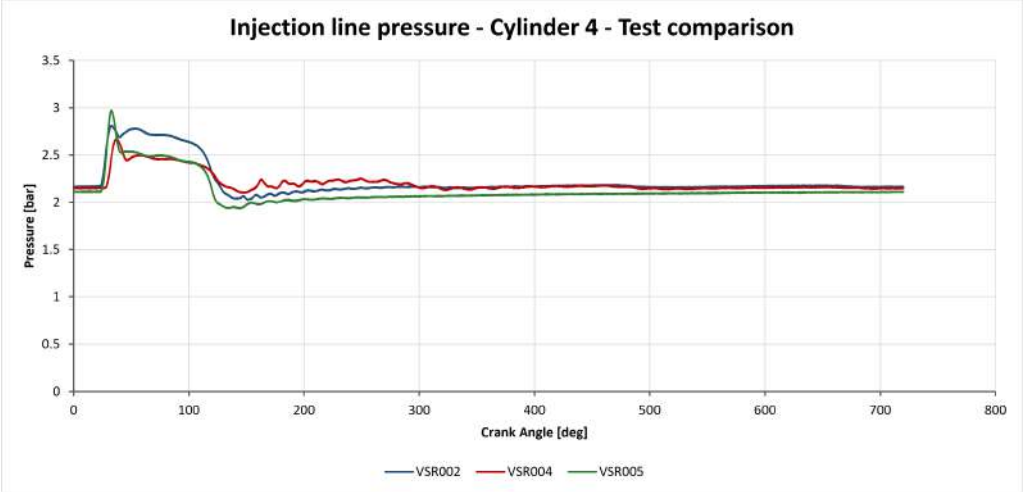


Figure 6.15: Comparison of the injection line pressure traces on cylinder 4 for MP010.

The intake manifold pressure presented in Figure 6.16 contains the contribution of all four cylinders because the sensor is installed in the common intake manifold, although positioned close to cylinder 4. The main pressure structures repeat approximately every 180 dCA, reflecting the successive intake events of the four-cylinder engine.

Considering the combustion TDC of cylinder 4 at approximately 360 dCA, its nominal intake stroke occurs in the preceding 0–180 dCA interval. During this part of the cycle, the manifold pressure decreases from an initial local maximum to a minimum around 120–130 dCA. Similar structures subsequently appear at approximately 180 dCA intervals due to the remaining cylinders.

VSR002 and VSR004 remain very close over most of the cycle, whereas VSR005 generally presents a lower manifold pressure and deeper pressure minimum. This indicates that the reduced diameter configuration is also associated with a small change in the overall intake system response.

Short and relatively sharp pressure fluctuations are superimposed on the main intake manifold waveform. These disturbances appear repeatedly during the engine cycle and are observed at approximately 180 dCA intervals. Their periodic character suggests that they are strongly associated with the normal pressure wave interaction generated by the successive cylinder events in the common intake manifold instead of a backfire event.

Nevertheless, if present, backfire would be undesirable because combustion propagation into the intake system would disturb cylinder filling, increase pressure loading of the intake components, and reduce combustion stability.

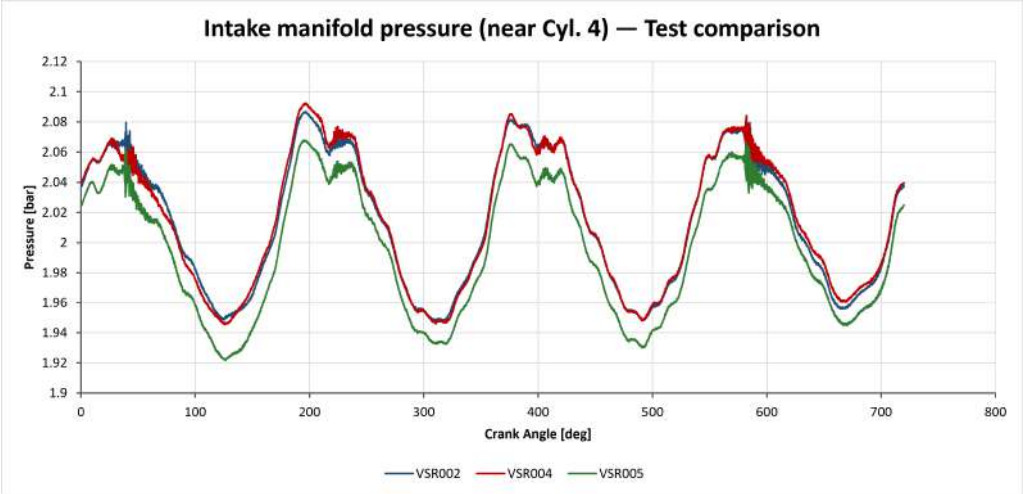


Figure 6.16: Comparison of the intake manifold pressure traces on cylinder 4 for MP010.

A clear distinction between the hose configurations is observed in the in-cylinder pressure traces presented in Figure 6.17. VSR002 and VSR004 are almost coincident throughout compression and combustion and both reach a maximum pressure of approximately 80 bar near 370 dCA, corresponding to approximately 10 dCA after combustion TDC. Their injected hydrogen masses are also very similar, with 15.8 mg/cycle for VSR002 and 15.6 mg/cycle for VSR004.

The close agreement between these two configurations indicates that, although increasing the hose length modifies the injection line pressure dynamics, it has little effect on the resulting combustion pressure at MP010.

In contrast, VSR005 reaches a maximum cylinder pressure of only approximately 66 bar, while the position of the pressure maximum remains close to that observed for VSR002 and VSR004. The corresponding injected hydrogen mass is 15.4 mg/cycle. Therefore, the hydrogen mass decreases only slightly relative to the baseline, whereas the reduction in peak cylinder pressure is considerably larger. The lower combustion pressure cannot therefore be explained by fuel quantity alone.

The reduced hose diameter substantially changes the transient pressure evolution in the injection line and may consequently modify the temporal distribution of the hydrogen flow and the resulting mixture formation before combustion. This provides a possible explanation for the lower cylinder pressure despite the similar total injected hydrogen mass. However, the available measurements do not allow the individual contributions of mixture distribution and combustion development to be quantified.

From an engine operation perspective, the lower cylinder pressure obtained with VSR005 is undesirable if the objective is uniform cylinder contribution. A lower combustion pressure reduces the work produced by cylinder 4 relative to the remaining cylinders.

No clear indication of pre-ignition is observed in the cylinder pressure traces. The spark-current peak occurs at approximately 341 dCA and the main combustion pressure rise develops

subsequently, with the pressure maximum occurring near 370 dCA. No abnormal pressure rise substantially preceding the ignition event is visible.

Similarly, no pronounced high frequency pressure oscillations are visible around the cylinder pressure maximum that would allow knock to be identified from the presented traces.

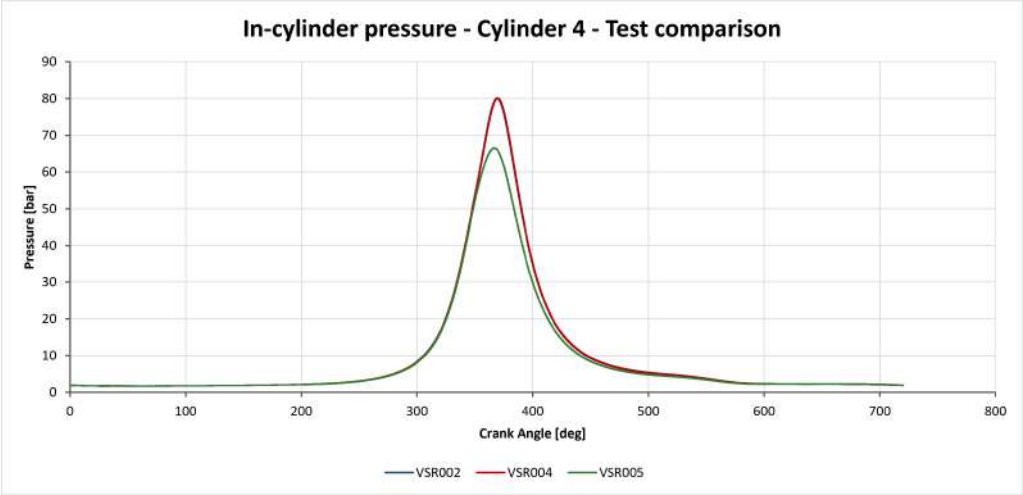


Figure 6.17: Comparison of the in-cylinder pressure traces on cylinder 4 for MP010.

The exhaust manifold pressure presented in Figure 6.18 contains the successive exhaust events of all four cylinders, since the pressure sensor is installed in the common exhaust manifold close to cylinder 4. The main pressure structures repeat approximately every 180 dCA as a consequence of the four cylinder firing sequence.

For cylinder 4, the combustion TDC occurs at approximately 360 dCA. The subsequent expansion stroke therefore extends through the following part of the cycle and is followed by the exhaust event. The pressure pulse observed approximately between 550 and 620 dCA is consequently associated with the exhaust process of cylinder 4.

This region also presents the clearest difference between the three configurations. VSR002 produces the highest pressure pulse, VSR004 remains only slightly lower, and VSR005 shows a clearly reduced amplitude. This ordering is consistent with the corresponding in-cylinder pressure results, where VSR005 produces a substantially lower combustion pressure.

The lower exhaust pressure contribution of VSR005 is therefore consistent with the reduced combustion contribution of cylinder 4. While a lower exhaust pressure pulse is not inherently harmful, in this case it is associated with lower cylinder work rather than an improvement in the gas exchange process. It should therefore be interpreted as a consequence of the reduced combustion performance of cylinder 4 rather than as a beneficial reduction in exhaust pressure.

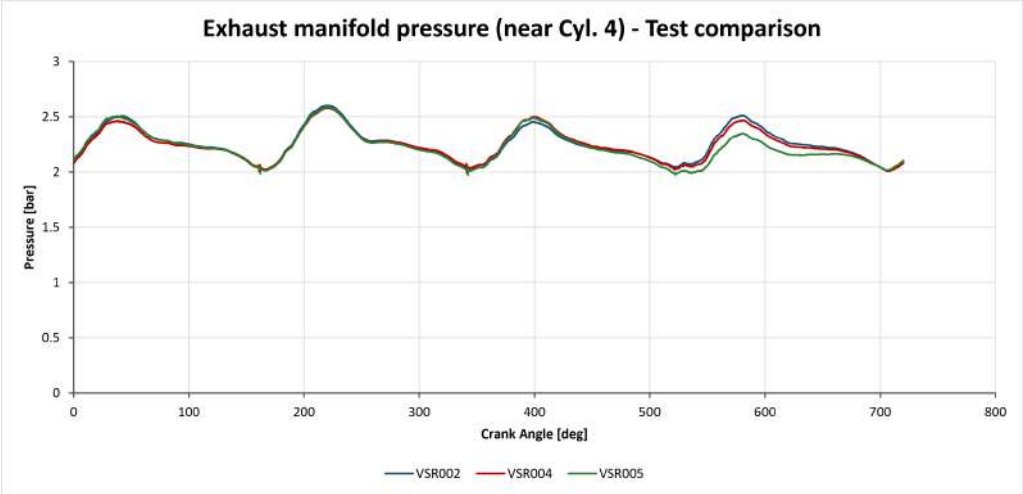


Figure 6.18: Comparison of the exhaust manifold pressure traces on cylinder 4 for MP010.

Overall, the results show that the connection hose geometry directly influences the transient behaviour of the hydrogen delivery system. Increasing the hose length in VSR004 modifies the injection line pressure response, but produces only limited changes in the in-cylinder and manifold pressure traces relative to the baseline. Under the investigated high load condition, the effect of the extended hose on the resulting combustion behaviour is therefore relatively small.

In contrast, the reduced hose diameter used in VSR005 produces a more pronounced response. The injection line pressure shows a higher initial peak and a stronger subsequent pressure variation, while the peak in-cylinder pressure decreases from approximately 80 bar in VSR002 to 66 bar in VSR005. This occurs despite only a small reduction in injected hydrogen mass, from 15.8 mg/cycle to 15.4 mg/cycle, showing that the change in combustion cannot be explained by fuel quantity alone. The modified line dynamics are therefore likely to affect the temporal delivery of hydrogen and the resulting mixture formation. The lower cylinder pressure is also reflected in the exhaust manifold during the cylinder 4 exhaust event, indicating a reduced contribution from this cylinder and a greater cylinder-to-cylinder imbalance. Consequently, for MP010, reducing the hose diameter has a more detrimental effect on engine operation than increasing the hose length.

The individual cylinder IMEP provides additional evidence of this behaviour. Cylinder 4, which was the only cylinder subjected to the hardware modifications, presents a lower IMEP than the remaining cylinders for both modified hose configurations. The reduction is more pronounced for VSR005 than for VSR004, showing that decreasing the hose inner diameter has a stronger detrimental effect on the indicated performance of cylinder 4 than increasing the hose length under the investigated condition. This result is consistent with the more pronounced changes observed in the injection line and in-cylinder pressure traces for the reduced diameter configuration.

The additional low and medium load comparisons presented in Appendix E show that the influence of the reduced hose diameter on the intake manifold is dependent on the operating condition. At MP001 and MP005, VSR005 presents a slightly higher intake manifold pressure than the other configurations, whereas at MP010 it presents the lowest pressure. This inversion indi-

cates that the intake response cannot be attributed solely to the local hose modification. Since the intake manifold is common to all four cylinders and forms part of the turbocharged air system, its pressure response depends on the interaction between the modified cylinder branch and the overall engine operating condition.

6.6 Check Valve and Nozzle Comparison: VSR002, VSR006 and VSR008

The effect of the check valve and nozzle is evaluated by comparing VSR002, VSR006, and VSR008 at MP010 (1800 rpm and 9 bar IMEP). VSR002 represents the baseline configuration, with both the check valve and nozzle installed on cylinder 4. In VSR006, the check valve is removed while the nozzle is retained, whereas VSR008 additionally removes the nozzle, leaving the connection hose directly open to the intake port. This sequential comparison allows the influence of removing the check valve to be distinguished from the additional effect of removing the nozzle.

The comparison includes the distributor upstream pressure, the cylinder 4 injection line pressure, the intake manifold pressure measured near cylinder 4, the in-cylinder pressure, and the exhaust manifold pressure measured near cylinder 4, presented in Figures 6.19 to 6.23. The intake and exhaust pressure sensors are located in common manifolds and therefore record pressure waves generated by all four cylinders, despite their location close to cylinder 4.

6.6.1 High Load: MP010

The distributor upstream pressure shown in Figure 6.19 retains a similar periodic evolution for the three configurations. VSR002 generally operates at a slightly higher pressure level, whereas VSR006 and VSR008 remain very close throughout most of the 720 dCA cycle.

Since this pressure is measured upstream of the distributor, it represents the response of the common fuel supply and cannot be associated exclusively with cylinder 4. The reduction observed after removing the check valve is consistent with a change in the downstream restriction and in the pressure response of the fuel delivery system. The close agreement between VSR006 and VSR008 also indicates that the additional removal of the nozzle has only a small influence at this measurement location.

From a system perspective, the modification therefore affects the common supply pressure to some extent, although the overall periodic behaviour of the distributor supply remains unchanged.

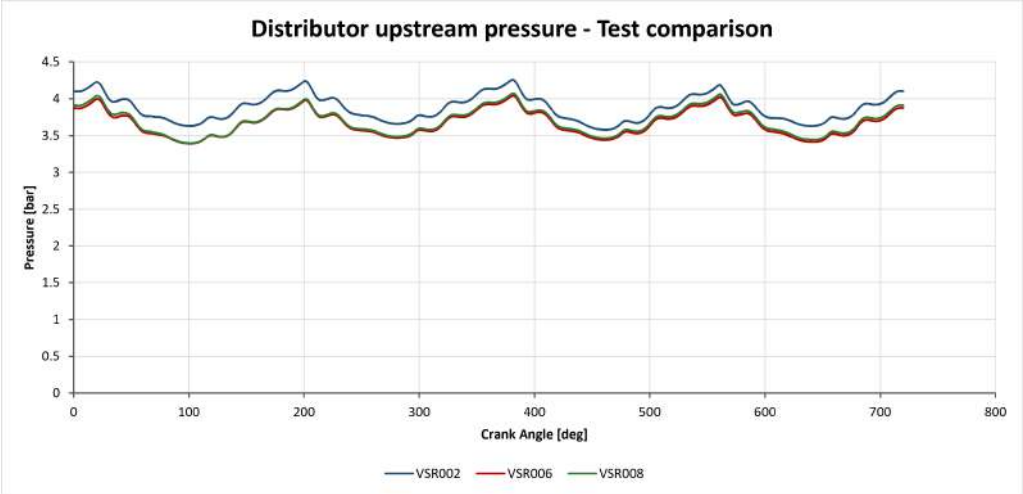


Figure 6.19: Comparison of the distributor upstream pressure traces for MP010.

The effect of the check valve is particularly evident in the injection line pressure shown in Figure 6.20. During the initial fuel delivery event, VSR002 reaches the highest pressure level, while VSR006 and VSR008 operate at slightly lower pressures. More importantly, the behaviour after the initial transient differs significantly.

With the check valve installed in VSR002, the injection line pressure becomes nearly constant after the fuel delivery event. In contrast, VSR006 and VSR008 show periodic pressure fluctuations throughout the remainder of the engine cycle. These fluctuations repeat at approximately 180 dCA intervals and follow a periodicity similar to that observed in the intake manifold.

This behaviour is consistent with the pressure isolation provided by the check valve. When the valve is removed, pressure disturbances from the intake side can propagate into the hydrogen line, producing a stronger pressure coupling between the fuel delivery system and the intake port. The similarity between VSR006 and VSR008 indicates that the loss of this isolation is primarily caused by the removal of the check valve, while removing the nozzle produces only a limited additional change.

This increased pressure coupling is undesirable from a fuel system perspective because the conditions inside the injection line become more sensitive to intake pressure fluctuations. This can reduce the independence and repeatability of successive fuel delivery events. The pressure measurements demonstrate pressure communication between the two systems, although they do not by themselves demonstrate reverse mass flow.

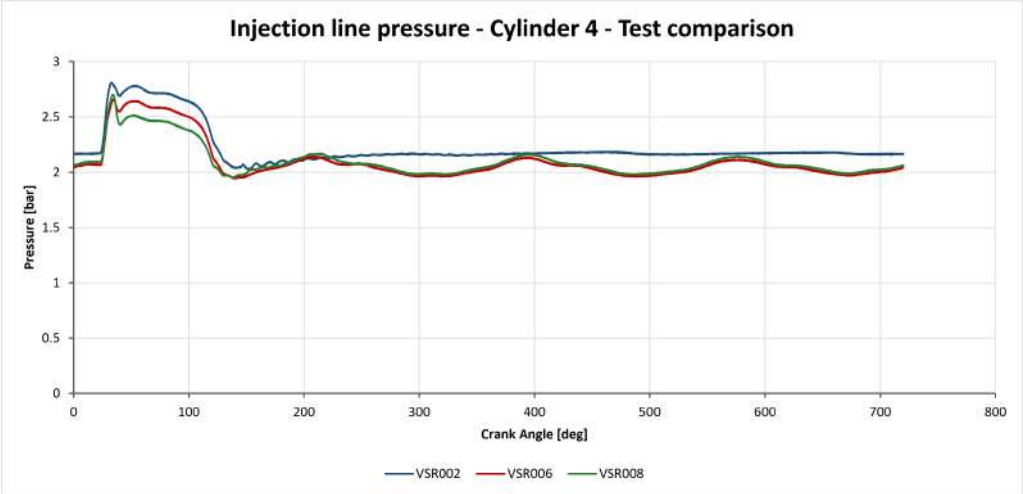


Figure 6.20: Comparison of the injection line pressure traces on cylinder 4 for MP010.

The intake manifold pressure presented in Figure 6.21 shows the periodic response of the common intake system. The principal pressure structures repeat approximately every 180 dCA as a consequence of the successive intake events of the four cylinders.

VSR002 generally presents the highest manifold pressure, while VSR006 shows the lowest values and VSR008 remains slightly above VSR006 over most of the cycle. Since the check valve is removed in both VSR006 and VSR008, the intake port and the cylinder 4 hydrogen line are more strongly pressure coupled, as also demonstrated by the injection line pressure traces. Nevertheless, because the intake manifold is common to all cylinders, the absolute difference between the campaigns cannot be attributed exclusively to cylinder 4.

Short and relatively sharp pressure disturbances are superimposed on the main intake manifold waveform. However, similar disturbances are observed during successive cylinder events and are also present in the baseline configuration. They are therefore not uniquely associated with the removal of the check valve or nozzle.

The available manifold pressure trace does not show an isolated pressure event that can be unambiguously correlated with combustion propagating from cylinder 4 into the intake system. Consequently, the present measurements do not provide sufficient evidence to confirm intake backfire.

If backfire were present, it would represent an undesirable operating condition because combustion propagation into the intake system can disturb cylinder filling, increase pressure loading of the intake components, and reduce combustion stability.

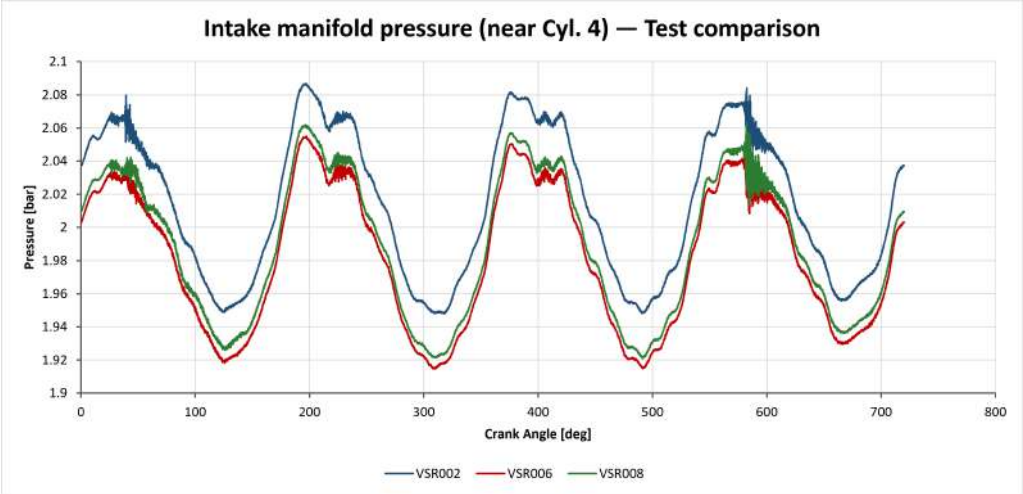


Figure 6.21: Comparison of the intake manifold pressure traces on cylinder 4 for MP010.

The in-cylinder pressure traces presented in Figure 6.22 show an increase in peak pressure after removal of the check valve. VSR002 reaches the lowest maximum pressure, VSR006 produces a higher peak, and VSR008 presents a further small increase. In contrast, the crank angle of the pressure maximum remains very similar for the three configurations, close to 370 dCA and therefore approximately 10 dCA after combustion TDC.

The injected hydrogen masses at MP010 are 15.8 mg/cycle for VSR002, 15.4 mg/cycle for VSR006, and 15.5 mg/cycle for VSR008. Therefore, the higher cylinder pressure obtained after removing the check valve cannot be explained by a higher total hydrogen mass, since both modified configurations receive slightly less fuel than the baseline.

The result indicates that removing the check valve modifies the conditions under which the hydrogen is delivered and the mixture is prepared before combustion. The change in injection line pressure dynamics may alter the temporal distribution of the hydrogen entering the intake port and consequently the mixture formation and combustion development. Since VSR008 produces only a small additional increase relative to VSR006, the check valve appears to have a stronger influence on the resulting combustion than the additional nozzle restriction under this operating condition.

The higher peak cylinder pressure may indicate a stronger combustion event, but it should not automatically be interpreted as an improvement in engine performance.

No clear indication of pre-ignition is observed in the in-cylinder pressure traces.

Similarly, no pronounced high frequency pressure oscillations are visible around the combustion pressure maximum that would allow knock to be identified from the presented traces.

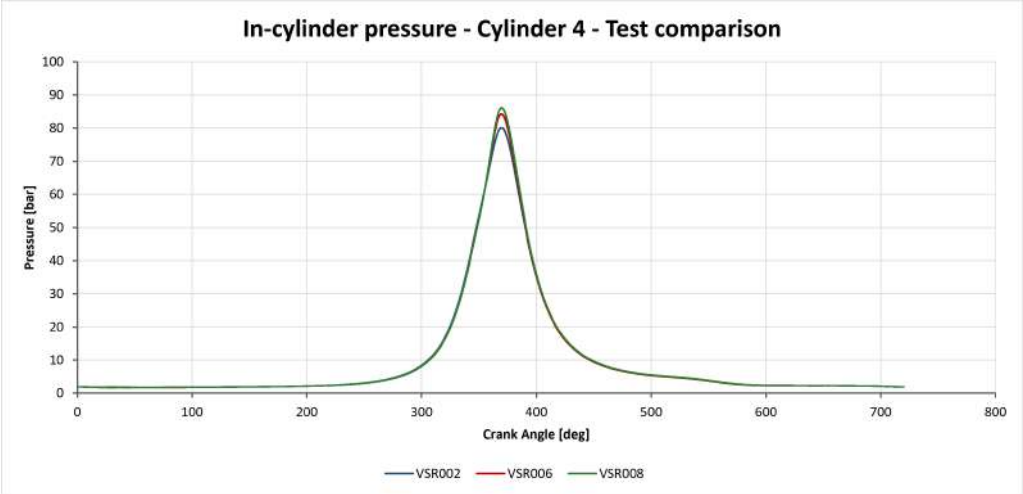


Figure 6.22: Comparison of the in-cylinder pressure traces on cylinder 4 for MP010.

The exhaust manifold pressure presented in Figure 6.23 contains the successive exhaust events of all four cylinders because the sensor is installed in the common exhaust manifold close to cylinder 4.

For cylinder 4, combustion TDC occurs at approximately 360 dCA. The following expansion process is subsequently followed by the exhaust event, making the pressure pulse approximately between 550 and 620 dCA the region most directly associated with the cylinder 4 exhaust process.

In this region, VSR002, VSR006, and VSR008 remain relatively close, despite the differences observed in peak in-cylinder pressure. This shows that the increased combustion pressure in VSR006 and VSR008 does not produce a proportional increase in the pressure measured in the common exhaust manifold.

The exhaust pressure is influenced by the cylinder pressure at exhaust valve opening, the subsequent gas expansion and blowdown process, and the interaction of pressure waves from all four cylinders. Differences in peak combustion pressure can therefore be substantially reduced before appearing in the common exhaust manifold. From the exhaust system perspective, the removal of the check valve and nozzle does not produce a major change in the pressure dynamics at MP010.

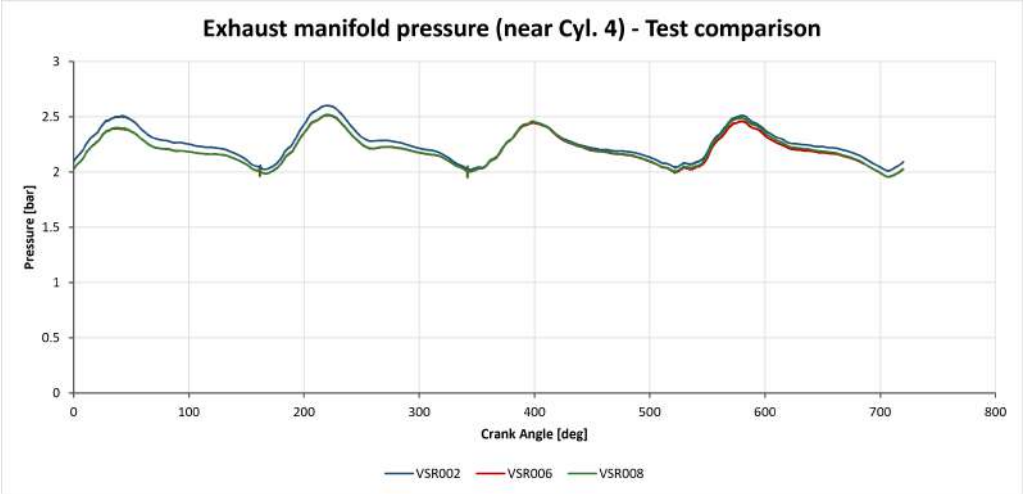


Figure 6.23: Comparison of the exhaust manifold pressure traces on cylinder 4 for MP010.

Overall, the comparison shows that the check valve plays an important role in isolating the cylinder 4 hydrogen line from the pressure dynamics of the intake system. In the baseline configuration, the injection line pressure becomes comparatively stable after the fuel delivery event. When the check valve is removed in VSR006, periodic intake-related pressure fluctuations remain visible in the injection line throughout the engine cycle. A very similar response is obtained in VSR008, indicating that the loss of pressure isolation is mainly associated with the removal of the check valve, while the additional removal of the nozzle has a smaller influence.

The modified configurations also produce higher peak in-cylinder pressures than the baseline, despite slightly lower injected hydrogen masses. The observed combustion change can therefore not be attributed to fuel quantity alone and is more consistent with changes in the delivery conditions and mixture formation resulting from the altered fuel line dynamics. Although the higher peak pressure indicates a stronger combustion response in cylinder 4, this should not be interpreted automatically as an improvement, since it may also increase cylinder-to-cylinder imbalance and local mechanical and thermal loading. From a fuel system perspective, the baseline configuration is therefore preferable because it provides greater separation between intake pressure disturbances and the hydrogen delivery line, supporting more controlled and repeatable fuel delivery.

The individual cylinder IMEP further confirms that the hardware modifications affected the contribution of cylinder 4. In both modified configurations, cylinder 4 presents a higher IMEP than the remaining unmodified cylinders. This is consistent with the higher in-cylinder pressure observed for VSR006 and VSR008 and indicates an increase in the indicated work produced by cylinder 4. However, this increase should not be interpreted independently as an overall improvement, since the modification also increases the imbalance between cylinders and removes the pressure isolation provided by the check valve.

The additional low and medium load comparisons presented in Appendix E confirm that these trends are maintained across the investigated operating range. At MP001, MP005, and MP010, removal of the check valve results in periodic intake related pressure fluctuations in the cylinder 4

injection line, whereas the baseline configuration remains substantially more stable after the fuel delivery event. The influence on the common intake manifold becomes more evident with increasing load: the three configurations are nearly coincident at MP001, while VSR006 and VSR008 operate at progressively lower intake pressure levels at MP005 and MP010.

A similar consistency is observed in the in-cylinder pressure response, where VSR006 and VSR008 produce higher peak pressures than VSR002 at the three selected operating points without a substantial change in the crank-angle position of the pressure maximum. The additional removal of the nozzle generally introduces only a limited further change. These results reinforce the conclusion that the check valve has the dominant influence on the pressure coupling between the hydrogen line and the intake system, while the nozzle has a secondary effect under the investigated conditions.

6.7 Injection Timing Comparison: VSR002 and VSR009

The effect of injection timing is evaluated by comparing VSR002 and VSR009 at MP010 (1800 rpm and 9 bar IMEP). Both campaigns use the same fuel delivery hardware, while the start of injection is shifted from SOI $= -340$ dCA in VSR002 to SOI $= -300$ dCA in VSR009. VSR009 therefore represents a 40 dCA later injection event.

The comparison includes the distributor upstream pressure, the cylinder 4 injection line pressure, the intake manifold pressure measured near cylinder 4, the in-cylinder pressure, and the exhaust manifold pressure measured near cylinder 4, presented in Figures 6.24 to 6.28. As in the previous comparisons, the intake and exhaust pressure signals contain contributions from all four cylinders because the corresponding sensors are installed in the common manifolds.

6.7.1 High Load: MP010

The distributor upstream pressure shown in Figure 6.24 retains a periodic behaviour for both injection timings. However, the pressure structures in VSR009 are shifted to later crank angles relative to VSR002. This displacement is consistent with the 40 dCA delay introduced in the start of injection.

The pressure upstream of the distributor responds to the sequential fuel demand of the four cylinders. Delaying the injection events therefore shifts the corresponding pressure disturbances within the 720 dCA cycle. VSR009 also presents a generally lower pressure level over part of the cycle, although the overall amplitude and periodic character of the signal remain similar.

The phase displacement is the main consequence observed at this measurement location and confirms that the change in injection timing propagates through the pressure dynamics of the common fuel supply. The small difference in pressure level may also be associated with the slightly lower hydrogen quantity used in VSR009, although the available pressure measurement alone does not allow this contribution to be quantified.

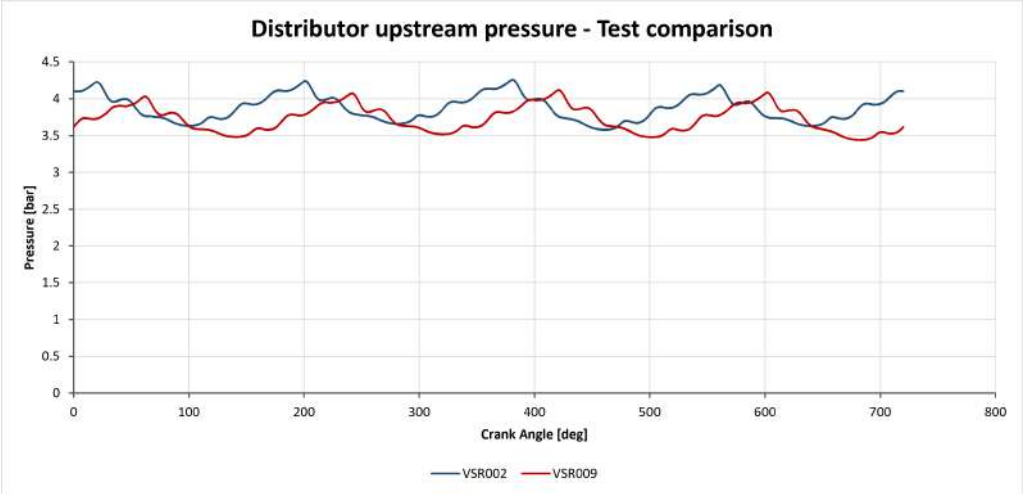


Figure 6.24: Comparison of the distributor upstream pressure traces for MP010.

The injection line pressure in Figure 6.25 provides the clearest confirmation of the imposed injection timing change. The pressure rise associated with fuel delivery occurs approximately 40 dCA later in VSR009 than in VSR002, in agreement with the change from SOI $= -340$ dCA to SOI $= -300$ dCA.

The overall shape of the fuel delivery event remains similar. VSR002 reaches a peak line pressure of approximately 2.8 bar, while VSR009 reaches a slightly lower maximum. The elevated pressure interval is also displaced towards later crank angles in VSR009 before the line pressure returns towards its residual level.

This result shows that the injection timing modification changes mainly the temporal position of the fuel delivery event rather than producing a fundamental change in its overall pressure response. A later injection event can reduce the residence time of hydrogen in the intake system, which may be favourable in terms of limiting the amount of combustible mixture present upstream of the cylinder. However, the shorter time available for mixture preparation may also reduce mixture homogeneity before ignition. The present pressure traces do not allow these two effects to be separated directly.

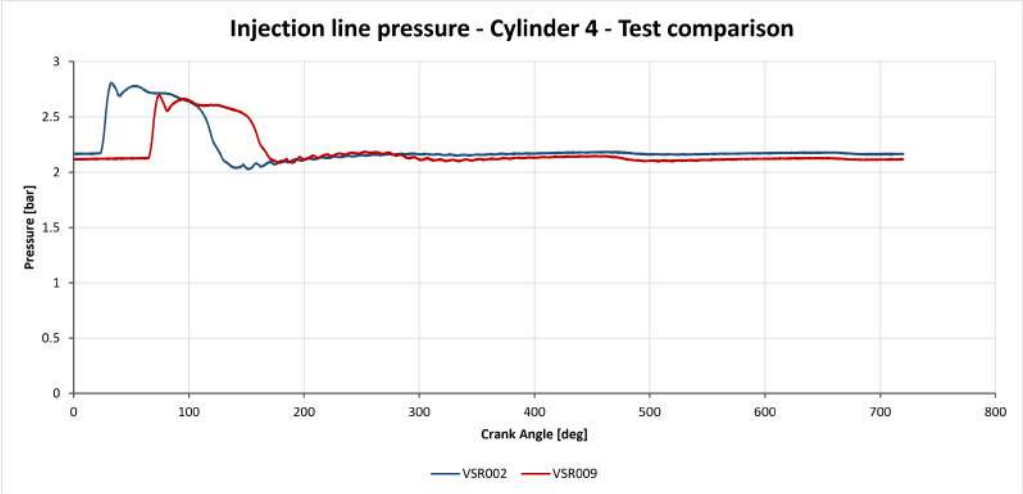


Figure 6.25: Comparison of the injection line pressure traces on cylinder 4 for MP010.

The intake manifold pressure presented in Figure 6.26 retains a similar periodic waveform for both campaigns, with the main pressure structures repeating approximately every 180 dCA as a consequence of the successive intake events of the four cylinders.

A clear difference is observed in the absolute pressure level. VSR009 operates at a consistently lower intake manifold pressure than VSR002 throughout most of the engine cycle. Since the sensor is located in the common intake manifold, this difference represents a change in the overall air path operating condition.

The lower intake pressure implies a lower pressure available for cylinder filling and may consequently affect the admitted air mass and the resulting air-fuel ratio. However, the manifold pressure alone is not sufficient to determine the corresponding change in cylinder air charge.

Short pressure disturbances remain visible around some of the intake manifold events. However, similar structures are present in VSR002 and VSR009 and repeat during successive cylinder events. The later injection timing therefore does not produce an evident increase in the magnitude of these pressure disturbances.

The available manifold pressure signal does not provide sufficient evidence to identify an intake backfire event. Nevertheless, delaying the injection reduces the time during which hydrogen is present in the intake path before combustion, which can be favourable from the point of view of reducing exposure of the premixed charge to an unintended ignition source.

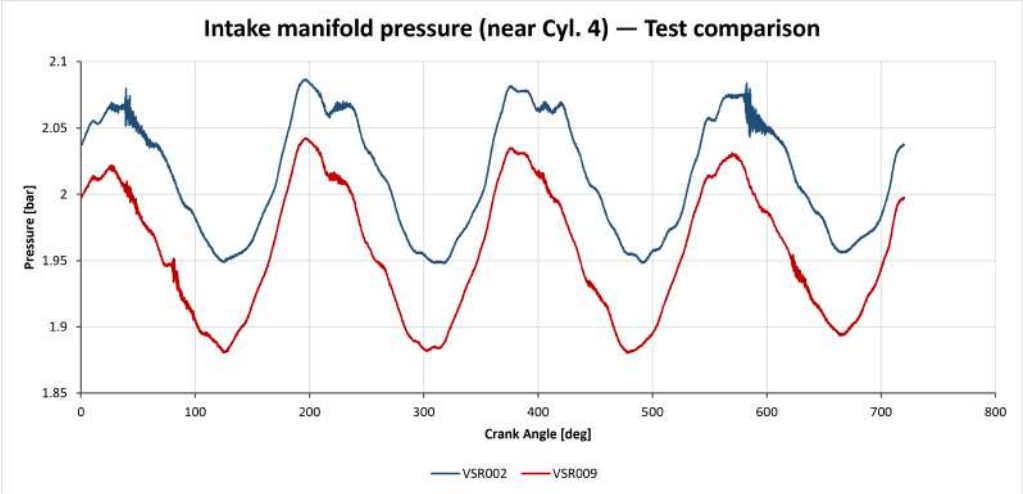


Figure 6.26: Comparison of the intake manifold pressure traces on cylinder 4 for MP010.

The in-cylinder pressure traces presented in Figure 6.27 remain very similar for the two injection timings. VSR002 reaches a maximum pressure of approximately 80 bar, while VSR009 presents a slightly lower peak of approximately 77 bar. In both cases, the maximum occurs close to 370 dCA, corresponding to approximately 10 dCA after combustion TDC.

The similarity in the location of the pressure maximum is significant. Although the fuel delivery event is delayed by 40 dCA in VSR009, the main combustion pressure peak remains almost unchanged in crank angle. The change in injection timing therefore affects the preparation of the mixture before ignition rather than producing an equivalent shift in the combustion phasing.

The injected hydrogen mass decreases from 15.8 mg/cycle in VSR002 to 15.4 mg/cycle in VSR009. The slightly lower peak pressure in VSR009 is therefore consistent with a small reduction in fuel energy supplied to the cylinder, although changes in mixture formation resulting from the later injection may also contribute to the observed difference.

From an engine operation perspective, the slightly lower peak pressure in VSR009 reduces the maximum mechanical and thermal loading experienced during combustion. This can be favourable if the same useful work is maintained. Conversely, if the lower pressure is accompanied by a reduction in cylinder IMEP, it would indicate a lower work contribution from the cylinder and would therefore be undesirable.

Peak pressure alone is consequently insufficient to determine whether the later injection timing improves engine performance. The corresponding cylinder IMEP or indicated work is required for this assessment.

No clear indication of pre-ignition is observed in either configuration.

No pronounced high frequency pressure oscillations are visible around the pressure maximum that would allow knock to be identified from these traces. The change in injection timing therefore does not show an obvious increase in abnormal combustion at MP010.

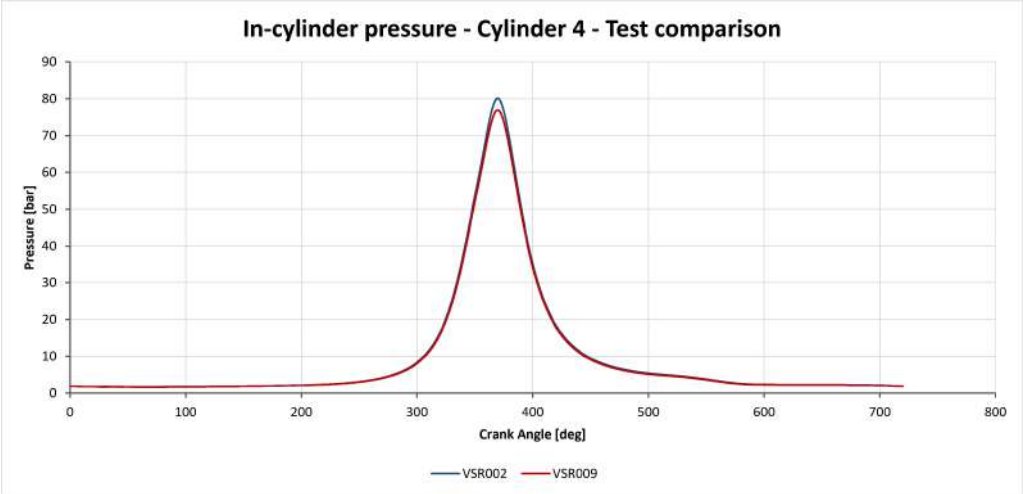


Figure 6.27: Comparison of the in-cylinder pressure traces on cylinder 4 for MP010.

The exhaust manifold pressure presented in Figure 6.28 maintains a similar periodic waveform for both injection timings, while VSR009 generally presents a lower pressure level throughout the engine cycle.

For cylinder 4, combustion TDC occurs at approximately 360 dCA and the subsequent expansion process is followed by the exhaust event. The pressure pulse approximately between 550 and 620 dCA is therefore the region most directly associated with the cylinder 4 exhaust process. VSR009 presents a slightly lower pressure contribution in this region, consistent with the lower peak in-cylinder pressure observed for the same campaign.

The lower exhaust manifold pressure may reduce the pressure against which the cylinder discharges during the exhaust process, which can be favourable in terms of pumping work. However, in a turbocharged engine, the exhaust flow also provides the energy required to drive the turbine. A reduction in exhaust pressure and available exhaust energy may therefore also contribute to a lower boost condition. This interpretation is consistent with the lower intake manifold pressure observed in VSR009, although exhaust temperature and turbocharger operating data would be required to quantify this relationship.

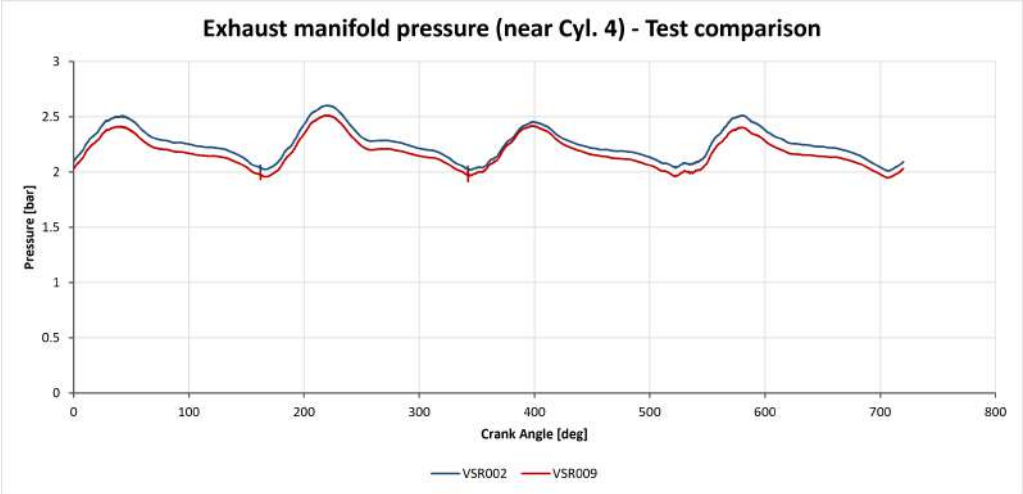


Figure 6.28: Comparison of the exhaust manifold pressure traces on cylinder 4 for MP010.

Overall, delaying the start of injection from SOI $= -340$ dCA to SOI $= -300$ dCA shifts the fuel delivery event by approximately 40 dCA. This displacement is clearly visible in both the injection line and distributor upstream pressure signals. Despite the later fuel delivery, the crank angle position of the maximum in-cylinder pressure remains nearly unchanged. The injection timing modification therefore affects mainly the period available for mixture preparation before ignition rather than producing a corresponding shift in the main combustion phasing.

At MP010, VSR009 operates with a slightly lower injected hydrogen mass and produces a modest reduction in peak in-cylinder pressure. The intake and exhaust manifold pressures are also lower, while their characteristic periodic behaviour remains similar to the baseline. The later injection therefore modifies both the fuel delivery conditions and the overall air path operating condition. From a combustion perspective, the shorter interval between fuel delivery and ignition reduces the time available for hydrogen-air mixing. This may affect mixture homogeneity, while the shorter residence time of hydrogen in the intake system may also reduce the exposure of the premixed charge to unintended ignition sources. Whether this represents an overall improvement cannot be determined from peak pressure alone and must also consider cylinder work, efficiency, mixture strength, and combustion stability.

The additional low and medium load comparisons presented in Appendix E show that the same behaviour is maintained across the investigated operating range. At MP001, MP005, and MP010, the later start of injection produces the expected displacement of the fuel delivery pressure transient, while the crank-angle position of the maximum in-cylinder pressure remains almost unchanged. VSR009 also presents a consistently lower intake manifold pressure at the three selected operating points, together with generally lower exhaust manifold and peak in-cylinder pressures. The consistency of these trends at the selected low, medium, and high load operating points supports the conclusion that the effect of injection timing extends beyond the local injection line and influences the mixture preparation and overall engine operating condition without substantially changing the phasing of the main cylinder pressure peak.

Chapter 7

Conclusions and Future Work

This chapter summarizes the main findings of the work and evaluates them in relation to the objectives defined at the beginning of the dissertation. The main conclusions obtained from the geometric characterization, experimental flow characterization, and engine testing are first presented. Based on these results, recommendations for future work are then proposed to support the further development and analysis of the hydrogen fuel injection system.

7.1 Conclusions

This dissertation investigated the hydrogen fuel delivery system developed for the converted DEUTZ TCD 3.6 L4 engine. The work focused on three main objectives: the geometric characterization of the rotary distributor, the experimental determination of the effective flow characteristics of the main metering and distribution components, and the evaluation of the influence of selected fuel system configurations during engine operation.

The geometric characterization of distributor 160 A established the relationship between its angular position and the overlap between the rotor and stator openings. The developed partial annular sector model provides a maximum ideal geometric overlap area of 72.10 mm^2 and defines the opening and closing profile of the distributor. Together with the distributor kinematics, this formulation provides a direct relationship between toothed wheel position and geometric opening area and was used as a reference during the experimental characterization.

An important conclusion obtained from the flow characterization is that the geometric overlap area and the effective flow area represent different quantities and should not be used interchangeably. The geometric model describes the physical opening created by the relative position of the distributor components, whereas the experimentally determined effective area represents the actual flow capacity of the component, including the influence of the real internal flow path and associated losses.

This difference is clearly observed for distributor 160 A. While the ideal geometric model produces a triangular opening profile with a maximum area of 72.10 mm^2, the experimentally determined effective area presents a rapid opening followed by a broad region of high flow capacity.

After correction for the residual flow measured in the closed position, the maximum effective area was 22.240 mm^2. The distributor also operated under both choked and non choked conditions during its angular sweep. These results provide the experimental relationship between distributor position and actual flow capacity required for a representative description of the component.

The proportional valve 620 B showed a different and considerably simpler flow characteristic. After an initial opening threshold of approximately 8% commanded position, the effective area increased almost linearly with valve command. The active range presented a coefficient of determination of $R^2 = 0.99993$, and extrapolation to full opening resulted in an effective area of 3.513 mm^2. Comparison with the geometric reference area resulted in a discharge coefficient of $C_d = 0.716$. The measured hysteresis was small, with a maximum absolute relative difference of approximately 1.10%. The proportional valve can therefore be represented primarily by its initial opening offset followed by an approximately linear effective area characteristic.

The engine tests demonstrated that the behaviour of the complete fuel delivery system depends not only on the total hydrogen quantity supplied to the engine but also on the transient behaviour of the components between the distributor and the intake ports. The investigated modifications included connection hose length and diameter, check valve and nozzle configuration, and start of injection. These parameters were shown to influence the pressure dynamics of the fuel system and, in some cases, the resulting in-cylinder pressure response.

The hose comparison showed that increasing the connection hose length modified the injection line pressure dynamics but had a relatively limited effect on the resulting cylinder response. In contrast, reducing the hose diameter produced a considerably stronger effect, including larger pressure variations in the injection line and a reduction in peak in-cylinder pressure despite only a small change in the injected hydrogen mass. The results therefore show that the transient fuel delivery behaviour can be significantly affected by the geometry of the connection line and that hose diameter is particularly important for the investigated system.

The check valve comparison showed that this component has an important pressure isolation function. With the check valve installed, the injection line becomes comparatively stable after the fuel delivery event. Its removal allows intake pressure disturbances to propagate more strongly into the hydrogen line. The additional removal of the nozzle produced a smaller further change, indicating that the check valve has the dominant influence on this pressure coupling. The baseline configuration is therefore preferable from the perspective of controlled and repeatable fuel delivery.

The injection timing comparison showed that delaying the start of injection by 40 dCA produced the corresponding displacement of the fuel delivery pressure transient. During the engine tests, spark timing was calibrated so that CA50 remained within the combustion phasing region associated with favourable efficiency. Consequently, the similar combustion phasing observed between the injection timing configurations should be interpreted in the context of this spark timing calibration. The results show that start of injection modifies the available mixture preparation time and the pressure conditions of the fuel delivery and air path systems even when favourable CA50 is maintained.

The baseline engine measurements also showed that the engine operated lean throughout the investigated map. Increasing load required a higher hydrogen mass and reduced lambda, while fuel consumption decreased and thermal efficiency increased. The highest efficiency was obtained in the higher load region, particularly in 1500 rpm. NO_x emissions remained low over most of the operating map, although isolated increases were measured at some of the lower lambda operating points.

No clear evidence of pre-ignition or intake backfire was identified from the pressure traces considered in this work, and no pronounced high frequency cylinder pressure oscillations were observed that would allow knock to be clearly identified. However, the available signals do not exclude the occurrence of isolated abnormal combustion events and should not be interpreted as proof of their complete absence.

Overall, the results demonstrate that the investigated hydrogen delivery system must be considered as a coupled system. The proportional valve defines the primary fuel metering characteristic, the rotary distributor controls the sequential distribution of the fuel, and the downstream components influence the transient pressure conditions under which the hydrogen reaches the intake ports. The experimental results also demonstrate why geometric flow areas alone are insufficient for describing the real system behaviour.

The objectives of the dissertation were therefore achieved by establishing a geometric description of the rotary distributor, experimentally determining the effective flow characteristics of the main fuel metering and distribution components, and identifying the influence of relevant hardware and injection parameters during engine operation. The resulting geometric, flow bench, and engine datasets provide a consistent experimental reference for the continued development of the fuel delivery system.

7.2 Future Work

The results obtained in this dissertation provide a basis for the continued development of the hydrogen fuel delivery system. One of the main future steps is the development of a one dimensional GT-Power model of the complete fuel delivery system. The geometric characterization of distributor 160 A can be used to define its kinematics and opening sequence, while the experimentally determined effective flow areas of the distributor and proportional valve 620 B provide the reference data required for model calibration.

The component models should first be validated against the experimental measurements and then extended to include the connection hoses, check valves, nozzles, and associated volumes. The pressure measurements obtained during the engine tests provide suitable validation data for the transient behaviour of the complete fuel delivery system. After this validation, the subsystem can be integrated into a complete engine GT-Power model to investigate its interaction with the intake, cylinders, exhaust system, and turbocharger.

The engine tests also showed that the connection hose diameter has a significant influence on the fuel delivery dynamics. Reducing the inner diameter produced a considerably stronger

effect than increasing the hose length. Future tests should therefore include a hose with an inner diameter larger than the standard configuration to determine whether a further reduction in flow restriction improves the pressure response and fuel delivery behaviour. This effect should be verified experimentally, since changing the diameter also changes the internal volume and pressure wave propagation in the line.

Finally, the experimental programme could be extended to syngas operation. Its different physical properties and required volumetric flow may change the influence of the restrictions identified during hydrogen operation and would provide an additional validation case for the future numerical model.

Overall, the geometric characterization, flow bench measurements, and engine test results obtained in this work provide the experimental basis required for future modelling, validation, and further optimization of the gaseous fuel delivery system.

References

[1] John B. Heywood. *Internal Combustion Engine Fundamentals*. 2nd. McGraw-Hill Education, 2018. ISBN: 9781260116106.

[2] S. Verhelst and T. Wallner. "Hydrogen-fueled internal combustion engines". In: *Progress in Energy and Combustion Science* 35.6 (2009), pp. 490–527. DOI: 10.1016/j.pecs.2009.08.001.

[3] Karsten Wittek, Vitor Cogo, and Geovane Prante. "Full load optimization of a hydrogen fuelled industrial engine". In: *International Journal of Hydrogen Energy* 77 (2024), pp. 230–243. DOI: 10.1016/j.ijhydene.2024.06.198.

[4] Hilmi Ersin Oktar, Muammer Özkan, and Mersin Hürpekli. "Experimental and thermodynamic analysis of hydrogen and gasoline in a spark-ignition engine". In: *International Journal of Hydrogen Energy* 203 (2026), p. 153154. DOI: 10.1016/j.ijhydene.2026.153154.

[5] M. F. J. Brunt and A. L. Emtage. "Evaluation of IMEP routines and analysis errors". In: *SAE Technical Paper* 1996-0609 (1996). DOI: 10.4271/960609.

[6] Jerald A. Caton. "Maximum efficiencies for internal combustion engines: Thermodynamic limitations". In: *International Journal of Engine Research* 19.10 (2018), pp. 1005–1023.

[7] N. Watson and M. S. Janota. *Turbocharging the Internal Combustion Engine*. Red Globe Press, 1982.

[8] Reza Shahouni and Moslem Abrofarakh. "Semi-Empirical Zero-Dimensional Optimization Model for Minimizing NOx Emissions and Maximizing Thermal Efficiency in Hydrogen Internal Combustion Engines". In: *Fuel* 420 (2026), p. 138939. DOI: 10.1016/j.fuel.2026.138939.

[9] Fabián Musy et al. "Hydrogen-fuelled internal combustion engines: Direct Injection versus Port-Fuel Injection". In: *International Journal of Hydrogen Energy* 137 (2025), pp. 925–938. DOI: 10.1016/j.ijhydene.2024.07.195.

[10] European Commission. *REPowerEU: affordable, secure and sustainable energy for Europe*. https://commission.europa.eu/topics/energy/repowereu_en. Accessed: 2026-07-08.

[11] European Commission. *Neue Abgasnorm Euro 7 – die Fakten*. https://germany.representation.ec.europa.eu/neue-abgasnorm-euro-7-die-fakten_de. Accessed: 2026-07-08.

[12] Mohamed A. Habib et al. "Hydrogen combustion, production, and applications: A review". In: *Alexandria Engineering Journal* 100 (2024), pp. 182–207. DOI: 10.1016/j.aej.2024.05.030.

[13] Amin Paykani et al. “Synthesis gas as a fuel for internal combustion engines in transportation”. In: *Progress in Energy and Combustion Science* 90 (2022), p. 100995. DOI: 10.1016/j.pecs.2022.100995.

[14] BMW Group. *BMW iX5 Hydrogen: Details zum Wasserstofftank*. Accessed: 2026-07-09. URL: https://www.bmwgroup.com/de/news/allgemein/2026/bmw-ix5-hydrogen-wasserstofftank.html.

[15] Helmut Klell, Helmut Eichlseder, and Alexander Trattner. *Wasserstoff in der Fahrzeugtechnik: Erzeugung, Speicherung, Anwendung*. 4th. Wiesbaden, Germany: Springer Vieweg, 2018. ISBN: 978-3-658-20446-4. DOI: 10.1007/978-3-658-20447-1.

[16] Karsten Wittek, Vitor Cogo, and Geovane Prante. “Development of a pneumatic actuated low-pressure direct injection gas injector for hydrogen-fueled internal combustion engines”. In: *International Journal of Hydrogen Energy* 48.19 (2023). Available online 27 December 2022, pp. 7111–7126. DOI: 10.1016/j.ijhydene.2022.12.023.

[17] Ahmad Hilmi Khalid et al. “Hydrogen port fuel injection: Review of fuel injection control strategies to mitigate backfire in internal combustion engine fuelled with hydrogen”. In: *International Journal of Hydrogen Energy* 66 (2024), pp. 571–581. DOI: 10.1016/j.ijhydene.2024.04.087.

[18] Zeyuan Huang et al. “Effects of hydrogen injection timing and injection pressure on mixture formation and combustion characteristics of a hydrogen direct injection engine”. In: *Fuel* 363 (2024), p. 130966. DOI: 10.1016/j.fuel.2024.130966.

[19] G. Maio et al. “Experimental and numerical investigation of a direct injection spark ignition hydrogen engine for heavy-duty applications”. In: *International Journal of Hydrogen Energy* 47.67 (2022), pp. 29069–29084. DOI: 10.1016/j.ijhydene.2022.06.184.

[20] Kaustubh R. Kapadani et al. “Sustainable Optimization of Emissions and Performance in Hydrogen Port Fuel Injection Internal Combustion Engines”. In: *Energy Science & Engineering* (2026). DOI: 10.1002/ese3.70438.

[21] Jianbing Gao et al. “Review of the backfire occurrences and control strategies for port hydrogen injection internal combustion engines”. In: *Fuel* 307 (2022), p. 121553. DOI: 10.1016/j.fuel.2021.121553.

[22] Toyota Gazoo Racing. *Toyota Gazoo Racing demonstrates GR Yaris H2 at WRC stages*. https://toyotagazooracing.com/wrc/release/2025/0708_01/. Accessed: 2026-07-09.

[23] Toyota Times. *Liquid Hydrogen Challenge at the 24 Hours of Nürburgring*. https://toyotatimes.jp/en/spotlights/hpe_challenge_2026_001.html. Accessed: 2026-07-09.

[24] Toyota Europe. *Le Mans 24 Hours: GR H2 Racing Concept debut*. https://newsroom.toyota.eu/le-mans-24-hours-tr-lh2-racing-prototype/. Accessed: 2026-07-09.

[25] MAN Energy Solutions. *Hydrogen Engines for Power Generation*. Accessed: 2026-07-09. URL: https://www.man.eu/engines/en/products/power-generation/wasserstoff/hydrogen.html.

[26] MAN Truck & Bus. *MAN hTGX: Ein Truck für besondere Fälle*. Accessed: 2026-07-09. URL: https://www.man.eu/de/de/ueber-uns/man-erleben/truckers-world/stories/ein-truck-fuer-besondere-faelle-162368.html.

[27] JCB. *JCB Hydrogen Engine Technology*. Accessed: 2026-07-09. URL: https://www.jcb.com/en-US/explore/sustainability/hydrogen/.

[28] European Alternative Fuels Observatory. *Germany launches new funding scheme for hydrogen refuelling and trucks*. Accessed: 2026-07-09. URL: https://alternative-fuels-observatory.ec.europa.eu/general-information/news/germany-launches-new-funding-scheme-hydrogen-refuelling-and-trucks.

Appendix A

Technical Drawings and CAD Models

This appendix presents additional CAD models and technical drawings of the main components of the hydrogen fuel delivery system. These drawings complement the component descriptions provided in the main body of the dissertation by showing their geometry, internal arrangement, and main design features.

The proportional valve 620 B is presented in Figures A.1 and A.2, showing the external geometry and the internal arrangement of the component, respectively. The corresponding sectional technical drawing is provided in Figure A.3.

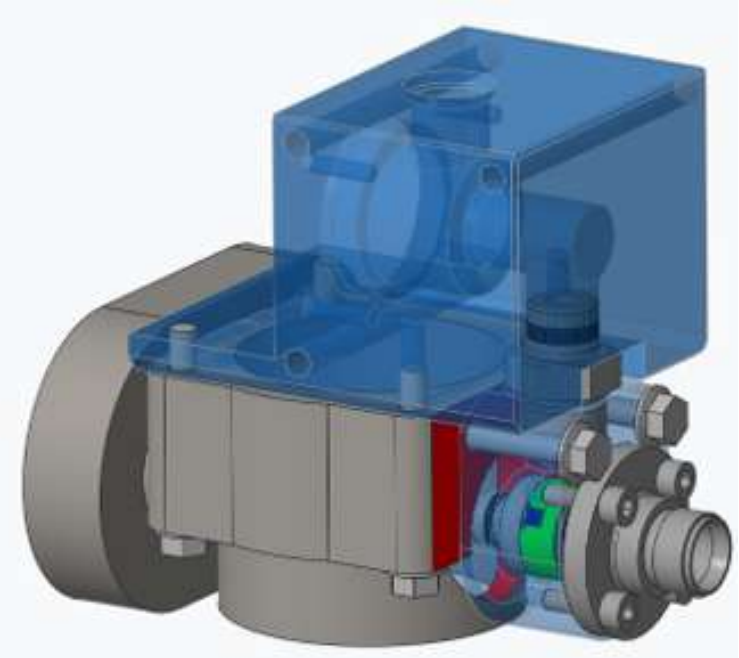


Figure A.1: Isometric CAD view of the proportional valve 620 B.

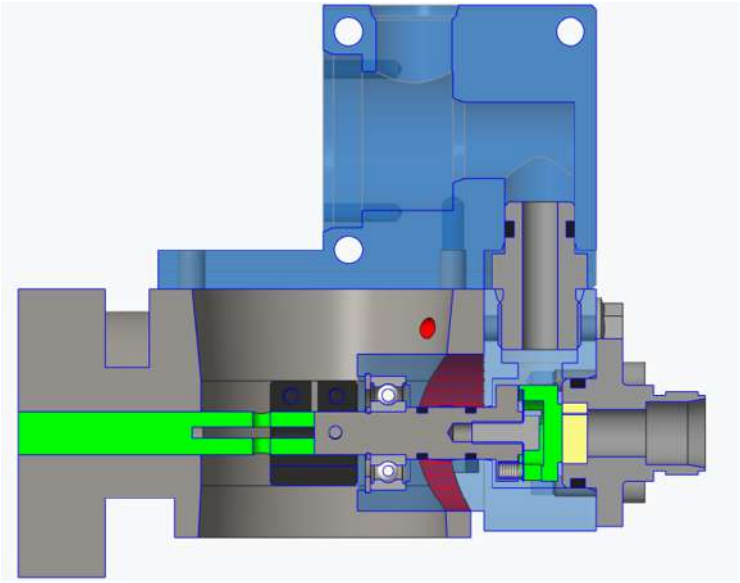


Figure A.2: Sectional CAD view of the proportional valve 620 B.

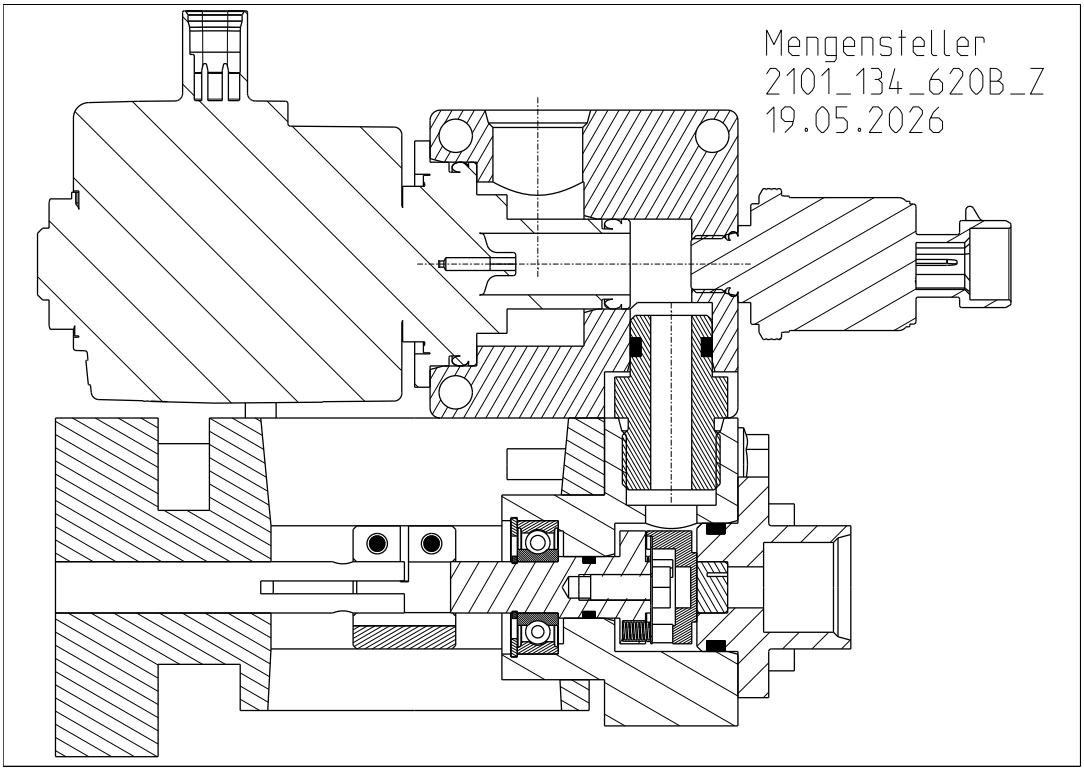


Figure A.3: Sectional technical drawing of the proportional valve 620 B.

The rotary distributor 160 A is presented in Figures A.4 and A.5. The sectional view illustrates the internal arrangement of the distributor, while the corresponding technical drawing is provided in Figure A.6.



Figure A.4: Isometric CAD view of the rotary distributor 160 A.

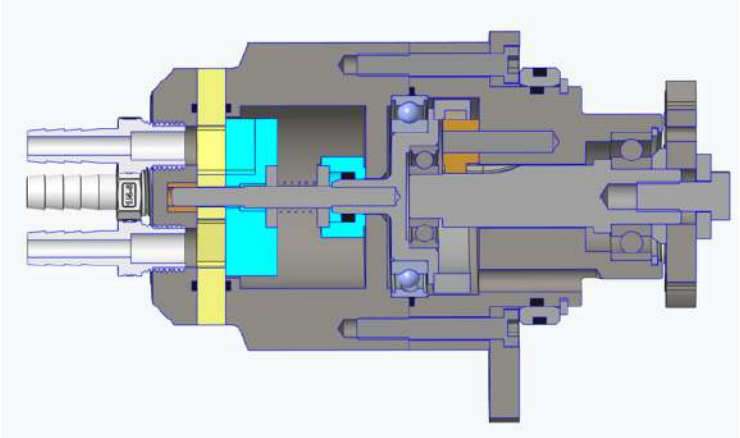


Figure A.5: Sectional CAD view of the rotary distributor 160 A.

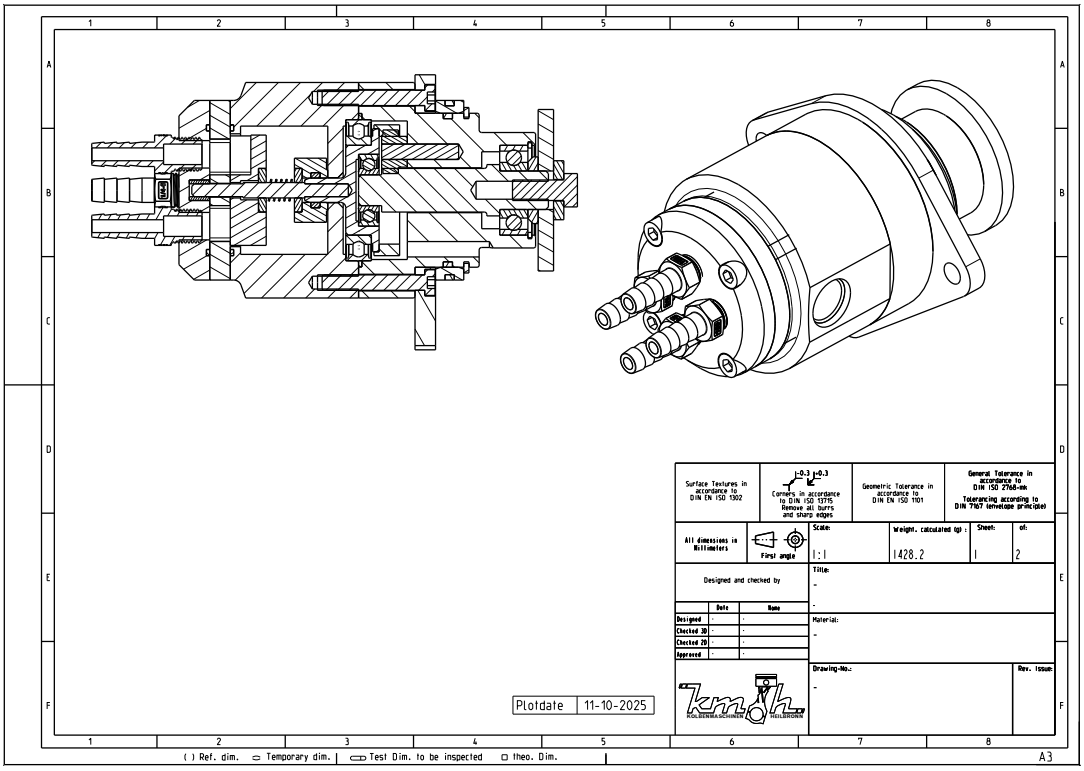


Figure A.6: Sectional technical drawing of the rotary distributor 160 A.

Additional technical drawings of the stator plate and the nozzle system are presented in Figures A.7 and A.8, respectively. These drawings provide the geometric definition of components directly involved in the distribution and delivery of hydrogen to the intake ports.

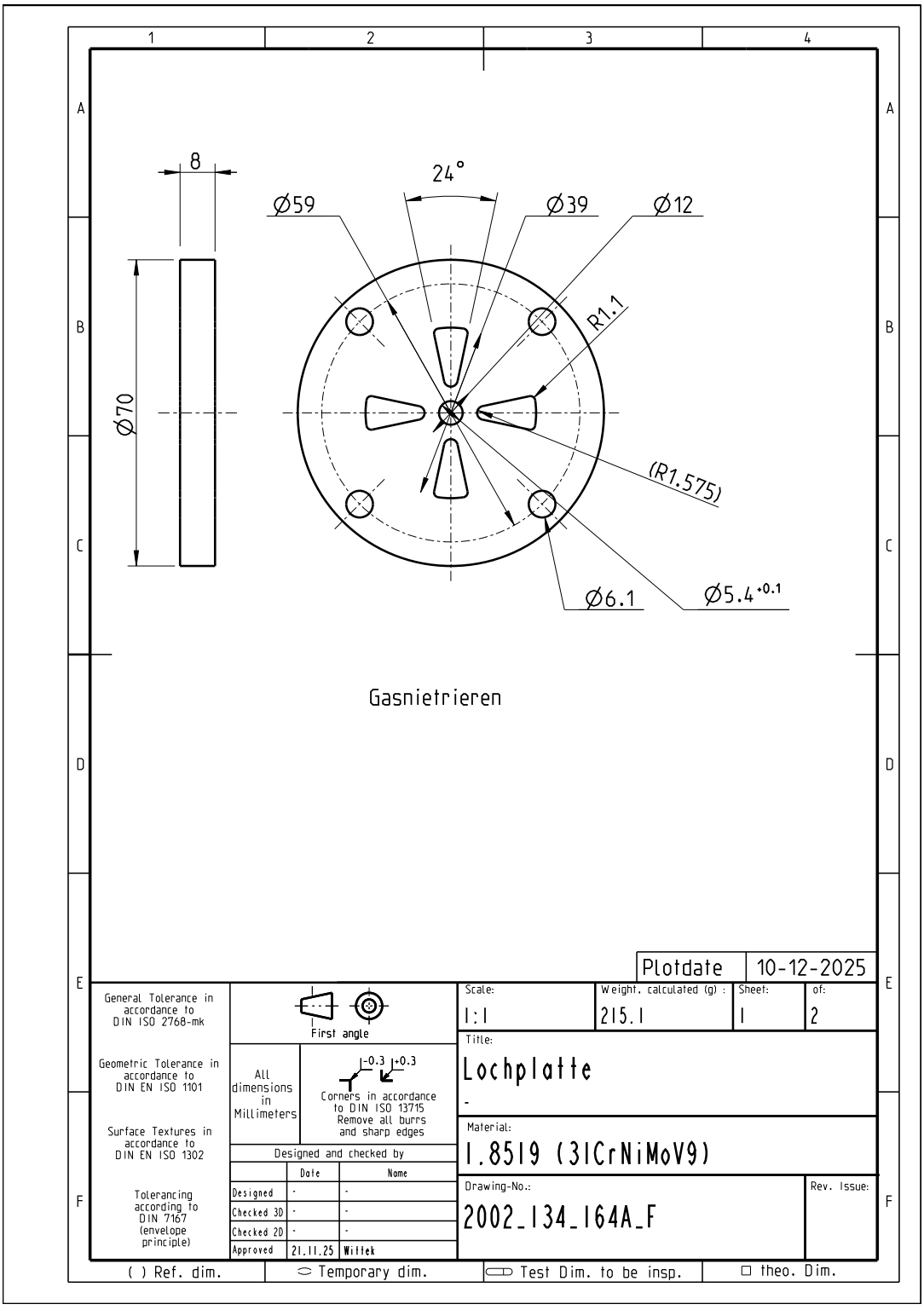


Figure A.7: Technical drawing of the stator plate.

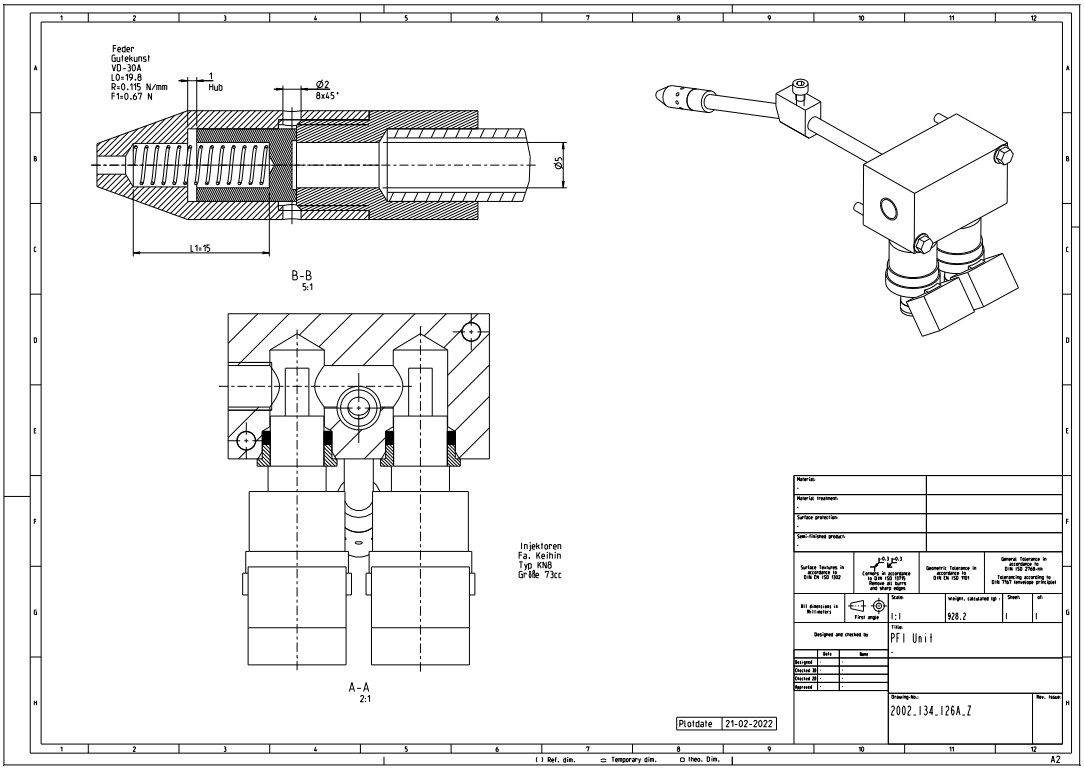


Figure A.8: Technical drawing of the nozzle system.

Appendix B

Rotary Distributor Overlap Area Calculation Tool

This appendix describes the spreadsheet calculation tool developed to characterize the geometric overlap area of the rotary distributor as a function of the toothed wheel angular position. The tool constitutes the primary geometric reference for all experimental and numerical work related to the distributor.

A.1 Geometric Model of the Partial Annular Sector

The rotor window and each of the four stator outlet windows can be represented geometrically as identical partial annular sectors defined by the inner radius r_1, outer radius r_2, and angular width α. These parameters were obtained directly from the CAD model. The area of a single sector is derived from integration in polar coordinates:

$$A_s = \frac{\alpha_{\text{rad}}}{2}\left(r_2^2 - r_1^2\right) \tag{B.1}$$

where $\alpha_{\text{rad}} = \alpha \cdot \pi/180$ is the sector angle in radians. This expression yields the maximum geometrically possible overlap area $A_{\max}$, attained when the rotor and stator windows are in perfect angular alignment ($\delta = 0$).

When the rotor is displaced by a relative angle δ with respect to the aligned position, the angular extent of the intersection between the two windows decreases linearly:

$$\Delta\alpha(\delta) = \max(0,\ \alpha - |\delta|) \tag{B.2}$$

The physical meaning of Equation B.2 is illustrated in Figure B.1: at $\delta = 0$ the overlap equals the full sector angle α; it decreases linearly with increasing displacement and reaches zero when $|\delta| = \alpha$, at which point the window is fully closed.

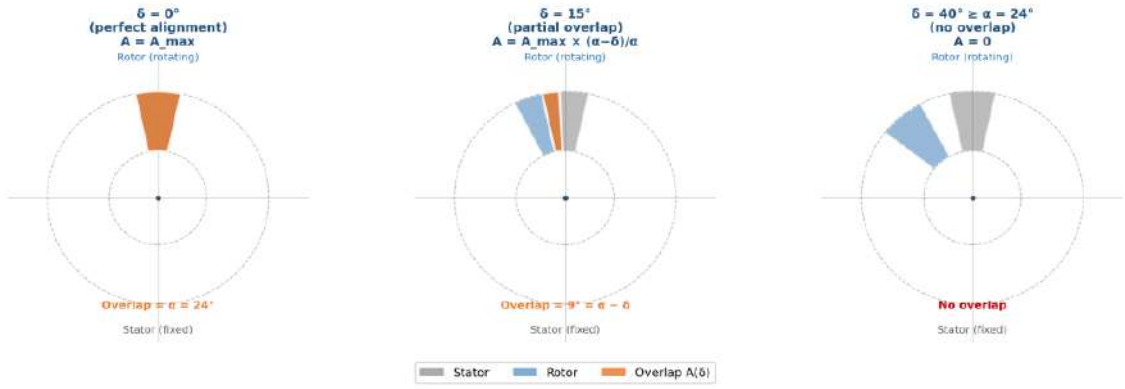


Figure B.1: Overlap area for three values of relative angular displacement δ. *Left:* perfect alignment ($\delta = 0°$, $A = A_{\max}$). *Centre:* partial overlap ($\delta = 15°$). *Right:* fully closed ($|\delta| \geq \alpha = 24°$, $A = 0$).

Since the area of an annular sector is directly proportional to its central angle (Equation B.1), the instantaneous overlap area is equally linear in δ:

$$A(\delta) = \frac{\max(0,\ \alpha_{\text{rad}} - |\delta_{\text{rad}}|)}{2} \left(r_2^2 - r_1^2\right) \tag{B.3}$$

This linear relationship is the direct and exact geometric consequence of the sector profile and produces the symmetric triangular injection area profile that characterizes this class of rotary distributors.

A.2 Kinematic Conversion to Toothed Wheel Angle

The distributor incorporates an internal 3:1 gear reduction between the externally accessible toothed wheel and the graphite rotor. Rotating the toothed wheel by an angle θ_w therefore produces a rotor displacement of:

$$\delta = \frac{\theta_w}{i} \tag{B.4}$$

where $i = 3$ is the internal gear ratio. Expressing angular position in terms of θ_w is operationally relevant because it corresponds directly to the physically accessible and measurable quantity during characterization testing on the flow bench and with the Coriolis mass meter: the toothed wheel can be rotated to a known angular position and the corresponding flow area read from the tool.

Substituting Equation B.4 into Equation B.3, the overlap area as a function of toothed wheel angle is:

$$A(\theta_w) = \frac{\max\left(0,\ \alpha_{\text{rad}} - \left|\frac{\theta_w}{i} - \alpha_{\text{rad}}\right|\right)}{2} \left(r_2^2 - r_1^2\right) \tag{B.5}$$

where the expression inside the absolute value represents the rotor displacement measured from the peak alignment position. The full injection window, the range of toothed wheel angles over which $A > 0$, spans:

$$\Delta\theta_{w,\mathrm{inj}} = 2\,\alpha \cdot i \tag{B.6}$$

For distributor 160 A ($\alpha = 24°$, $i = 3$), this yields an injection window of $\Delta\theta_w = 144°$ of toothed wheel rotation, centred on the peak alignment position.

A.3 Spreadsheet Implementation

The calculation tool was implemented in an Excel workbook. Figure B.2 shows the geometry sheet of the calculation tool, which contains the input parameters r_1, r_2, α, and i. The derived quantities are calculated automatically from these parameters through linked cell references.

DISTRIBUTOR GEOMETRY & PARAMETERS

All calculated values update automatically (edit blue cells)

IDENTIFICATION

Parameter	Value	Unit	Notes
Distributor model reference	160 A	-	Model name / serial number
Number of sectors N	4	-	One sector per cylinder

SECTOR GEOMETRY

Parameter	Value	Unit	Notes
Inner radius r_1	6.0	mm	Radial distance centre to inner arc
Outer radius r_2	19.5	mm	Radial distance centre to outer arc
Sector angular width α	24.0	°	Angle between the two radial faces

KINEMATICS

Parameter	Value	Unit	Notes
Internal gear ratio (toothed wheel : rotor)	3.0	-	Rotating wheel 3° turns rotor 1°

CALCULATED GEOMETRY (automatic)

Parameter	Value	Unit	Formula
α in radians	0.4189	rad	α × π/180
A_max = (α_rad/2)×(r_2^2−r_1^2)	72.10	mm²	Max overlap area
Equivalent diameter D_ref	9.58	mm	√(4·A_max/π)
Half-window (wheel degrees)	72.0	°	α × gear_ratio
Full injection window	144.0	°	2 × half-window
Period between sectors (wheel)	270.0	°	360 × ratio / N

LOOKUP A — wheel angle → overlap area

Toothed wheel angle (measured from start of opening, 0 = window just closed)

θ_wheel from opening [°]	θ_rotor from opening [°]	Overlap area A [mm²]	A / A_max [—]
72.0	24.0	72.10	1.000

LOOKUP B — desired overlap angle → wheel degrees to rotate

Sector opening angle (rotor degrees, 0 to α)(How many wheel degrees to rotate from closed)

Desired overlap angle [°]	Wheel degrees to rotate [°]	Resulting area A [mm²]	A / A_max [—]
12.0	36.0	36.05	0.500

Figure B.2: Geometry sheet of the calculation tool.

Two interactive lookup functions are provided within the same sheet. The first accepts any toothed wheel angle θ_w as input and returns the corresponding rotor displacement, instantaneous overlap area $A(\theta_w)$, and normalised area $A/A_{\max}$. The second performs the inverse operation: given a desired rotor opening angle δ, it computes the required toothed wheel rotation from the closed position as:

$$\theta_w = \delta \cdot i$$

(B.7)

This inverse function was used directly during flow bench testing to determine the toothed wheel positions corresponding to the target angular steps of the measurement sweep.

Table B.1 summarises the geometric and kinematic input parameters of distributor 160 A together with the key derived quantities can be used throughout the experimental and numerical analysis.

Table B.1: Geometric parameters and derived quantities of the Distributor 160 A

Parameter	Symbol	Unit	Value
Inner radius	r_1	mm	6.0
Outer radius	r_2	mm	19.5
Sector angular width	α	deg	24.0
Internal gear ratio	i	–	3
Maximum overlap area	$A_{\max}$	mm^2	72.10
Injection window (wheel)	$\Delta\theta_{w,\text{inj}}$	deg	144
Peak position (wheel)	$\theta_{w,\text{peak}}$	deg	72

Table B.2 lists the calculated values of $A(\theta_w)$ at 1° intervals over the toothed wheel range, together with the corresponding rotor angle and normalized area. The resulting profile is a symmetric isosceles triangle, consistent with Equation B.5, spanning the window $[0^\circ, 144^\circ]$ of toothed wheel rotation with its peak at $\theta_w = \alpha \cdot i = 72^\circ$.

Table B.2: Calculated Overlap Area Values as a Function of Wheel Angle

θ_{wheel} [°]	θ_{disc} [°]	$A(\theta)$ [mm^2]	$A/A_{\max}$ [-]
0	0.0	0.00	0.000
1	0.3	1.00	0.014
2	0.7	2.00	0.028
3	1.0	3.00	0.042
4	1.3	4.01	0.056
5	1.7	5.01	0.069
6	2.0	6.01	0.083
7	2.3	7.01	0.097
8	2.7	8.01	0.111
9	3.0	9.01	0.125
10	3.3	10.01	0.139
11	3.7	11.02	0.153

θ_{wheel} [°]	θ_{disc} [°]	$A(\theta)$ [mm^2]	A/A_{max} [-]
12	4.0	12.02	0.167
13	4.3	13.02	0.181
14	4.7	14.02	0.194
15	5.0	15.02	0.208
16	5.3	16.02	0.222
17	5.7	17.02	0.236
18	6.0	18.02	0.250
19	6.3	19.03	0.264
20	6.7	20.03	0.278
21	7.0	21.03	0.292
22	7.3	22.03	0.306
23	7.7	23.03	0.319
24	8.0	24.03	0.333
25	8.3	25.03	0.347
26	8.7	26.04	0.361
27	9.0	27.04	0.375
28	9.3	28.04	0.389
29	9.7	29.04	0.403
30	10.0	30.04	0.417
31	10.3	31.04	0.431
32	10.7	32.04	0.444
33	11.0	33.05	0.458
34	11.3	34.05	0.472
35	11.7	35.05	0.486
36	12.0	36.05	0.500
37	12.3	37.05	0.514
38	12.7	38.05	0.528
39	13.0	39.05	0.542
40	13.3	40.06	0.556
41	13.7	41.06	0.569
42	14.0	42.06	0.583
43	14.3	43.06	0.597
44	14.7	44.06	0.611
45	15.0	45.06	0.625
46	15.3	46.06	0.639
47	15.7	47.06	0.653
48	16.0	48.07	0.667
49	16.3	49.07	0.681

θ_{wheel} [°]	θ_{disc} [°]	$A(\theta)$ [mm^2]	A/A_{max} [-]
50	16.7	50.07	0.694
51	17.0	51.07	0.708
52	17.3	52.07	0.722
53	17.7	53.07	0.736
54	18.0	54.07	0.750
55	18.3	55.08	0.764
56	18.7	56.08	0.778
57	19.0	57.08	0.792
58	19.3	58.08	0.806
59	19.7	59.08	0.819
60	20.0	60.08	0.833
61	20.3	61.08	0.847
62	20.7	62.09	0.861
63	21.0	63.09	0.875
64	21.3	64.09	0.889
65	21.7	65.09	0.903
66	22.0	66.09	0.917
67	22.3	67.09	0.931
68	22.7	68.09	0.944
69	23.0	69.10	0.958
70	23.3	70.10	0.972
71	23.7	71.10	0.986
72	24.0	72.10	1.000
73	24.3	71.10	0.986
74	24.7	70.10	0.972
75	25.0	69.10	0.958
76	25.3	68.09	0.944
77	25.7	67.09	0.931
78	26.0	66.09	0.917
79	26.3	65.09	0.903
80	26.7	64.09	0.889
81	27.0	63.09	0.875
82	27.3	62.09	0.861
83	27.7	61.08	0.847
84	28.0	60.08	0.833
85	28.3	59.08	0.819
86	28.7	58.08	0.806
87	29.0	57.08	0.792

θ_{wheel} [°]	θ_{disc} [°]	$A(\theta)$ [mm^2]	A/A_{max} [-]
88	29.3	56.08	0.778
89	29.7	55.08	0.764
90	30.0	54.07	0.750
91	30.3	53.07	0.736
92	30.7	52.07	0.722
93	31.0	51.07	0.708
94	31.3	50.07	0.694
95	31.7	49.07	0.681
96	32.0	48.07	0.667
97	32.3	47.06	0.653
98	32.7	46.06	0.639
99	33.0	45.06	0.625
100	33.3	44.06	0.611
101	33.7	43.06	0.597
102	34.0	42.06	0.583
103	34.3	41.06	0.569
104	34.7	40.06	0.556
105	35.0	39.05	0.542
106	35.3	38.05	0.528
107	35.7	37.05	0.514
108	36.0	36.05	0.500
109	36.3	35.05	0.486
110	36.7	34.05	0.472
111	37.0	33.05	0.458
112	37.3	32.04	0.444
113	37.7	31.04	0.431
114	38.0	30.04	0.417
115	38.3	29.04	0.403
116	38.7	28.04	0.389
117	39.0	27.04	0.375
118	39.3	26.04	0.361
119	39.7	25.03	0.347
120	40.0	24.03	0.333
121	40.3	23.03	0.319
122	40.7	22.03	0.306
123	41.0	21.03	0.292
124	41.3	20.03	0.278
125	41.7	19.03	0.264

θ_{wheel} [°]	θ_{disc} [°]	$A(\theta)$ [mm^2]	A/A_{max} [-]
126	42.0	18.02	0.250
127	42.3	17.02	0.236
128	42.7	16.02	0.222
129	43.0	15.02	0.208
130	43.3	14.02	0.194
131	43.7	13.02	0.181
132	44.0	12.02	0.167
133	44.3	11.02	0.153
134	44.7	10.01	0.139
135	45.0	9.01	0.125
136	45.3	8.01	0.111
137	45.7	7.01	0.097
138	46.0	6.01	0.083
139	46.3	5.01	0.069
140	46.7	4.01	0.056
141	47.0	3.00	0.042
142	47.3	2.00	0.028
143	47.7	1.00	0.014
144	48.0	0.00	0.000

Appendix C

Analytical Formulation for Effective Flow Area Characterization from Coriolis Measurements

This appendix describes the calculation procedure used to determine the effective flow area of the Mengesteller 620 B proportional valve and the Verteiler 160 A rotary distributor from experimental measurements performed with compressed air and a Coriolis mass flow meter.

The procedure implemented in the calculation spreadsheet includes the conversion of the measured quantities to the units required by the calculation, the determination of the upstream air density from the ideal gas law, the evaluation of the measured and critical pressure ratios, the calculation of the isentropic flow function, and the determination of the effective flow area. For the rotary distributor, the calculated effective area is additionally corrected by subtracting the effective area corresponding to the closed-position leakage.

The equations presented in the following sections reproduce the calculation procedure implemented in the spreadsheet. The proportional valve and rotary distributor use the same pressure-ratio and flow-function treatment, but different pressure terms are used in their respective effective-area equations. These component-specific expressions are therefore presented separately.

C.1 Measured Variables

The main quantities used as inputs to the calculations are:

- air mass flow rate, $\dot{m}$;
- upstream gauge pressure, pr_{up};
- downstream gauge pressure, pr_{dw};
- gas temperature, T_{gas};

- ambient pressure, p_{amb}.

The mass flow rate and upstream and downstream pressures are measured for the individual operating points. The ambient pressure and gas temperature are defined for each characterization dataset and are used throughout the corresponding calculations.

The independent variable depends on the component under evaluation. For the proportional valve, it is the relative valve position commanded by the TRIJEKT engine control unit. For the rotary distributor, it is the angular position of the distributor input shaft, θ_{dist}.

C.2 Pressure, Density, and Flow Function

The measured gauge pressures are first converted to absolute pressures by adding the ambient pressure:

$$p_{up} = pr_{up} + p_{amb}, \tag{C.1}$$

$$p_{dw} = pr_{dw} + p_{amb}, \tag{C.2}$$

where pr_{up} and pr_{dw} are the measured gauge pressures, p_{amb} is the ambient pressure, and p_{up} and p_{dw} are the corresponding absolute pressures. In the spreadsheet, these pressures are expressed in bar.

The upstream air density is calculated from the ideal gas law. Since p_{up} is stored in bar and T_{gas} in degrees Celsius, the spreadsheet implements the calculation as

$$\rho_{up} = \frac{p_{up} \times 10^5}{R_{gas}\,(273.15 + T_{gas})}, \tag{C.3}$$

where

$$R_{gas} = 287\ \mathrm{J\,kg^{-1}\,K^{-1}} \tag{C.4}$$

is the specific gas constant for air.

The measured downstream-to-upstream pressure ratio is then calculated as

$$PR_{meas} = \frac{p_{dw}}{p_{up}}. \tag{C.5}$$

The critical pressure ratio is calculated from

$$PR_{crit} = \left(\frac{2}{\gamma_{gas} + 1}\right)^{\frac{\gamma_{gas}}{\gamma_{gas} - 1}}, \tag{C.6}$$

where

$$\gamma_{gas} = 1.4. \tag{C.7}$$

For these conditions,

$$PR_{crit} \approx 0.52828. \tag{C.8}$$

The pressure ratio subsequently used in the flow calculation is selected according to

$$PR = \begin{cases} PR_{crit}, & PR_{meas} \leq PR_{crit}, \\ PR_{meas}, & PR_{meas} > PR_{crit}. \end{cases} \tag{C.9}$$

Therefore, when the measured pressure ratio is equal to or below the critical value, the calculation is performed using the critical pressure ratio, corresponding to choked flow. When the measured pressure ratio is above the critical value, the measured value is retained and the flow is treated as non-choked.

The same expression is used for the isentropic flow function in both cases:

$$\psi = \sqrt{\frac{\gamma_{gas}}{\gamma_{gas}-1}\left[PR^{\frac{2}{\gamma_{gas}}} - PR^{\frac{\gamma_{gas}+1}{\gamma_{gas}}}\right]}. \tag{C.10}$$

The distinction between choked and non-choked operation is therefore introduced through the value of PR used in Equation C.10, rather than through separate expressions for the effective flow area.

C.3 Effective Flow Area Calculation

The effective flow area is calculated from the measured mass flow rate, the upstream gas density, and the isentropic flow function. Although the same pressure-ratio treatment is applied to both components, the effective-area expressions implemented in the two spreadsheet worksheets are not identical and are therefore described separately.

C.3.1 Proportional Valve Effective Flow Area

For the proportional valve, the spreadsheet calculates the effective flow area using the absolute upstream pressure, p_{up}. Since the measured mass flow rate is expressed in kg/h, the pressure in bar, and the resulting area in mm^2, the implemented expression is

$$A_{eff} = \frac{\dot{m}/3600}{\psi\sqrt{2\,(p_{up}\times 10^5)\,\rho_{up}}} \times 10^6. \tag{C.11}$$

The factor $1/3600$ converts the measured mass flow rate from kg/h to kg/s, the factor 10^5 converts the pressure from bar to Pa, and the factor 10^6 converts the resulting area from m^2 to mm^2.

No leakage offset is applied to the proportional valve. The calculated A_{eff} is therefore used directly as the effective-area characteristic of the component.

C.3.2 Rotary Distributor Effective Flow Area

For the rotary distributor, the worksheet uses the ambient pressure, p_{amb}, in the pressure term of the effective-area equation. The expression implemented in the spreadsheet is

$$A_{eff} = \frac{\dot{m}/3600}{\psi\sqrt{2\,(p_{amb} \times 10^5)\,\rho_{up}}} \times 10^6. \tag{C.12}$$

This expression reproduces the distributor worksheet exactly. It should be noted that the pressure term differs from Equation C.11: the proportional-valve calculation uses p_{up}, whereas the distributor calculation uses p_{amb}.

A non-zero effective area is obtained at the calculated closed-position reference of the distributor. In the spreadsheet, the effective area of this reference point is

$$A_{eff,closed} = 1.3614 \text{ mm}^2. \tag{C.13}$$

This value is treated as a leakage offset and is subtracted from the calculated effective area at each angular position:

$$A_{eff,off} = A_{eff} - A_{eff,closed}. \tag{C.14}$$

The corrected quantity, $A_{eff,off}$, is therefore interpreted as the opening-related contribution to the distributor effective area. The constant subtraction used in Equation C.14 implies that the leakage contribution is assumed to remain constant over the angular sweep.

C.4 Proportional Valve Linearization

In addition to the direct calculation of A_{eff}, the proportional valve worksheet determines a linearized characteristic over the active operating range.

The geometric reference area used in the spreadsheet is

$$A_{geo} = 2.5 \times 2.5 \times 0.25\pi, \tag{C.15}$$

resulting in

$$A_{geo} = 4.9087 \text{ mm}^2. \tag{C.16}$$

A linear regression of A_{eff} as a function of TRIJEKT valve position is performed using the measurement points between 10.9% and 98.4% commanded position. If this regression is expressed as

$$A_{eff} = a\,u + b, \tag{C.17}$$

where u is the valve position in percent, the effective area corresponding to a 100% command is obtained in the spreadsheet from

$$A_{eff,100} = 100\,a + b. \tag{C.18}$$

The resulting value is

$$A_{eff,100} = 3.5125\ \text{mm}^2. \tag{C.19}$$

The discharge coefficient reported in the worksheet is subsequently calculated as

$$C_d = \frac{A_{eff,100}}{A_{geo}}, \tag{C.20}$$

which gives

$$C_d = 0.7156. \tag{C.21}$$

The worksheet also expresses each calculated effective area as a normalized effective-area value according to

$$A_{eff,lin} = \frac{A_{eff}}{A_{eff,100}} \times 1000, \tag{C.22}$$

where the resulting value is expressed in units of 0.1%, such that a value of 1000 corresponds to the extrapolated full-scale effective area.

The calculation tool additionally contains inverse lookup relations between this normalized effective area and the TRIJEKT command. Both a quadratic and a linear regression are evaluated over the active operating range. These relations are used to obtain the valve command corresponding to a required normalized effective area.

C.5 Valve Hysteresis Evaluation

A separate characterization sequence was performed to evaluate the hysteresis of the proportional valve. During this test, the commanded valve position was first increased and subsequently decreased over the tested active range. The effective flow area was calculated independently for the opening and closing measurements using Equation C.11.

For the command positions available in both directions, the spreadsheet compares the opening and closing effective areas using

$$A_{eff,diff} = \frac{A_{eff,opening} - A_{eff,closing}}{A_{eff,opening}} \times 100. \tag{C.23}$$

A positive value therefore indicates that the opening effective area is greater than the closing value at the same commanded position, whereas a negative value indicates that the closing effective area is greater.

No arithmetic mean of the opening and closing areas is used in the spreadsheet to define the main proportional-valve characteristic. The main effective-area characteristic and the hysteresis evaluation are obtained from separate characterization datasets. The hysteresis dataset is used specifically to quantify the difference between the opening and closing directions.

C.6 Proportional Valve Characterization

The proportional valve, Mengesteller 620 B, was characterized using compressed shop air. The main characterization dataset was obtained by commanding a series of discrete TRIJEKT valve positions and measuring the resulting air mass flow rate and upstream and downstream pressures. The ambient pressure and gas temperature used in this dataset are

$$p_{amb} = 0.99935 \text{ bar} \tag{C.24}$$

and

$$T_{gas} = 27\,^{\circ}\text{C}, \tag{C.25}$$

respectively.

For each calculated measurement point, the absolute pressures are obtained from Equations C.1 and C.2, the upstream air density is evaluated using Equation C.3, and the measured pressure ratio is determined from Equation C.5. The pressure ratio used in the flow function is then selected according to Equation C.9, and ψ is calculated using Equation C.10.

The proportional-valve effective area is subsequently determined from Equation C.11. The resulting values establish the relationship between the commanded TRIJEKT valve position and the effective flow area of the component.

The separate opening and closing dataset is processed using the same effective-area procedure, after which the relative hysteresis is calculated according to Equation C.23.

The corresponding measured and calculated quantities are presented in Figures C.1 and C.2.

Measurement made with compressed shop air																		
p_amb	0.999	[bar]											A,geo	4.9087	[mm²]	p,H2	12	[bar]
T_gas	27	[degC]											A,eff,DK100	3.5125	[mm²]	T,H2	20	[degC]
R_gas	287	[J/kgK]											Cd	0.716	[-]	eta,e	0.4	[-]
gamma_gas	1.4	[-]																
MP	TRIJEKT_pos	TRIJEKT_pos	TRIJEKT_pos	voltage_pos	mass_flow	pr_up	pr_dw	p_up	p_dw	PR_meas	PR	psi	rho_up	A_eff	Lin. A_eff	mp_H2	Pe	
[-]	[%]	[0.1%]	[V]	[V]	[kg/h]	[rel.bar]	[rel.bar]	[bar]	[bar]	[-]	[-]	[-]	[kg/m³]	[mm²]	[0.1%]	[kg/h]	[kW]	
1	0	0	0	0.67012	0.00017	0.99935	4.93812	0.000	0.000	0.000	0.0000	0.0000	0.000	0.0000	0.0	0.000	0.0	
2	5	50	0.679	0.6761	0.00122	9.77725	0.00237	10.777	1.002	0.093	0.5283	0.4842	12.510	0.0001	0.0	0.000	0.0	
3	6.2	62	0.728	0.71963	0.00127	9.7692	0.00238	10.769	1.002	0.093	0.5283	0.4842	12.501	0.0001	0.0	0.000	0.0	
4	7.3	73	0.776	0.76745	0.00084	9.75439	0.00237	10.754	1.002	0.093	0.5283	0.4842	12.484	0.0001	0.0	0.000	0.0	
5	7.7	77	0.791	0.78306	0.00266	9.73554	0.0024	10.735	1.002	0.093	0.5283	0.4842	12.462	0.0003	0.1	0.001	0.0	
6	8.1	81	0.811	0.80621	0.00737	9.69363	0.00243	10.693	1.002	0.094	0.5283	0.4842	12.413	0.0097	2.8	0.023	0.3	
7	8.9	89	0.845	0.83863	0.24371	9.64578	0.00248	10.645	1.002	0.094	0.5283	0.4842	12.358	0.0273	7.8	0.065	0.9	
8	9.7	97	0.874	0.86807	0.41991	9.61111	0.00248	10.610	1.002	0.094	0.5283	0.4842	12.317	0.0471	13.4	0.112	1.5	
9	10.9	109	0.928	0.92501	0.79183	9.5579	0.00247	10.557	1.002	0.095	0.5283	0.4842	12.255	0.0893	25.4	0.212	2.8	
10	12.1	121	0.977	0.97428	1.18549	9.50957	0.00267	10.509	1.002	0.095	0.5283	0.4842	12.199	0.1343	38.2	0.318	4.2	
11	14	140	1.055	1.05396	1.79963	9.44448	0.00288	10.444	1.002	0.096	0.5283	0.4842	12.124	0.2052	58.4	0.486	6.5	
12	19.9	199	1.304	1.29166	3.80084	9.31635	0.00404	10.316	1.003	0.097	0.5283	0.4842	11.975	0.4387	124.9	1.039	13.9	
13	30	300	1.729	1.71923	7.1404	9.13468	0.00961	10.134	1.006	0.099	0.5283	0.4842	11.764	0.8389	238.8	1.988	26.5	
14	51.5	515	2.632	2.61591	13.69652	8.74671	0.02034	9.748	1.020	0.105	0.5283	0.4842	11.314	1.6733	476.4	3.964	52.9	
15	70.3	703	3.418	3.40907	18.89768	8.44124	0.03729	9.441	1.037	0.110	0.5283	0.4842	10.969	2.3834	678.5	5.647	75.3	
16	90.2	902	4.253	4.24113	23.89788	8.10036	0.04566	9.100	1.045	0.115	0.5283	0.4842	10.563	3.1269	890.2	7.408	98.8	
17	96.4	964	4.535	4.57854	25.849	7.94371	0.0525	8.943	1.052	0.118	0.5283	0.4842	10.382	3.4415	979.8	8.153	108.7	
-	100	1000	-	-	-	-	-	-	-	-	-	-	-	3.5125	1000.0	8.322	111.0	

Figure C.1: Proportional valve characterization data.

Measurement made with compressed shop air																		
p_amb	0.9994	[bar]																
T_gas	27	[degC]																
R_gas	287	[J/kgK]																
gamma_gas	1.4	[-]																
MP	TRIJEKT_pos	TRIJEKT_pos	voltage_pos	mass_flow	pr_up	pr_dw	p_up	p_dw	PR_meas	PR	psi	rho_up	A_eff		DK_pos	A_eff_openi	A_eff_closin	A_eff_diff
[-]	[%]	[0.1%]	[V]	[kg/h]	[rel.bar]	[rel.bar]	[bar]	[bar]	[-]	[-]	[-]	[kg/m³]	[mm²]		[%]	[mm²]	[mm²]	[%]
1	10.1	101	0.87244	0.46674	9.42972	0	10.429	0.999	0.096	0.5263	0.4842	12.107	0.0533		15.2	0.2498	0.2479	0.74016
2	15.2	152	1.08804	2.1975	9.47593	0	10.475	0.999	0.095	0.5263	0.4842	12.160	0.2498		19.9	0.4304	0.4272	0.74052
3	19.9	199	1.28149	3.76106	9.40577	0	10.405	0.999	0.096	0.5263	0.4842	12.079	0.4304		25	0.6307	0.6288	0.31343
4	25	250	1.4977	5.47249	9.33127	0	10.331	0.999	0.097	0.5263	0.4842	11.992	0.6307		30	0.8269	0.8360	-1.10071
5	30	300	1.70683	7.12414	9.25823	0	10.258	0.999	0.097	0.5263	0.4842	11.908	0.8269		35.1	1.0236	1.0269	-0.32723
6	35.1	351	1.92376	8.74021	9.16746	0	10.167	0.999	0.098	0.5263	0.4842	11.802	1.0236		40.2	1.2256	1.2272	-0.12975
7	40.2	402	2.13838	10.373	9.07795	0	10.077	0.999	0.099	0.5263	0.4842	11.698	1.2256		45.3	1.4236	1.4253	-0.12478
8	45.3	453	2.34971	11.93945	8.98672	0	9.986	0.999	0.100	0.5263	0.4842	11.592	1.4236		50.3	1.6153	1.6122	0.18820
9	50.3	503	2.55654	13.42696	8.89813	0	9.897	0.999	0.101	0.5263	0.4842	11.490	1.6153		55	1.7942	1.7948	-0.03539
10	55	550	2.75548	14.77774	8.80764	0	9.807	0.999	0.102	0.5263	0.4842	11.385	1.7942		60.1	1.9889	1.9964	-0.37632
11	60.1	601	2.97301	16.2138	8.70718	0	9.707	0.999	0.103	0.5263	0.4842	11.268	1.9889		65.2	2.1808	2.1763	0.20812
12	65.2	652	3.18245	17.59369	8.6062	0	9.606	0.999	0.104	0.5263	0.4842	11.151	2.1808		70.3	2.3680	2.3798	-0.50218
13	70.3	703	3.39677	18.87891	8.49338	0	9.493	0.999	0.105	0.5263	0.4842	11.020	2.3680		75.3	2.5659	2.5765	-0.41455
14	75.3	753	3.61191	20.20593	8.37685	0	9.376	0.999	0.107	0.5263	0.4842	10.884	2.5659		80.4	2.7416	2.7508	-0.33539
15	80.4	804	3.81241	21.3201	8.25967	0	9.259	0.999	0.108	0.5263	0.4842	10.748	2.7416		85.1	2.9186	2.9259	-0.25097
16	85.1	851	4.01533	22.3848	8.13271	0	9.132	0.999	0.109	0.5263	0.4842	10.601	2.9186		90.2	3.1024	3.1061	-0.11808
17	90.2	902	4.23504	23.39623	7.97972	0	8.979	0.999	0.111	0.5263	0.4842	10.423	3.1024		95.3	3.2923	3.2923	0.00000
18	95.3	953	4.44573	24.52019	7.8685	0	8.868	0.999	0.113	0.5263	0.4842	10.294	3.2923					
19	90.2	902	4.23446	23.55977	8.03182	0	9.031	0.999	0.111	0.5263	0.4842	10.484	3.1061					
20	85.1	851	4.01608	22.54414	8.17489	0	9.174	0.999	0.109	0.5263	0.4842	10.650	2.9259					
21	80.4	804	3.81313	21.48924	8.30193	0	9.301	0.999	0.107	0.5263	0.4842	10.797	2.7508					
22	75.3	753	3.61487	20.37848	8.41788	0	9.417	0.999	0.106	0.5263	0.4842	10.932	2.5765					
23	70.3	703	3.40175	19.04817	8.53113	0	9.530	0.999	0.105	0.5263	0.4842	11.064	2.3798					
24	65.2	652	3.18382	17.62474	8.64322	0	9.643	0.999	0.104	0.5263	0.4842	11.194	2.1763					
25	60.1	601	2.97555	16.33962	8.74583	0	9.745	0.999	0.103	0.5263	0.4842	11.313	1.9964					
26	55	550	2.75814	14.84714	8.85021	0	9.850	0.999	0.101	0.5263	0.4842	11.434	1.7948					
27	50.3	503	2.55902	13.4415	8.92753	0	9.927	0.999	0.101	0.5263	0.4842	11.524	1.6122					
28	45.3	453	2.34889	11.98072	9.00875	0	10.008	0.999	0.100	0.5263	0.4842	11.618	1.4253					
29	40.2	402	2.13353	10.40095	9.09201	0	10.091	0.999	0.099	0.5263	0.4842	11.715	1.2272					
30	35.1	351	1.92433	8.77245	9.17168	0	10.171	0.999	0.098	0.5263	0.4842	11.807	1.0269					
31	30	300	1.71268	7.19439	9.2466	0	10.246	0.999	0.098	0.5263	0.4842	11.894	0.8360					
32	25	250	1.49703	5.45425	9.32921	0	10.329	0.999	0.097	0.5263	0.4842	11.990	0.6288					
33	19.9	199	1.28374	3.73351	9.40661	0	10.406	0.999	0.096	0.5263	0.4842	12.080	0.4272					
34	15.2	152	1.08703	2.18141	9.47677	0	10.476	0.999	0.095	0.5263	0.4842	12.161	0.2479					
35	10.1	101	0.87066	0.40364	9.59689	0	10.596	0.999	0.094	0.5263	0.4842	12.301	0.0454					

Figure C.2: Proportional valve hysteresis characterization data.

C.7 Rotary Distributor Characterization

The rotary distributor, Verteiler 160 A, was characterized using compressed shop air by changing the distributor input shaft angle and measuring the corresponding air mass flow rate and upstream and downstream pressures. The angular sweep extends from 0° to 180° input shaft angle.

The ambient pressure and gas temperature used in the distributor calculation are

$$p_{amb} = 1.0033 \text{ bar} \tag{C.26}$$

and

$$T_{gas} = 23\,^{\circ}\mathrm{C}, \tag{C.27}$$

respectively.

For each calculated measurement point, the absolute pressures, upstream density, measured pressure ratio, pressure ratio used in the flow function, and isentropic flow function are obtained according to Equations C.1–C.10.

The same pressure-ratio logic is applied throughout the complete angular sweep. When PR_{meas} falls below the critical value, $PR = PR_{crit}$ is used in the calculation of ψ. When PR_{meas} exceeds the critical value, the measured pressure ratio is used directly. The effective-area expression itself remains unchanged for all distributor measurement points.

The distributor effective area is calculated from Equation C.12. The closed-position value is then subtracted according to Equation C.14 to obtain $A_{eff,off}$ as a function of the distributor input shaft angle.

The complete set of measured variables and calculated quantities for the rotary distributor is presented in Figure C.3.

Measurement made with compressed shop air												
p_amb	1.0033	[bar]										
T_gas	23	[degC]										
R_gas	287	[J/kgK]										
gamma_gas	1.4	[-]										
MP	vert_in-shaf	mass_flow	pr_up	pr_dw	p_up	p_dw	PR_meas	PR	psi	rho_up	A_eff	A_eff_off
[-]	[deg]	[kg/h]	[rel.bar]	[rel.bar]	[bar]	[bar]	[-]	[-]	[-]	[kg/m^3]	[mm^2]	[mm^2]
1	0	0.40266	1.0033	0.00161	0	0	0.0000	0.0000	0.0000	0.0000	0.0000	0.00
2	0	3.06477	6.06198	0.00161	7.06528	1.00491	0.1422	0.5283	0.4842	8.3126	1.3614	0.00
3	6	3.09699	6.00799	0.00168	7.01129	1.00498	0.1433	0.5283	0.4842	8.2491	1.3810	0.02
4	12	3.10744	5.99641	0.00171	6.99971	1.00501	0.1436	0.5283	0.4842	8.2354	1.3868	0.03
5	18	3.18298	5.97555	0.00169	6.97885	1.00499	0.1440	0.5283	0.4842	8.2109	1.4227	0.06
6	21	3.47002	5.94236	0.00197	6.94566	1.00527	0.1447	0.5283	0.4842	8.1718	1.5547	0.19
7	24	13.50235	5.42796	0.196	6.43126	1.1993	0.1865	0.5283	0.4842	7.5666	6.2867	4.93
8	27	23.20046	4.71545	0.94664	5.71875	1.94994	0.3410	0.5283	0.4842	6.7283	11.4553	10.09
9	30	30.38027	4.38074	1.63636	5.38404	2.63966	0.4903	0.5283	0.4842	6.3345	15.4595	14.10
10	33	33.10928	4.01654	1.89956	5.01984	2.90286	0.5783	0.5783	0.4815	5.9060	17.5456	16.18
11	36	34.55936	3.83846	2.0498	4.84176	3.0531	0.6306	0.6306	0.4728	5.6965	18.9895	17.63
12	39	35.7212	3.75329	2.14808	4.75659	3.15138	0.6625	0.6625	0.4644	5.5963	20.1611	18.80
13	42	36.41768	3.7083	2.20465	4.7116	3.20795	0.6809	0.6809	0.4585	5.5434	20.9200	19.56
14	45	37.08445	3.68313	2.25811	4.68643	3.26141	0.6959	0.6959	0.4530	5.5138	21.6211	20.26
15	48	37.30049	3.67929	2.29443	4.68259	3.29773	0.7043	0.7043	0.4496	5.5093	21.9164	20.56
16	51	37.73567	3.68617	2.3325	4.68947	3.3358	0.7113	0.7113	0.4467	5.5173	22.3032	20.94
17	54	37.98504	3.69374	2.36002	4.69704	3.36332	0.7161	0.7161	0.4446	5.5263	22.5361	21.17
18	57	38.30066	3.70335	2.38078	4.70665	3.38408	0.7190	0.7190	0.4433	5.5376	22.7676	21.41
19	60	38.42828	3.71502	2.40034	4.71832	3.40364	0.7214	0.7214	0.4422	5.5513	22.8706	21.51
20	63	38.6564	3.7233	2.41375	4.7266	3.41705	0.7229	0.7229	0.4415	5.5610	23.0239	21.66
21	66	38.24844	3.66257	2.37527	4.66587	3.37857	0.7241	0.7241	0.4410	5.4896	22.9567	21.60
22	69	37.89109	3.61138	2.34226	4.61468	3.34556	0.7250	0.7250	0.4406	5.4294	22.8893	21.53
23	72	37.31057	3.54869	2.30022	4.55199	3.30352	0.7257	0.7257	0.4402	5.3556	22.7114	21.35
24	75	36.87866	3.47792	2.25577	4.48122	3.25907	0.7273	0.7273	0.4395	5.2723	22.6626	21.30
25	78	36.77156	3.46377	2.2529	4.46707	3.2562	0.7289	0.7289	0.4387	5.2557	22.6734	21.31
26	81	37.09385	3.49955	2.28846	4.50285	3.29176	0.7310	0.7310	0.4377	5.2978	22.8340	21.47
27	84	37.59519	3.54278	2.32151	4.54608	3.32481	0.7314	0.7314	0.4375	5.3486	23.0404	21.68
28	87	37.88737	3.58832	2.35523	4.59162	3.35853	0.7314	0.7314	0.4375	5.4022	23.1064	21.74
29	90	38.20425	3.62366	2.38272	4.62696	3.38602	0.7318	0.7318	0.4373	5.4438	23.2197	21.86
30	93	38.52627	3.66015	2.41178	4.66345	3.41508	0.7323	0.7323	0.4370	5.4867	23.3368	21.98
31	96	38.69361	3.66883	2.42195	4.67213	3.42525	0.7331	0.7331	0.4366	5.4969	23.4378	22.08
32	99	38.88651	3.68809	2.43921	4.69139	3.44251	0.7338	0.7338	0.4363	5.5196	23.5240	22.16
33	102	38.97284	3.69045	2.44268	4.69375	3.44598	0.7342	0.7342	0.4361	5.5224	23.5802	22.22
34	105	38.87694	3.70377	2.45231	4.70707	3.45561	0.7341	0.7341	0.4361	5.5381	23.4881	22.13
35	108	39.13584	3.71484	2.45778	4.71814	3.46108	0.7336	0.7336	0.4364	5.5511	23.6017	22.24
36	111	38.79212	3.67672	2.42638	4.68002	3.42968	0.7328	0.7328	0.4368	5.5062	23.4700	22.11
37	114	38.10099	3.6061	2.37147	4.6094	3.37477	0.7321	0.7321	0.4371	5.4231	23.2100	21.85
38	117	37.63634	3.55004	2.3214	4.55334	3.3247	0.7302	0.7302	0.4381	5.3572	23.0169	21.66
39	120	37.11609	3.50966	2.28309	4.51296	3.28639	0.7282	0.7282	0.4390	5.3097	22.7513	21.39
40	123	36.57222	3.4645	2.24156	4.4678	3.24486	0.7263	0.7263	0.4399	5.2565	22.4839	21.12
41	126	37.02432	3.52561	2.27476	4.52891	3.27806	0.7238	0.7238	0.4411	5.3284	22.5485	21.19
42	129	37.31818	3.57992	2.30082	4.58322	3.30412	0.7209	0.7209	0.4424	5.3923	22.5244	21.16
43	132	37.6036	3.64942	2.33201	4.65272	3.33531	0.7169	0.7169	0.4443	5.4741	22.4337	21.07
44	135	37.88357	3.70071	2.34582	4.70401	3.34912	0.7120	0.7120	0.4464	5.5345	22.3696	21.01
45	138	37.81133	3.73452	2.34171	4.73782	3.34501	0.7060	0.7060	0.4489	5.5742	22.1226	20.76
46	141	37.65367	3.77731	2.32927	4.78061	3.33257	0.6971	0.6971	0.4525	5.6246	21.7576	20.40
47	144	37.54847	3.83765	2.31343	4.84095	3.31673	0.6851	0.6851	0.4570	5.6956	21.3498	19.99
48	147	37.44277	3.91975	2.29449	4.92305	3.29779	0.6699	0.6699	0.4622	5.7922	20.8748	19.51
49	150	36.42661	4.01858	2.20563	5.02188	3.20893	0.6390	0.6390	0.4709	5.9084	19.7357	18.37
50	153	35.15838	4.15702	2.08165	5.16032	3.08495	0.5978	0.5978	0.4790	6.0713	18.4728	17.11
51	156	31.97156	4.44181	1.76943	5.44511	2.77273	0.5092	0.5283	0.4842	6.4064	16.1778	14.82
52	159	26.79172	4.89677	1.2642	5.90007	2.2675	0.3843	0.5283	0.4842	6.9417	13.0236	11.66
53	162	18.25308	5.46128	0.50073	6.46458	1.50403	0.2327	0.5283	0.4842	7.6058	8.4767	7.12
54	165	5.80524	6.0453	0.00896	7.0486	1.01226	0.1436	0.5283	0.4842	8.2930	2.5818	1.22
55	168	3.29398	6.1486	0.0027	7.1519	1.006	0.1407	0.5283	0.4842	8.4145	1.4543	0.09
56	171	3.20065	6.14804	0.00255	7.15134	1.00585	0.1407	0.5283	0.4842	8.4138	1.4132	0.05
57	177	3.18188	6.14772	0.00253	7.15102	1.00583	0.1407	0.5283	0.4842	8.4135	1.4049	0.04
58	180	3.17888	6.14446	0.00251	7.14776	1.00581	0.1407	0.5283	0.4842	8.4096	1.4039	0.04

Figure C.3: Rotary distributor measurement data and results.

Appendix D

Individual Engine Test Campaign Results

This appendix presents the additional results obtained for the individual test campaigns. The contour maps of the main engine operating parameters are included for completeness and complement the results discussed in the main body of the dissertation.

D.1 VSR004 (Extended Hose Length)

Figures D.1 to D.5 summarize the overall engine behaviour obtained during campaign VSR004, in which the extended hydrogen connection hose was used. The contour maps show a consistent dependence of the main performance and mixture parameters on engine load. As IMEP increases, the injected hydrogen mass increases substantially, from approximately 6–7 mg/cycle at 3 bar IMEP to approximately 15–16 mg/cycle at 9 bar and approximately 20 mg/cycle at 12 bar. At the same time, λ decreases from values close to 5 at low load to approximately 2.4–2.7 at the highest tested loads. This reflects the progressively larger fuel quantity required to increase engine load relative to the available air mass.

The increase in load is accompanied by a marked improvement in brake specific fuel consumption and thermal efficiency. At 1200 rpm, BSFC decreases from 118.0 g/kWh at 3 bar IMEP to 78.5 g/kWh at 9 bar, while thermal efficiency increases from 25.5% to 38.2%. A similar trend is observed at 1500 and 1800 rpm. The highest thermal efficiency measured in this campaign is 39.4% at 1500 rpm and 12 bar IMEP, corresponding to a BSFC of 76.1 g/kWh. In contrast, the low-load operating points show the highest BSFC values, particularly at 1800 rpm, where 162.5 g/kWh is measured at 3 bar IMEP together with a thermal efficiency of 18.5%. This behaviour is consistent with the increasing relative influence of friction, pumping, and auxiliary losses when the brake output is low.

Engine speed also affects the mixture and efficiency characteristics. For a given IMEP, the higher-speed operating points generally require a slightly greater hydrogen mass and operate at a higher λ. For example, at 6 bar IMEP the injected hydrogen mass increases from 10.1 mg/cycle at

1200 rpm to 10.7 mg/cycle at 1800 rpm, while λ increases from 3.0 to 3.8. Over the same range, thermal efficiency decreases from 36.2% to 32.0% and BSFC increases from 83.0 to 93.7 g/kWh. The influence of engine speed on efficiency becomes less pronounced at the highest loads, where the operating points converge towards lower BSFC and higher thermal efficiency.

The NO_x distribution differs from the smoother trends observed for fuel consumption, efficiency, and mixture strength. Most operating points remain at comparatively low brake-specific NO_x levels, whereas the 1200 rpm, 9 bar IMEP point reaches approximately 2.5 g/kWh. At 1500 rpm and 12 bar IMEP, the measured value is approximately 0.5 g/kWh, while the corresponding high-load points at 1800 rpm remain close to 0.1 g/kWh. The high value at 1200 rpm and 9 bar occurs together with the lowest λ measured at 9 bar IMEP and relatively high thermal efficiency, indicating that the conditions at this operating point are more favourable to NO_x formation. However, the contour maps alone are not sufficient to identify the individual contributions of local temperature, oxygen concentration, and combustion phasing to this behaviour.

Overall, the VSR004 results show that the principal variation across the operating map is governed by engine load. Increasing IMEP requires a larger hydrogen quantity and reduces λ, while simultaneously improving BSFC and thermal efficiency. Engine speed has a secondary but clearly observable influence, particularly at low and medium load, where higher speed is associated with greater specific fuel consumption and lower thermal efficiency.

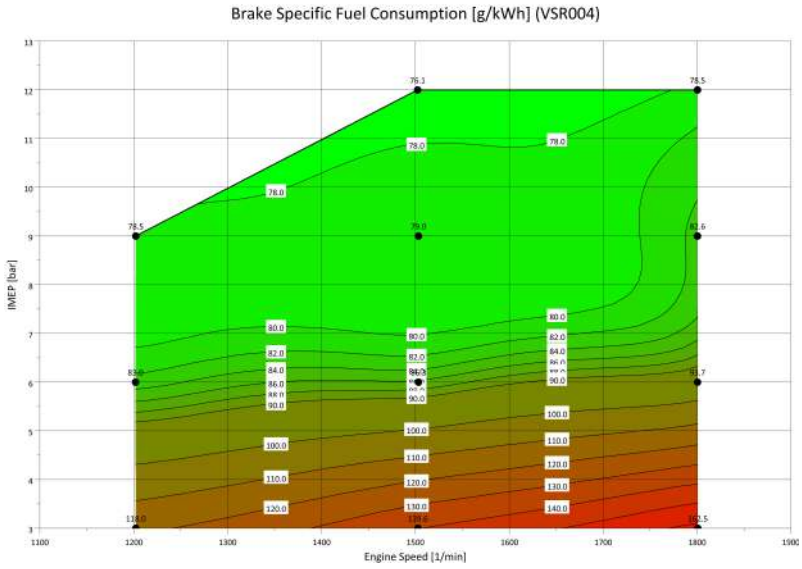


Figure D.1: Contour map of brake specific fuel consumption as a function of engine speed and IMEP for campaign VSR004 (Extended Hose Length).

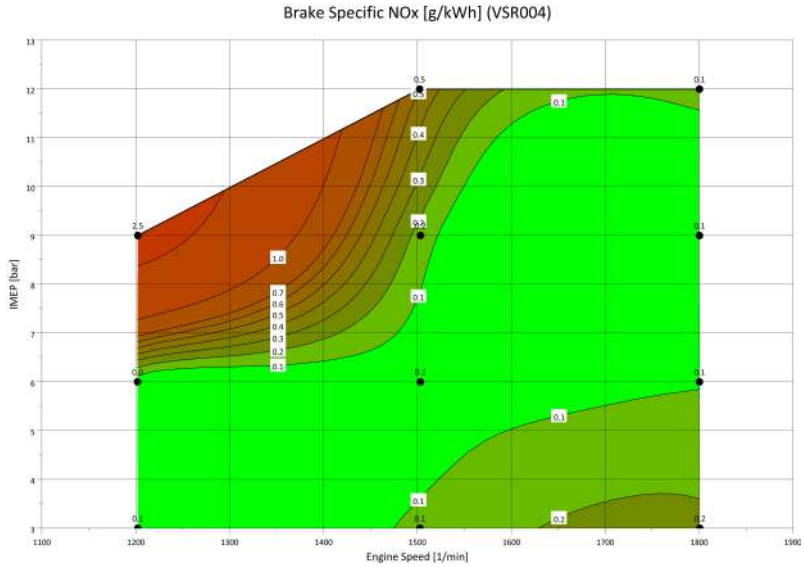


Figure D.2: Contour map of brake specific NO_x emissions as a function of engine speed and IMEP for campaign VSR004 (Extended Hose Length).

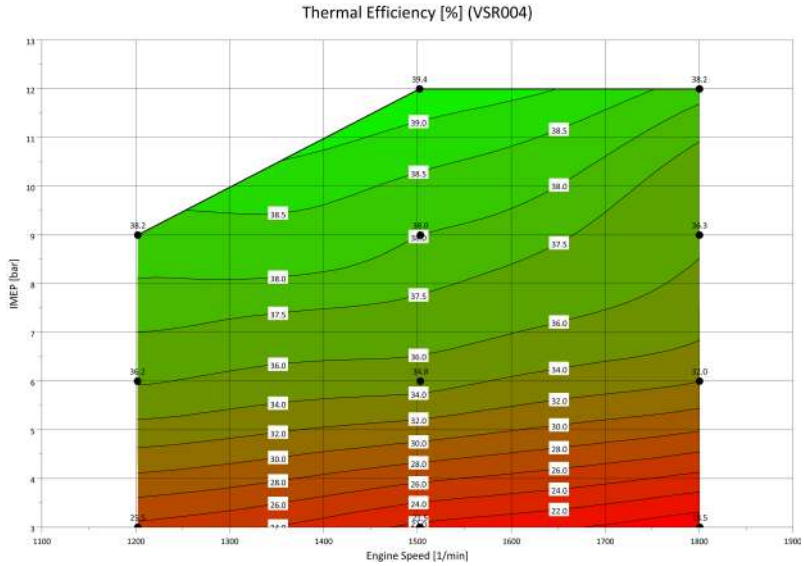


Figure D.3: Contour map of thermal efficiency as a function of engine speed and IMEP for campaign VSR004 (Extended Hose Length).

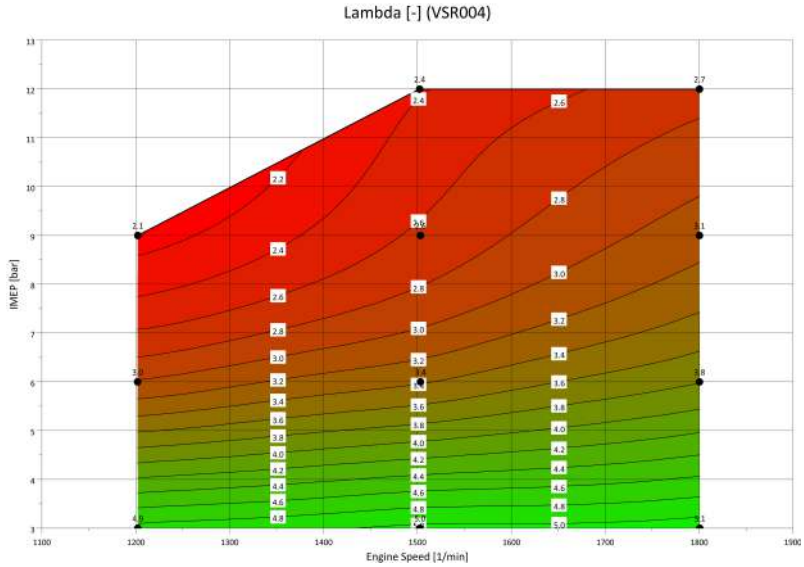


Figure D.4: Contour map of lambda as a function of engine speed and IMEP for campaign VSR004 (Extended Hose Length).

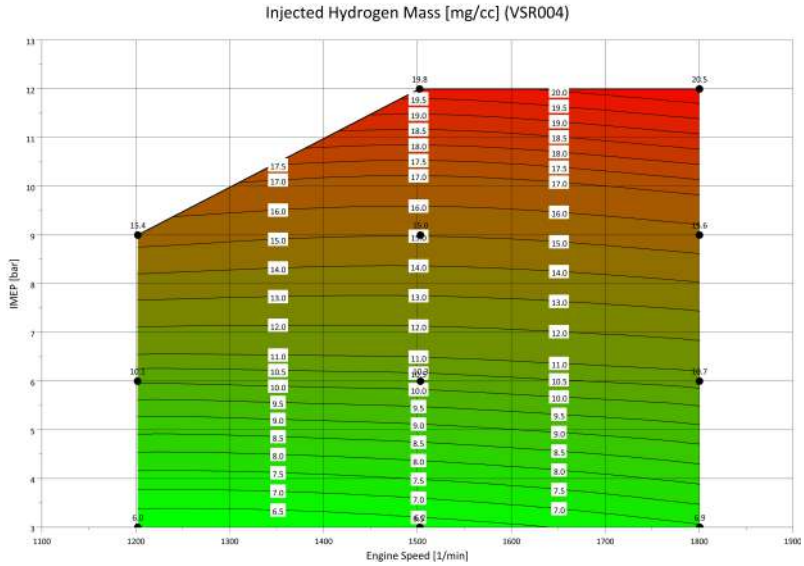


Figure D.5: Contour map of injected hydrogen mass per cycle as a function of engine speed and IMEP for campaign VSR004 (Extended Hose Length).

D.2 VSR005 (Reduced Hose Diameter)

Figures D.6 to D.10 summarize the engine operating characteristics obtained during campaign VSR005, in which the reduced diameter hydrogen connection hose was used. As in the other investigated configurations, engine load is the main parameter governing the variation of the mixture and performance quantities. Increasing IMEP requires a progressively larger hydrogen quantity,

while the excess-air ratio decreases. At 1200 rpm, for example, the injected hydrogen mass increases from approximately 5.9 mg/cycle at 3 bar IMEP to 15.4 mg/cycle at 9 bar, while λ decreases from approximately 5.0 to 2.1. At the highest investigated load, the injected hydrogen mass reaches approximately 19.9 mg/cycle at 1500 rpm and 20.6 mg/cycle at 1800 rpm, with corresponding λ values of approximately 2.4 and 2.7, respectively.

The increase in load is accompanied by a substantial reduction in brake specific fuel consumption and a corresponding increase in thermal efficiency. At 1200 rpm, BSFC decreases from 127.1 g/kWh at 3 bar IMEP to 79.2 g/kWh at 9 bar, while thermal efficiency increases from 23.8% to 37.9%. The same trend is observed at 1500 and 1800 rpm. The highest thermal efficiency measured in VSR005 is 38.9% at 1500 rpm and 12 bar IMEP, where the corresponding BSFC is 77.1 g/kWh. In contrast, the least favourable fuel consumption condition occurs at 1800 rpm and 3 bar IMEP, where BSFC reaches 172.2 g/kWh and thermal efficiency falls to 17.7%. This behaviour reflects the larger relative contribution of friction, pumping, and auxiliary losses when the brake output is low.

Engine speed has a particularly clear influence at low and medium load. At 6 bar IMEP, the injected hydrogen mass increases from 10.1 mg/cycle at 1200 rpm to 10.9 mg/cycle at 1800 rpm, while λ increases from approximately 3.0 to 3.7. Over the same speed range, BSFC increases from 83.2 to 95.6 g/kWh and thermal efficiency decreases from 36.1% to 31.4%. At higher load, these differences become smaller. At 12 bar IMEP, for example, the thermal efficiency is 38.9% at 1500 rpm and 37.7% at 1800 rpm, indicating that the effect of engine speed on overall efficiency is less pronounced under the highest load conditions.

The brake-specific NO_x distribution again shows a different pattern from the smoother variation of fuel consumption and efficiency. The majority of the operating map remains at comparatively low NO_x levels, particularly at 1800 rpm, where values between approximately 0.1 and 0.2 g/kWh are measured over the investigated load range. A pronounced increase occurs at 1200 rpm and 9 bar IMEP, where the measured value reaches approximately 5.2 g/kWh. This operating point also corresponds to the lowest measured λ in the VSR005 map, approximately 2.1. At 1500 rpm, NO_x also increases towards the highest load, reaching approximately 1.1 g/kWh at 12 bar IMEP. These results show that NO_x formation is strongly dependent on the specific combustion conditions and cannot be described by load alone. The contour maps do not, however, allow the individual effects of combustion temperature, local mixture distribution, and combustion phasing to be separated.

Overall, the VSR005 maps show that increasing engine load is associated with a higher hydrogen requirement, a reduction in λ, lower BSFC, and higher thermal efficiency. Increasing engine speed generally has an unfavourable effect on fuel consumption and efficiency at low and medium load, whereas the differences become smaller at high load. The NO_x response is more localized, with the highest emissions occurring in the high load, low speed region rather than following the global efficiency trend directly.

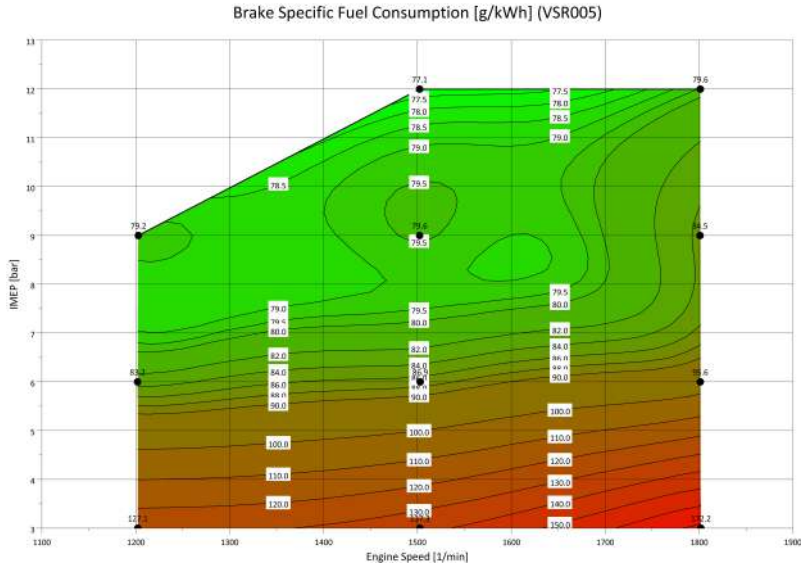


Figure D.6: Contour map of brake specific fuel consumption as a function of engine speed and IMEP for campaign VSR005 (Reduced Hose Diameter).

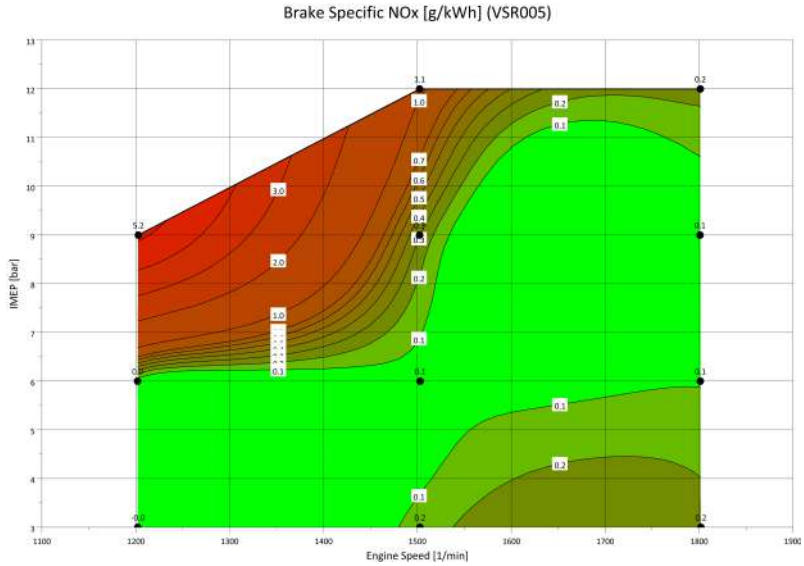


Figure D.7: Contour map of brake specific NO_x emissions as a function of engine speed and IMEP for campaign VSR005 (Reduced Hose Diameter).

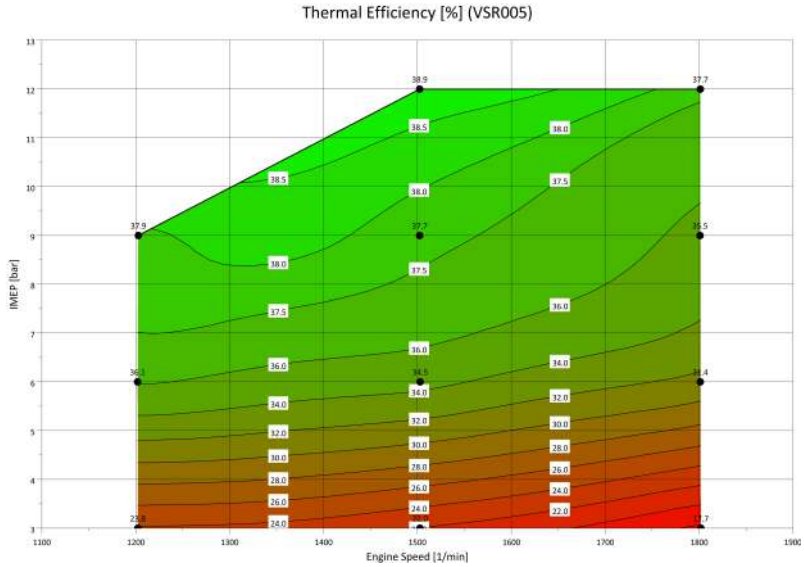


Figure D.8: Contour map of thermal efficiency as a function of engine speed and IMEP for campaign VSR005 (Reduced Hose Diameter).

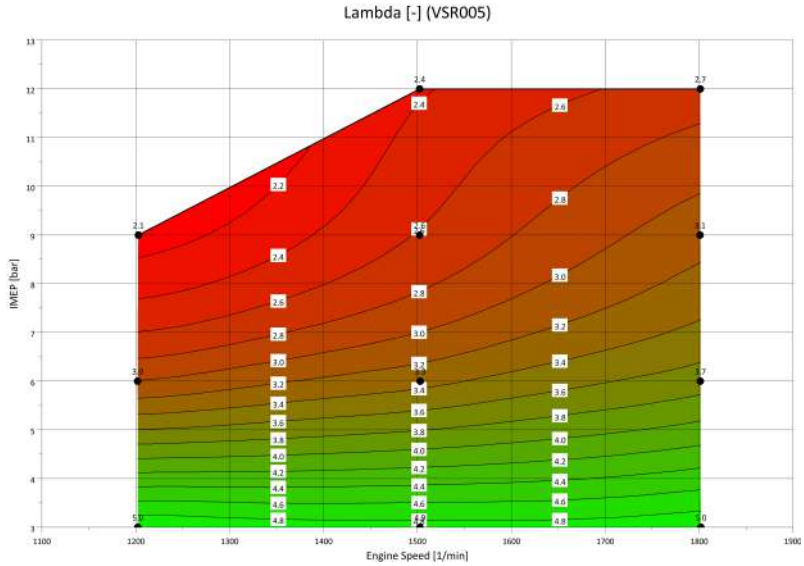


Figure D.9: Contour map of lambda as a function of engine speed and IMEP for campaign VSR005 (Reduced Hose Diameter).

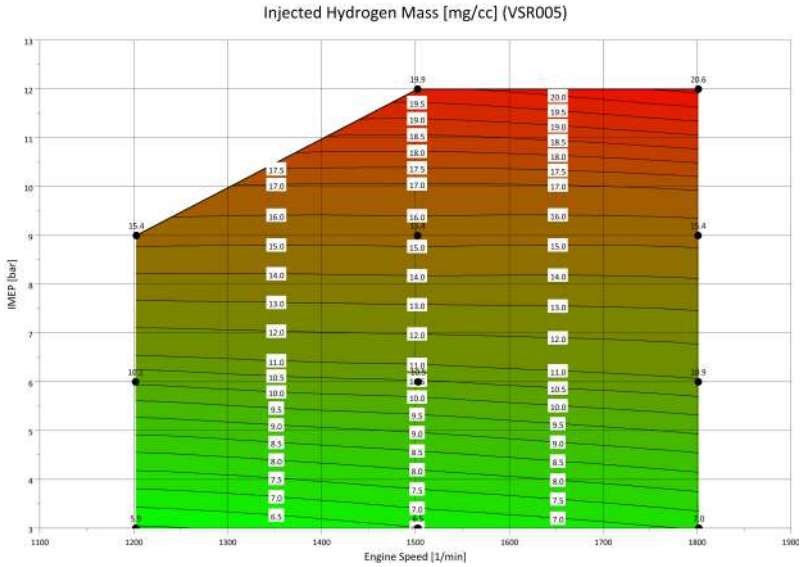


Figure D.10: Contour map of injected hydrogen mass per cycle as a function of engine speed and IMEP for campaign VSR005 (Reduced Hose Diameter).

D.3 VSR006 (Without Check Valve)

Figures D.11 to D.15 summarize the engine operating characteristics obtained during campaign VSR006, in which the check valve was removed while the nozzle was retained. The contour maps show that the main variations in mixture strength, fuel consumption, and efficiency remain primarily governed by engine load. Increasing IMEP requires a progressively larger injected hydrogen mass and is accompanied by a reduction in λ. At 1200 rpm, the injected hydrogen mass increases from approximately 5.7 mg/cycle at 3 bar IMEP to 15.4 mg/cycle at 9 bar, while λ decreases from approximately 5.0 to 2.1. At 12 bar IMEP, the hydrogen mass reaches approximately 19.9 mg/cycle at 1500 rpm and 20.5 mg/cycle at 1800 rpm, with corresponding λ values of approximately 2.3 and 2.7.

The increase in load is accompanied by a substantial reduction in brake specific fuel consumption and an increase in thermal efficiency. At 1200 rpm, BSFC decreases from 122.1 g/kWh at 3 bar IMEP to 78.6 g/kWh at 9 bar, while thermal efficiency increases from 24.7% to 38.2%. The same general behaviour is observed at the other engine speeds. The highest thermal efficiency measured in VSR006 is approximately 39.5% at 1500 rpm and 12 bar IMEP, where the corresponding BSFC is approximately 75.9 g/kWh. Conversely, the least favourable fuel consumption condition occurs at 1800 rpm and 3 bar IMEP, where BSFC reaches approximately 167.0 g/kWh and thermal efficiency decreases to approximately 18.0%. As in the other campaigns, this behaviour is consistent with the larger relative contribution of friction, pumping, and auxiliary losses when brake output is low.

Engine speed has a clear influence at low and medium load. At 6 bar IMEP, the injected hydrogen mass varies from approximately 10.3 mg/cycle at 1200 rpm to 10.6 mg/cycle at 1800 rpm,

while λ increases from approximately 2.9 to 3.7. Over the same speed range, BSFC increases from 82.3 to 93.1 g/kWh and thermal efficiency decreases from 36.4% to 32.2%. The influence of speed becomes less pronounced at higher load. At 12 bar IMEP, for example, thermal efficiency decreases only from approximately 39.5% at 1500 rpm to 38.1% at 1800 rpm.

The brake-specific NO_x distribution is more localized than the variations in BSFC, thermal efficiency, or hydrogen mass. Most of the operating map remains at very low NO_x levels, particularly at 1500 and 1800 rpm. A clear increase occurs at 1200 rpm and 9 bar IMEP, where the measured value reaches approximately 2.7 g/kWh. This point also corresponds to one of the lowest λ values in the VSR006 map, approximately 2.1. At 1500 rpm and 12 bar IMEP, the measured NO_x level is approximately 0.6 g/kWh, while the corresponding high-load point at 1800 rpm remains close to 0.1 g/kWh. The contour maps therefore indicate that NO_x formation depends strongly on the specific combustion conditions rather than on load alone. The available data do not allow the separate effects of local mixture distribution, combustion temperature, and combustion phasing to be quantified.

Overall, VSR006 preserves the same principal operating map behaviour observed in the other configurations: increasing load requires more hydrogen and reduces λ, while simultaneously improving BSFC and thermal efficiency. Increasing engine speed is generally unfavourable to efficiency at low and medium load, whereas the differences become smaller towards the highest loads. The removal of the check valve therefore does not produce a fundamental change in the global trends of the engine map. Its more specific influence on fuel line dynamics and cylinder behaviour must instead be assessed from the direct pressure trace comparisons between VSR006 and the baseline configuration.

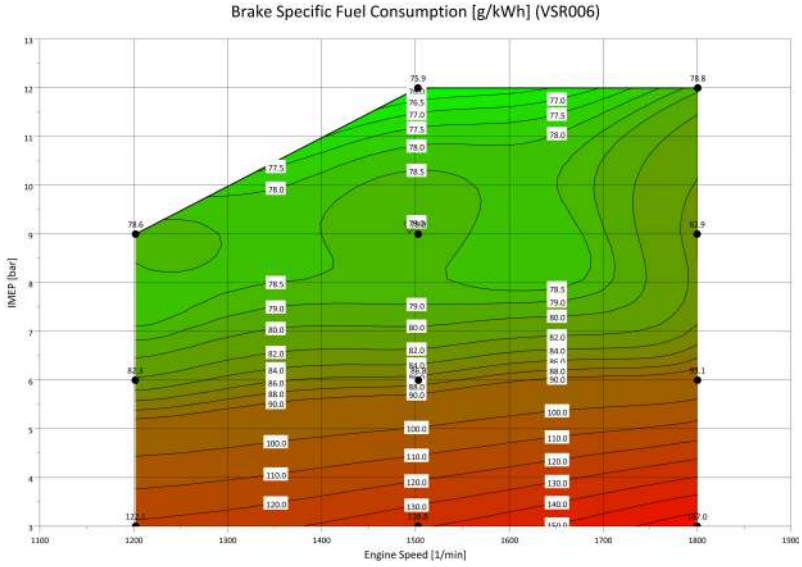


Figure D.11: Contour map of brake specific fuel consumption as a function of engine speed and IMEP for campaign VSR006 (Without Check Valve).

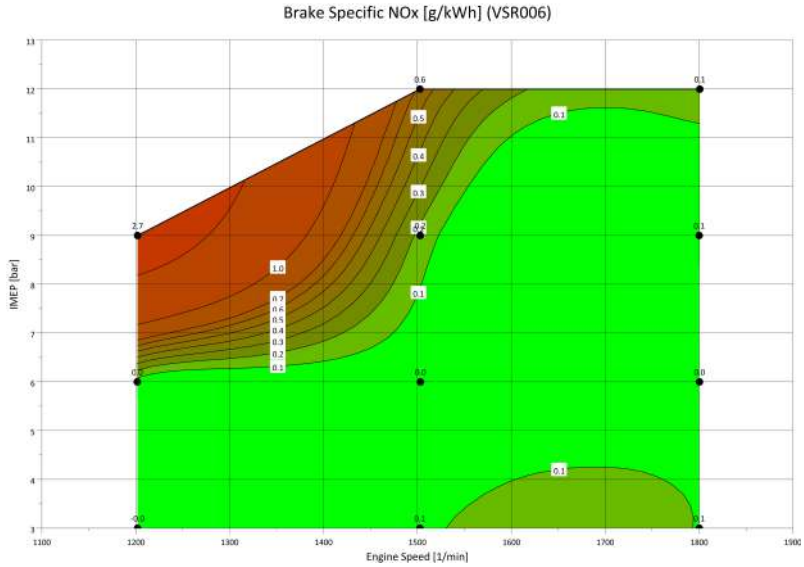


Figure D.12: Contour map of brake specific NO_x emissions as a function of engine speed and IMEP for campaign VSR006 (Without Check Valve).

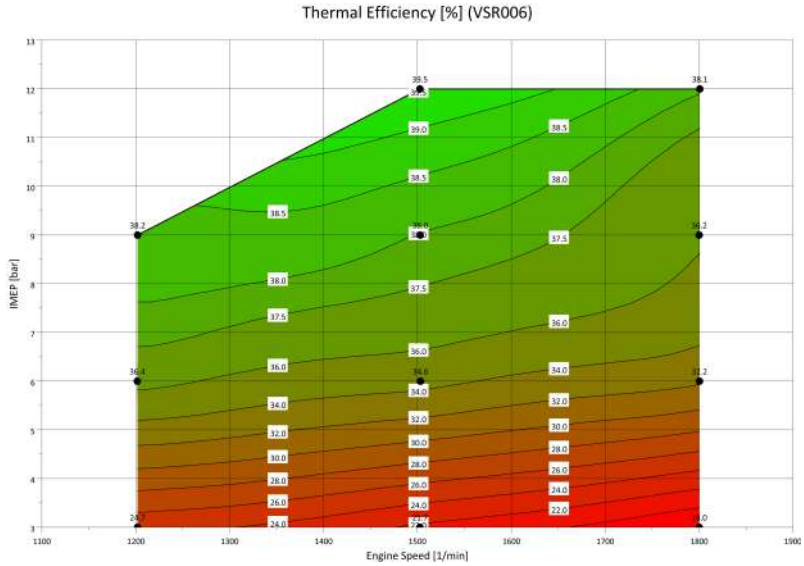


Figure D.13: Contour map of thermal efficiency as a function of engine speed and IMEP for campaign VSR006 (Without Check Valve).

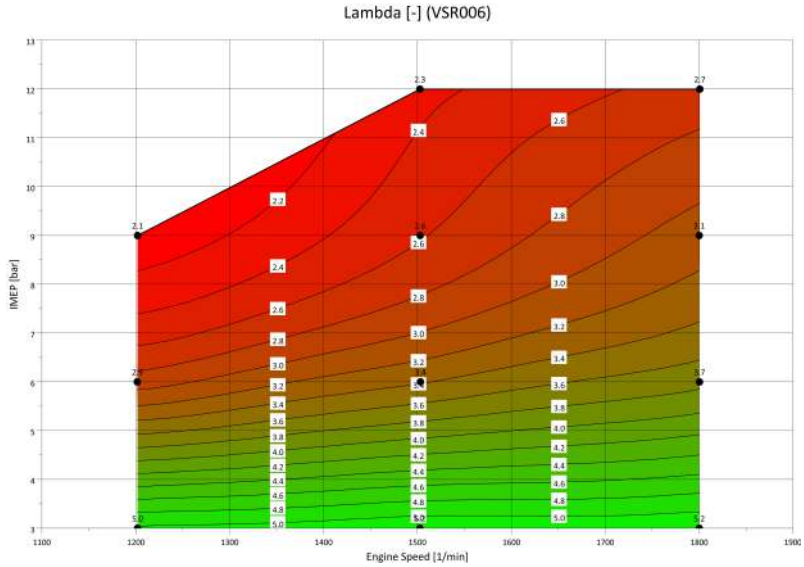


Figure D.14: Contour map of lambda as a function of engine speed and IMEP for campaign VSR006 (Without Check Valve).

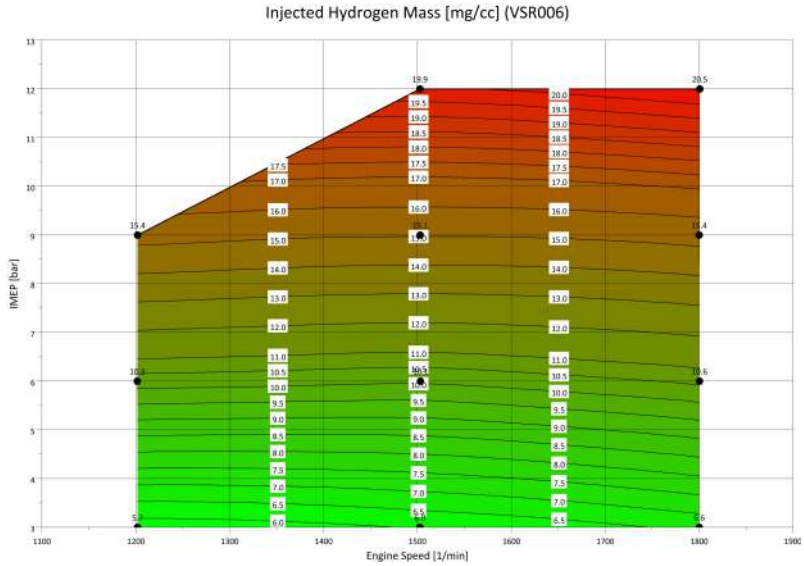


Figure D.15: Contour map of injected hydrogen mass per cycle as a function of engine speed and IMEP for campaign VSR006 (Without Check Valve).

D.4 VSR008 (Without Check Valve and Nozzle)

Figures D.16 to D.20 summarize the engine operating characteristics obtained during campaign VSR008, in which both the check valve and the nozzle were removed from the cylinder 4 hydrogen delivery branch. The contour maps show that the main variation of the mixture and performance parameters remains predominantly governed by engine load. Increasing IMEP requires a larger injected hydrogen mass and is accompanied by a reduction in the excess-air ratio. At 1200 rpm, the

injected hydrogen mass increases from approximately 5.8 mg/cycle at 3 bar IMEP to 15.7 mg/cycle at 9 bar, while λ decreases from approximately 4.9 to 2.0. At the highest investigated load, the injected hydrogen mass reaches approximately 20.1 mg/cycle at 1500 rpm and 20.3 mg/cycle at 1800 rpm, with corresponding λ values of approximately 2.3 and 2.7.

The increase in load is again associated with a clear reduction in brake specific fuel consumption and an increase in thermal efficiency. At 1200 rpm, BSFC decreases from 119.5 g/kWh at 3 bar IMEP to 78.2 g/kWh at 9 bar, while thermal efficiency increases from 25.2% to 38.4%. The same general trend is observed at 1500 and 1800 rpm. The highest thermal efficiency measured in VSR008 is 39.7% at 1500 rpm and 12 bar IMEP, where the corresponding BSFC is 75.5 g/kWh. In contrast, the least favourable operating point in terms of fuel consumption occurs at 1800 rpm and 3 bar IMEP, where BSFC reaches 177.8 g/kWh and thermal efficiency decreases to 16.9%. As observed in the other campaigns, the low load penalty is consistent with friction, pumping, and auxiliary losses representing a larger fraction of the brake output.

The effect of engine speed remains most evident at low and medium load. At 6 bar IMEP, the injected hydrogen mass changes only moderately, from 10.1 mg/cycle at 1200 rpm to 10.6 mg/cycle at 1800 rpm, while λ increases from approximately 2.9 to 3.7. Over the same speed range, BSFC increases from 82.1 to 93.5 g/kWh and thermal efficiency decreases from 36.6% to 32.1%. At higher load, the efficiency difference with engine speed becomes smaller. At 12 bar IMEP, thermal efficiency is 39.7% at 1500 rpm and 38.2% at 1800 rpm.

The brake-specific NO_x distribution is more localized than the mixture and efficiency trends. Most operating points remain at low NO_x levels, particularly at 1500 and 1800 rpm. The most pronounced increase occurs at 1200 rpm and 9 bar IMEP, where the measured value reaches approximately 4.6 g/kWh. This point also corresponds to the lowest λ measured in the VSR008 map, approximately 2.0. At 1500 rpm and 12 bar IMEP, the measured NO_x value is approximately 0.9 g/kWh, while the corresponding 1800 rpm point remains close to 0.2 g/kWh. These results confirm that NO_x formation is highly dependent on the local combustion conditions and does not follow a simple monotonic dependence on load. The available contour maps do not allow the separate contributions of mixture distribution, combustion temperature, and combustion phasing to be determined.

Overall, VSR008 maintains the same principal operating map trends observed in the other configurations: increasing load requires a larger hydrogen quantity, reduces λ, and improves both BSFC and thermal efficiency, while increasing engine speed generally has a less favourable effect at low and medium load. The removal of both the check valve and the nozzle therefore does not fundamentally alter the global engine map behaviour. Its more specific effect is instead observed in the cycle resolved pressure comparisons, particularly in the increased pressure communication between the intake system and the cylinder 4 hydrogen line.

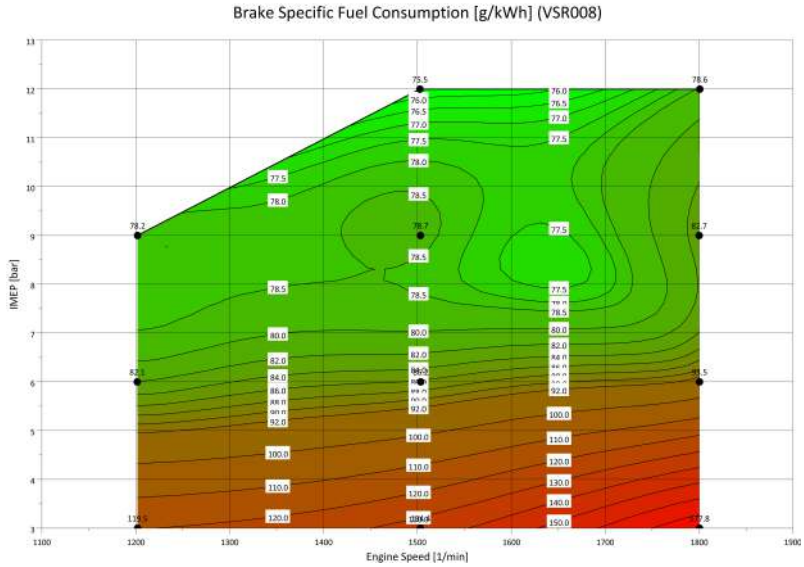


Figure D.16: Contour map of brake specific fuel consumption as a function of engine speed and IMEP for campaign VSR008 (Without Check Valve and Nozzle).

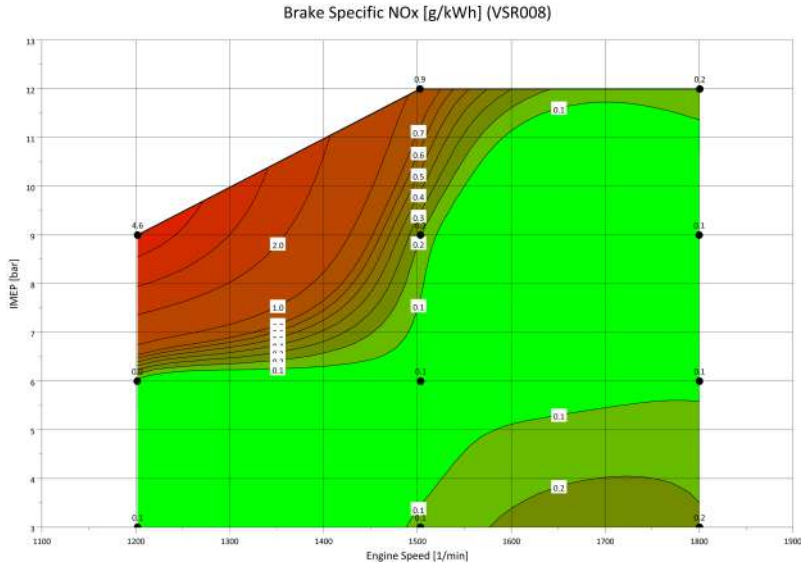


Figure D.17: Contour map of brake specific NO_x emissions as a function of engine speed and IMEP for campaign VSR008 (Without Check Valve and Nozzle).

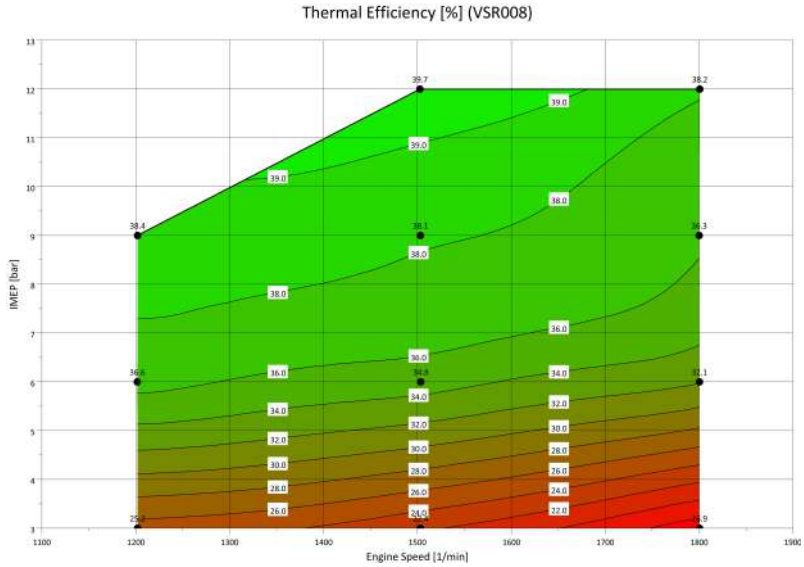


Figure D.18: Contour map of thermal efficiency as a function of engine speed and IMEP for campaign VSR008 (Without Check Valve and Nozzle).

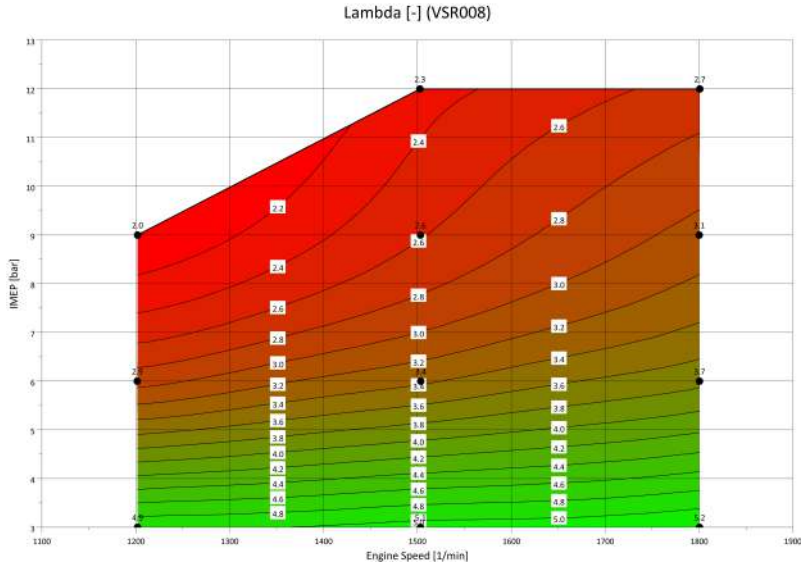


Figure D.19: Contour map of lambda as a function of engine speed and IMEP for campaign VSR008 (Without Check Valve and Nozzle).

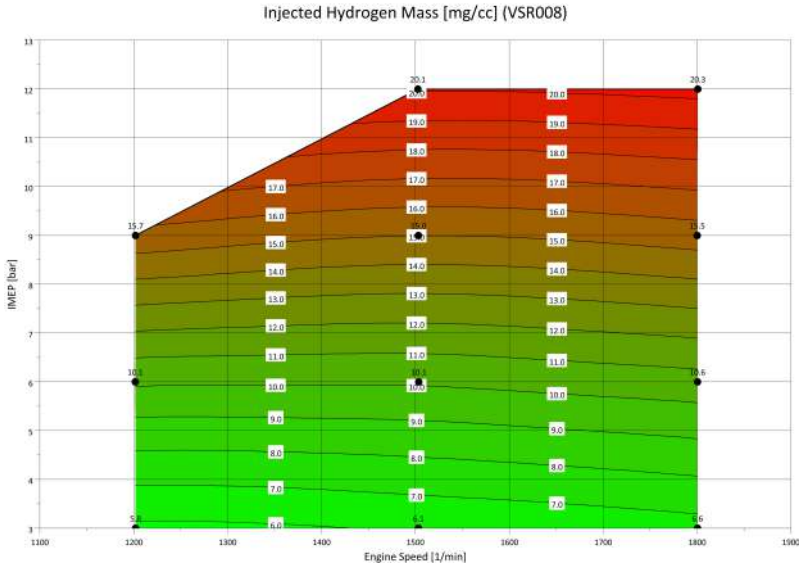


Figure D.20: Contour map of injected hydrogen mass per cycle as a function of engine speed and IMEP for campaign VSR008 (Without Check Valve and Nozzle).

D.5 VSR009 (Modified Injection Timing)

Figures D.21 to D.25 summarize the engine operating characteristics obtained during campaign VSR009, in which the start of injection was delayed from SOI $= -340\,$dCA to SOI $= -300\,$dCA. The contour maps show that the main variation of the mixture and performance parameters remains primarily governed by engine load. Increasing IMEP requires a progressively larger hydrogen quantity and is accompanied by a reduction in λ. At 1200 rpm, the injected hydrogen mass increases from approximately 5.5 mg/cycle at 3 bar IMEP to 15.3 mg/cycle at 9 bar, while λ decreases from approximately 5.2 to 2.1. At 12 bar IMEP, the injected hydrogen mass reaches approximately 19.8 mg/cycle at 1500 rpm and 20.0 mg/cycle at 1800 rpm, with corresponding λ values of approximately 2.3 and 2.7.

The increase in load is accompanied by a clear reduction in brake specific fuel consumption and an increase in thermal efficiency. At 1200 rpm, BSFC decreases from 137.8 g/kWh at 3 bar IMEP to 79.6 g/kWh at 9 bar, while thermal efficiency increases from 21.9% to 37.7%. The same general trend is observed at 1500 and 1800 rpm. The highest thermal efficiency measured in VSR009 is 39.2% at 1500 rpm and 12 bar IMEP, where the corresponding BSFC is 76.5 g/kWh. At 1800 rpm and 3 bar IMEP, BSFC reaches 161.0 g/kWh and thermal efficiency decreases to 18.7%. As observed in the other campaigns, the low-load operating points therefore present the least favourable fuel consumption performance, consistent with the larger relative contribution of friction, pumping, and auxiliary losses when brake output is low.

Engine speed again has its clearest influence at low and medium load. At 6 bar IMEP, the injected hydrogen mass remains close to 10.4–10.5 mg/cycle across the investigated speed range, whereas λ increases from approximately 2.9 at 1200 rpm to 3.7 at 1800 rpm. Over the same range,

BSFC increases from 83.8 to 93.5 g/kWh and thermal efficiency decreases from 35.8% to 32.1%. At 12 bar IMEP, the influence of speed is smaller, with thermal efficiency decreasing from 39.2% at 1500 rpm to 38.2% at 1800 rpm.

The brake specific NO_x distribution remains strongly dependent on the operating condition. Most of the map presents low NO_x levels, particularly at 1800 rpm, where values remain close to 0.1–0.2 g/kWh over the investigated load range. A pronounced increase occurs at 1200 rpm and 9 bar IMEP, where the measured value reaches approximately 5.0 g/kWh. This point also corresponds to one of the lowest air-fuel ratios in the map, with $\lambda \approx 2.1$. At 1500 rpm, NO_x also increases towards the highest load, reaching approximately 1.5 g/kWh at 12 bar IMEP. These results show that the NO_x response is more sensitive to the specific combustion conditions than the smoother trends observed for fuel consumption and thermal efficiency. The contour maps alone do not allow the individual effects of mixture distribution, combustion temperature, and combustion phasing to be separated.

Overall, VSR009 maintains the same principal engine map trends observed in the other campaigns: increasing load requires more hydrogen, reduces λ, and improves both BSFC and thermal efficiency, while higher engine speed is generally associated with lower efficiency at low and medium load. Delaying the start of injection therefore does not fundamentally alter the global structure of the engine operating map. Its more specific influence is better identified from the direct comparison with VSR002, where the later injection shifts the fuel delivery event while the crank angle position of the maximum in-cylinder pressure remains nearly unchanged.

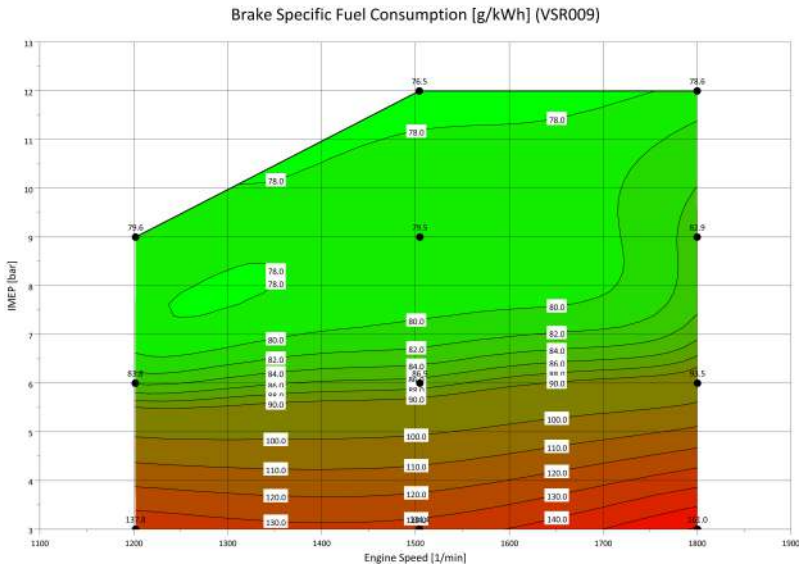


Figure D.21: Contour map of brake specific fuel consumption as a function of engine speed and IMEP for campaign VSR009 (Modified Injection Timing).

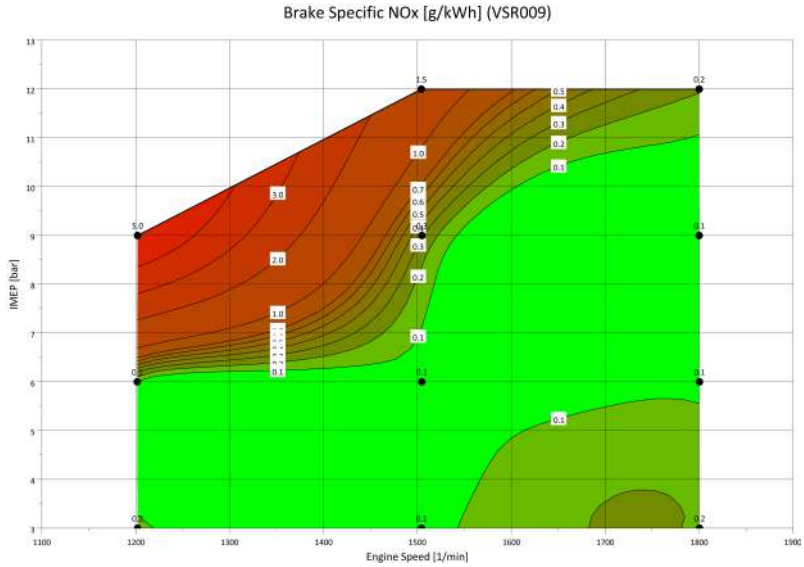


Figure D.22: Contour map of brake specific NO_x emissions as a function of engine speed and IMEP for campaign VSR009 (Modified Injection Timing).

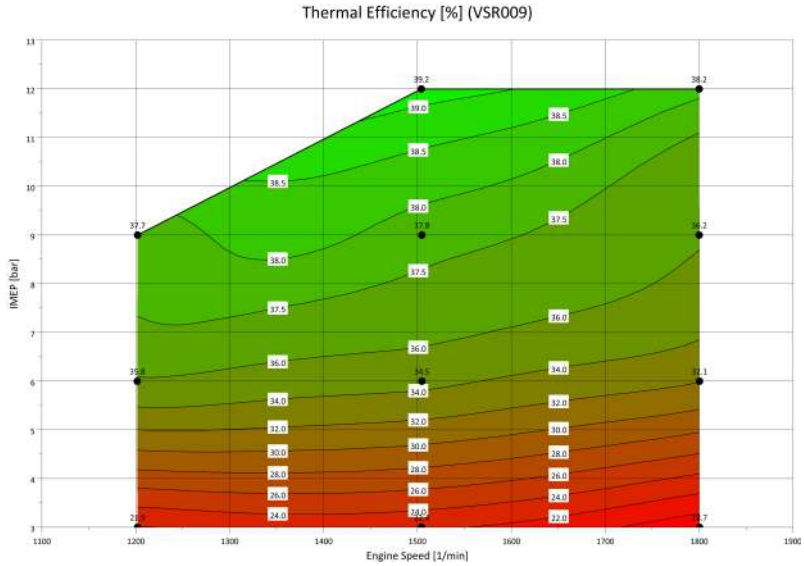


Figure D.23: Contour map of thermal efficiency as a function of engine speed and IMEP for campaign VSR009 (Modified Injection Timing).

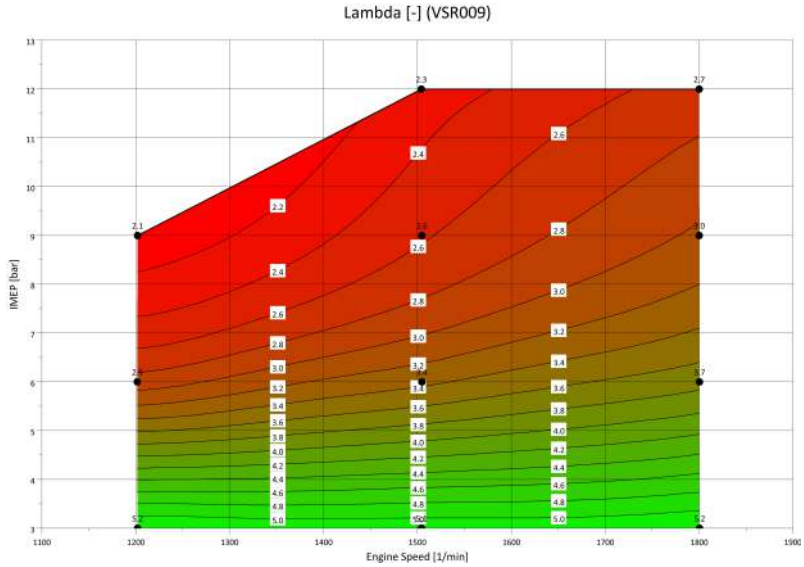


Figure D.24: Contour map of lambda as a function of engine speed and IMEP for campaign VSR009 (Modified Injection Timing).

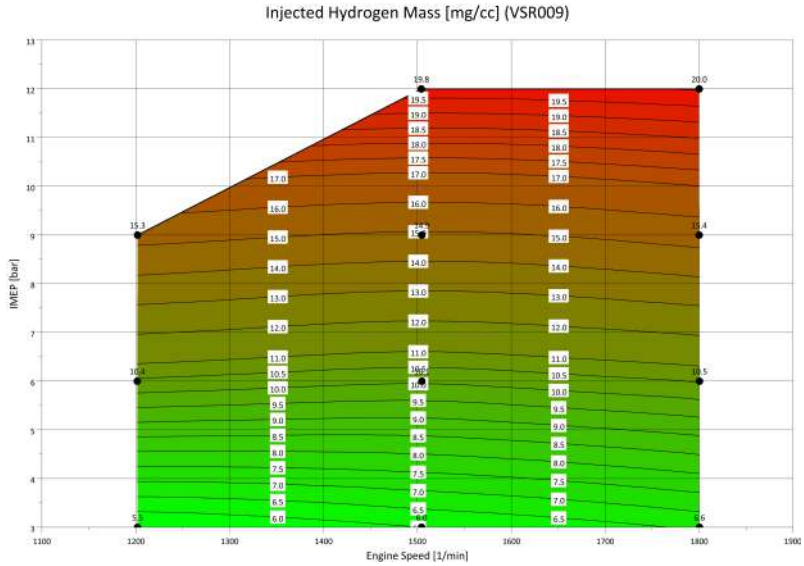


Figure D.25: Contour map of injected hydrogen mass per cycle as a function of engine speed and IMEP for campaign VSR009 (Modified Injection Timing).

Appendix E

Additional Comparative Engine Test Results

This appendix presents the additional comparisons between the tested fuel system configurations at low and medium load operating points. These results complement the representative high load comparisons presented in the main body and are used to verify whether the identified trends are maintained across the investigated operating range.

E.1 Hose Geometry Comparison

E.1.1 Low Load: MP001

At the low-load operating point MP001 (1200 rpm and 3 bar IMEP), the influence of hose geometry remains visible primarily in the cylinder 4 fuel line. The reduced diameter configuration, VSR005, produces the largest pressure oscillations, while the extended hose used in VSR004 also changes the timing and amplitude of the pressure wave response relative to the baseline. The multiple pressure peaks observed during the fuel delivery event are consistent with the propagation and reflection of pressure waves within the compressible hydrogen line rather than with separate injection events. When the distributor opens, the resulting pressure disturbance travels along the hose and can be partially reflected at changes in flow area and at downstream components such as the nozzle and check valve. The interaction between incident and reflected waves produces the successive pressure maximum and minimum visible in the signal. This effect is particularly pronounced in VSR005, where the reduced hose diameter modifies both the flow restriction and the dynamic response of the line, while the increased hose length in VSR004 changes the propagation time and therefore the phase of the pressure oscillations.

These changes in the injection line are accompanied by a progressive reduction in peak in-cylinder pressure from VSR002 to VSR004 and VSR005, indicating that the hose modifications affect the resulting combustion even at low load. The stronger pressure oscillations do not necessarily imply a larger total injected hydrogen mass, but they can modify the temporal distribution

of the fuel delivered to the intake port and therefore influence mixture formation and combustion development.

The distributor upstream, intake manifold, and exhaust manifold pressures retain their characteristic periodic behaviour, with smaller differences between the configurations. In the region associated with the cylinder 4 exhaust event, VSR005 presents the lowest pressure contribution, consistent with its lower in-cylinder pressure. Overall, the low load results support the same main conclusion obtained at high load: reducing the hose diameter has a stronger influence on the fuel delivery dynamics and combustion response than increasing the hose length. No clear indication of abnormal combustion, such as pre-ignition, knock, or an isolated intake backfire event, is evident from the presented pressure traces.

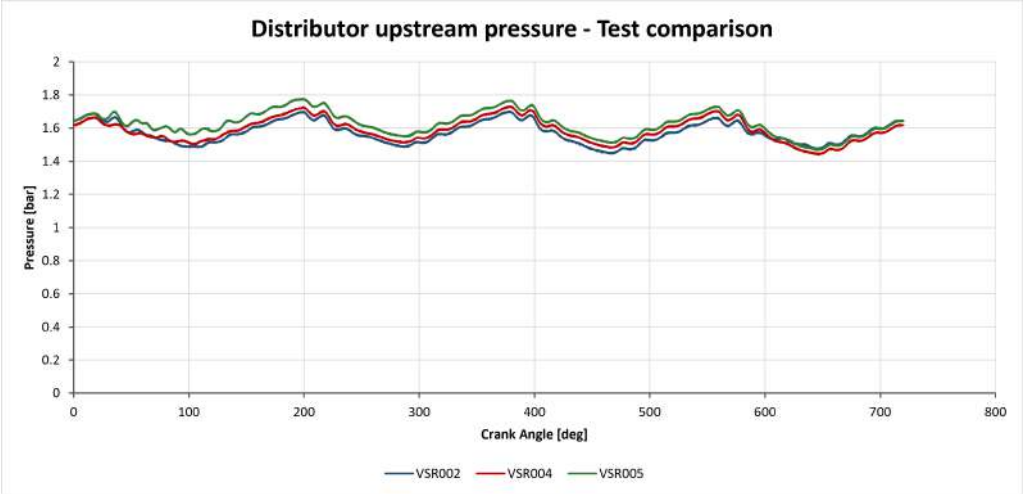


Figure E.1: Comparison of the distributor upstream pressure traces for MP001.

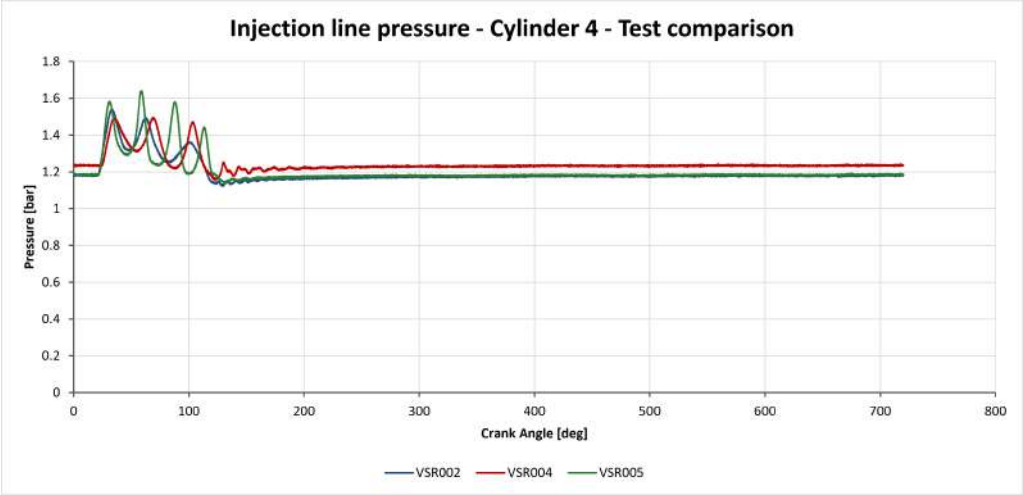


Figure E.2: Comparison of the injection line pressure traces on cylinder 4 for MP001.

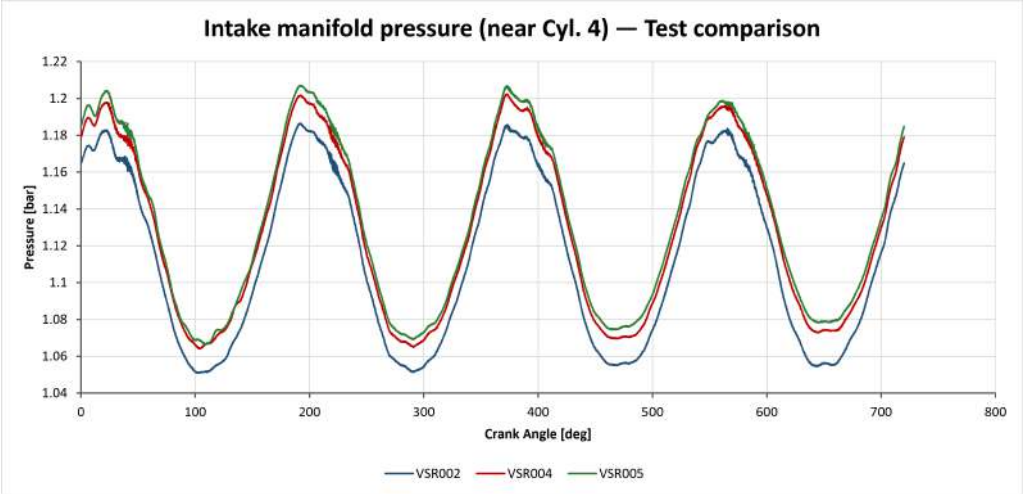


Figure E.3: Comparison of the intake manifold pressure traces on cylinder 4 for MP001.

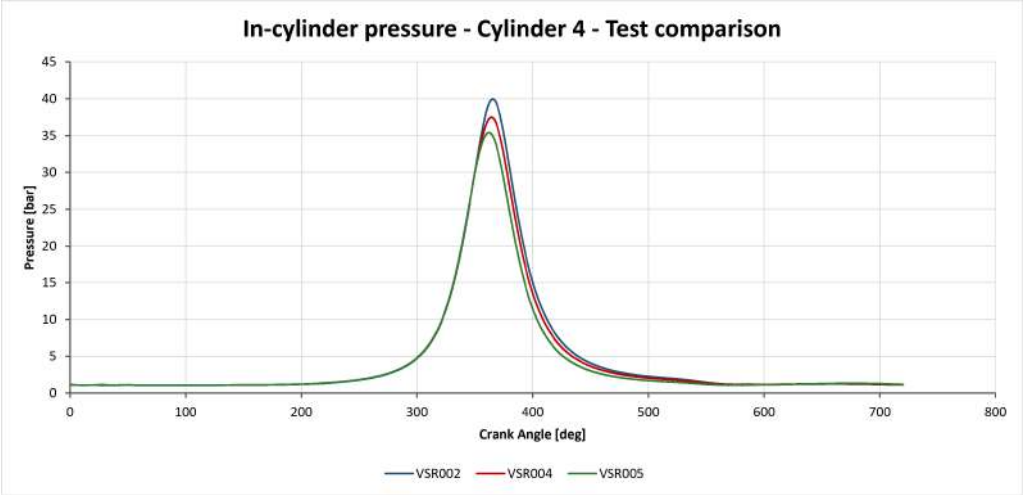


Figure E.4: Comparison of the in-cylinder pressure traces on cylinder 4 for MP001.

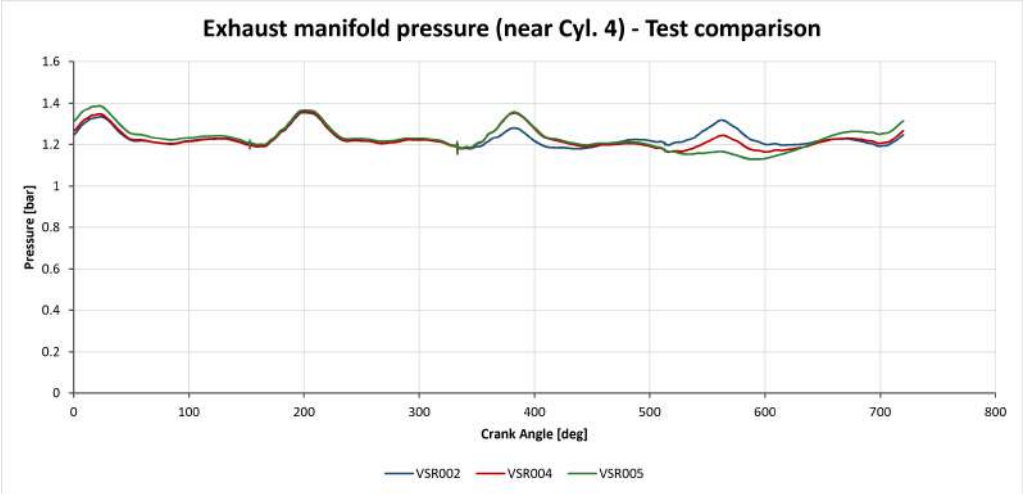


Figure E.5: Comparison of the exhaust manifold pressure traces on cylinder 4 for MP001.

E.1.2 Mid Load: MP005

At the medium-load operating point MP005 (1500 rpm and 6 bar IMEP), the influence of hose geometry remains clearly visible in the cylinder 4 fuel delivery and combustion response. The injection line pressure shows different transient behaviour for the three configurations. VSR005 produces the largest initial pressure peak, whereas VSR004 presents more evident pressure oscillations after the main fuel delivery transient. These differences are consistent with the effect of the reduced hose diameter on flow restriction and line dynamics, and with the effect of the increased hose length on pressure wave propagation and reflection.

The resulting in-cylinder pressure follows the same general trend observed at low and high load. VSR002 produces the highest peak pressure, VSR004 presents an intermediate response, and VSR005 produces the lowest peak. The similarity in the crank angle position of the pressure maxima indicates that the main difference is in the magnitude of the combustion response rather than in a substantial displacement of combustion phasing. The lower cylinder pressure obtained with VSR005 therefore confirms that reducing the hose diameter has a stronger influence on cylinder 4 operation than increasing the hose length.

The distributor upstream and intake manifold pressures retain their characteristic periodic behaviour, although some differences in absolute pressure level are present between the campaigns. Since these measurements represent common parts of the fuel and air systems, these differences cannot be attributed exclusively to cylinder 4. In the exhaust manifold, the pressure pulse associated with the cylinder 4 exhaust event is also lower for VSR005, which is consistent with its reduced in-cylinder pressure. Overall, the medium load results support the trend observed at the other operating points and confirm the greater sensitivity of the fuel delivery system to hose diameter than to the increase in hose length considered in VSR004. No clear indication of pre-ignition, knock, or an isolated intake backfire event is evident from these pressure traces.

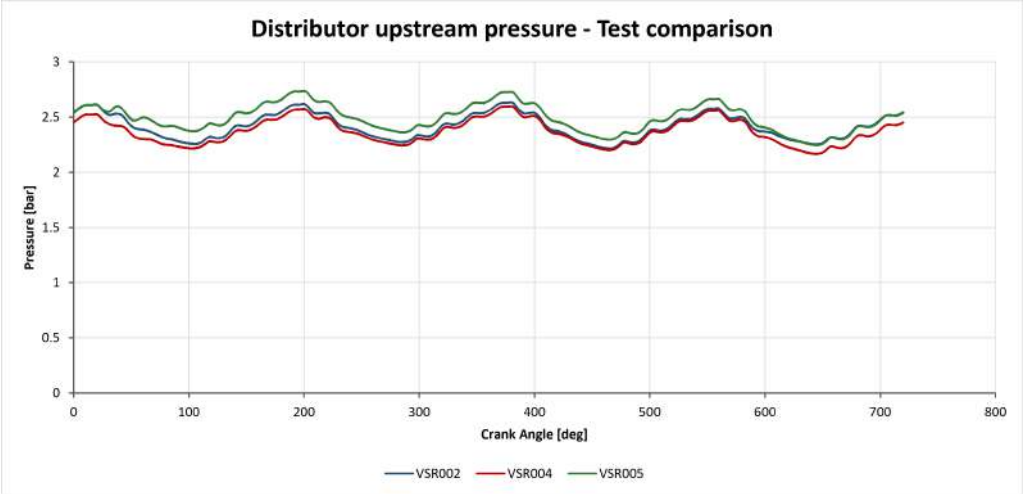


Figure E.6: Comparison of the distributor upstream pressure traces for MP005.

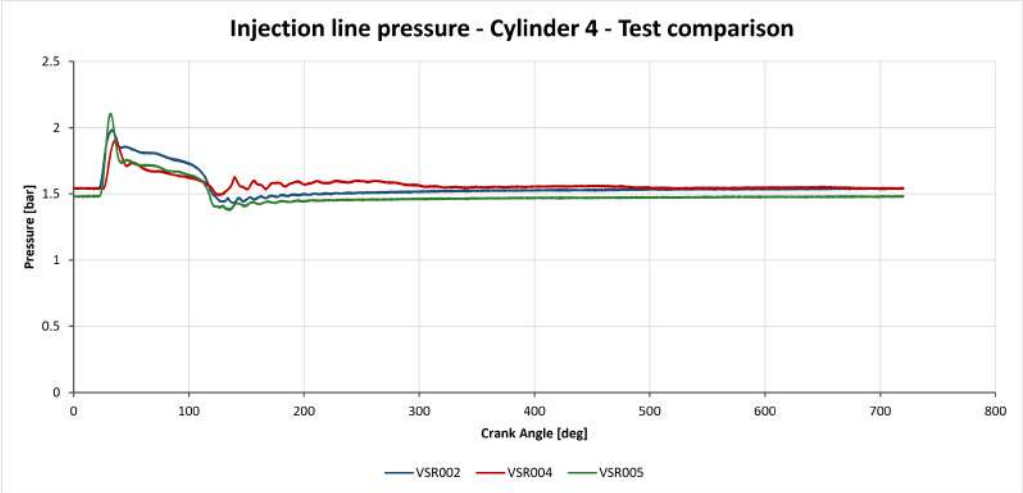


Figure E.7: Comparison of the injection line pressure traces on cylinder 4 for MP005.

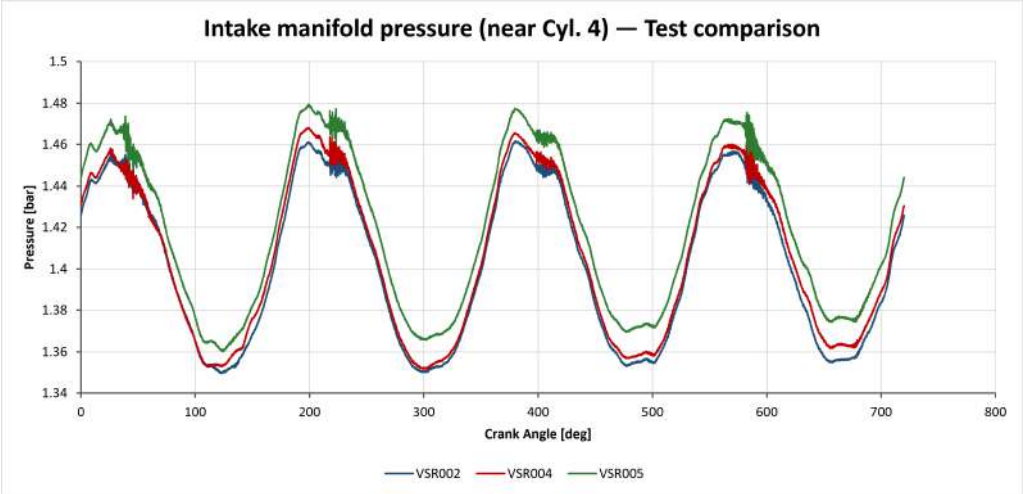


Figure E.8: Comparison of the intake manifold pressure traces on cylinder 4 for MP005.

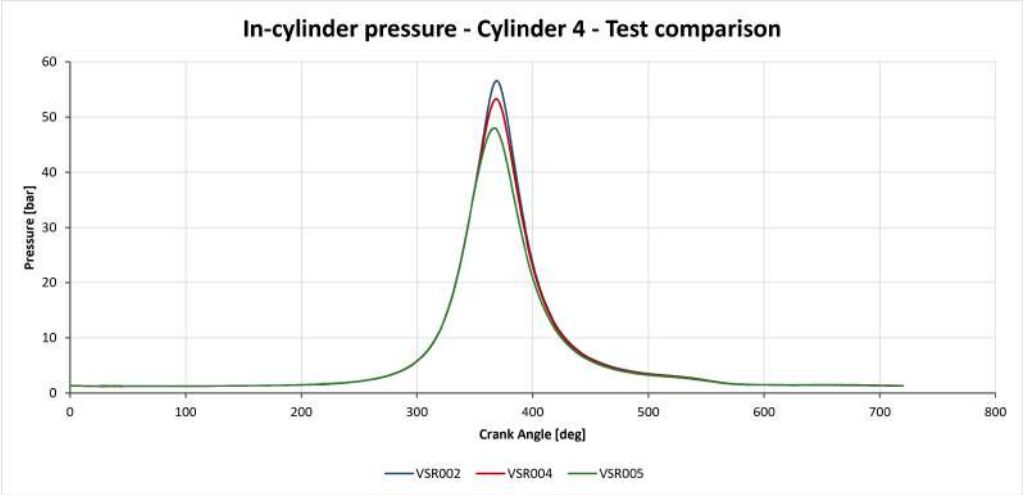


Figure E.9: Comparison of the in-cylinder pressure traces on cylinder 4 for MP005.

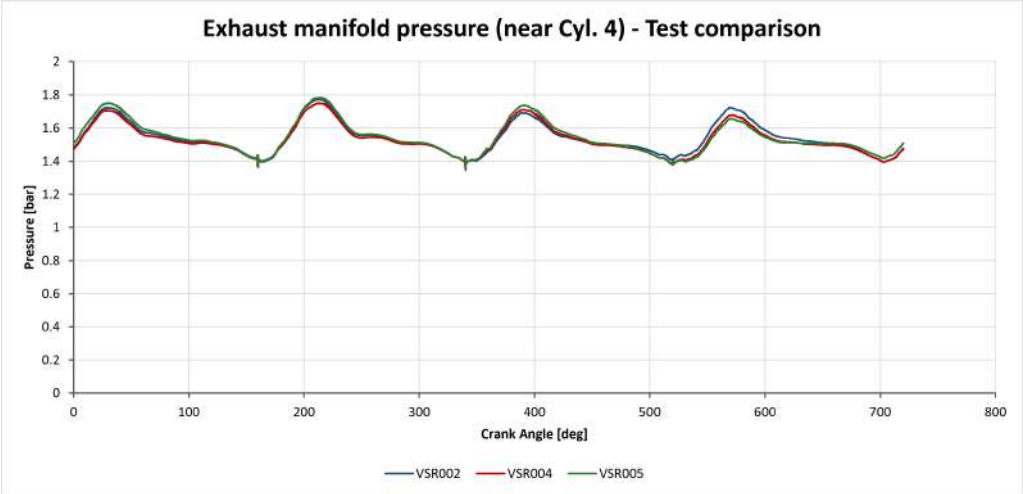


Figure E.10: Comparison of the exhaust manifold pressure traces on cylinder 4 for MP005.

E.2 Check Valve Comparison

E.2.1 Low Load: MP001

At the low-load operating point MP001 (1200 rpm and 3 bar IMEP), the effect of removing the check valve is most clearly visible in the cylinder 4 injection line. With the check valve installed in VSR002, the pressure oscillations generated during the fuel delivery event progressively decay and the line pressure subsequently remains almost constant. In contrast, VSR006 and VSR008 exhibit periodic pressure fluctuations throughout the remainder of the engine cycle. These oscillations repeat approximately every 180 dCA and are consistent with pressure waves from the intake system propagating back into the hydrogen line once the isolation provided by the check valve is removed. The close agreement between VSR006 and VSR008 indicates that this behaviour is mainly caused by the removal of the check valve, while the additional removal of the nozzle has only a limited effect on the line response.

The in-cylinder pressure also increases after removal of the check valve, with VSR006 and particularly VSR008 reaching higher peak pressures than the baseline, while the crank angle position of the maximum remains very similar. This indicates a change in the resulting combustion intensity without a substantial shift in combustion phasing.

The intake manifold pressure traces remain almost coincident for the three configurations at MP001, indicating that the local hardware modifications have little influence on the overall intake pressure at low load. Similarly, the distributor upstream pressure retains the same general periodic behaviour, with only small differences in absolute pressure level. In the exhaust manifold, larger differences appear between some of the individual pressure pulses due to the interaction of the four cylinders in the common manifold. However, in the region associated with the cylinder 4 exhaust event, approximately 550–620 dCA, the differences between the three configurations remain relatively small. Overall, the low load results confirm that the main consequence of removing the

check valve is the loss of pressure isolation between the intake port and the hydrogen line, while the additional removal of the nozzle produces a smaller effect. No clear evidence of pre-ignition, knock, or an isolated intake backfire event is identified from the presented traces.

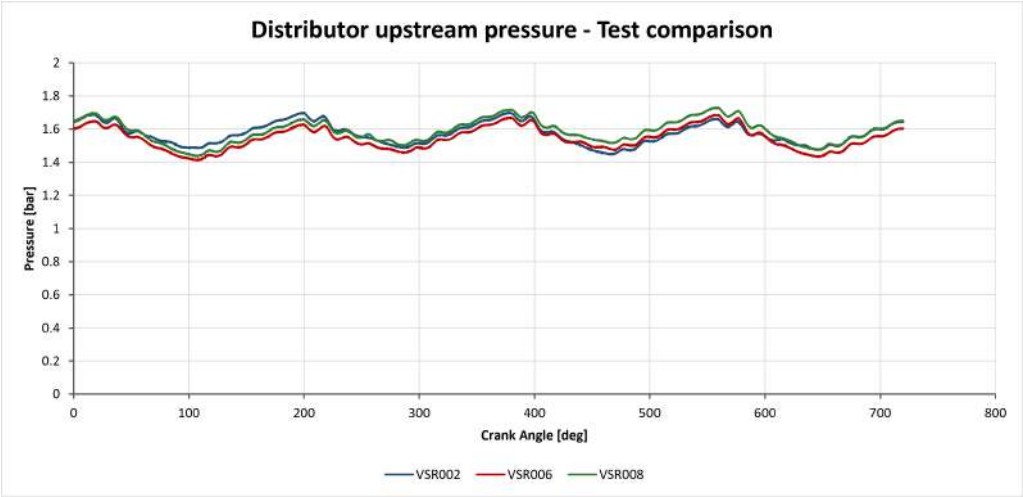


Figure E.11: Comparison of the distributor upstream pressure traces for MP001.

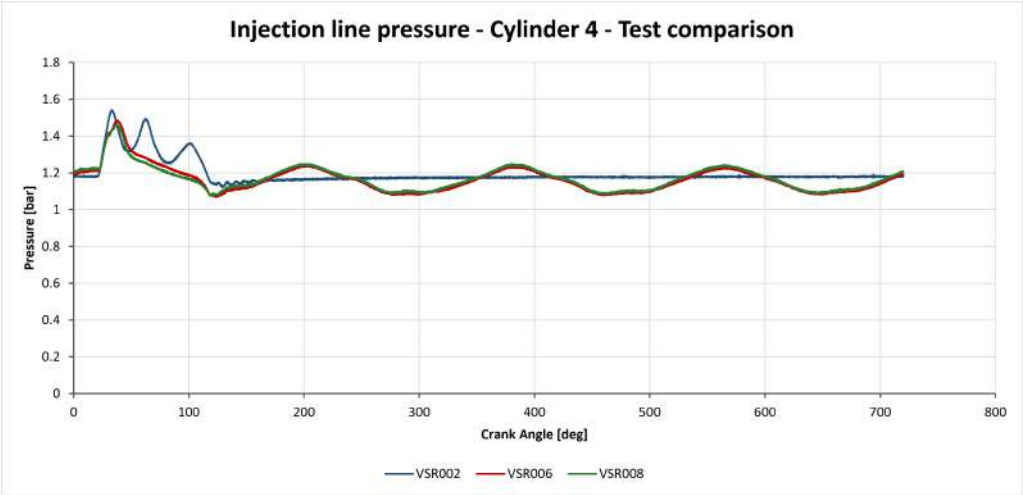


Figure E.12: Comparison of the injection line pressure traces on cylinder 4 for MP001.

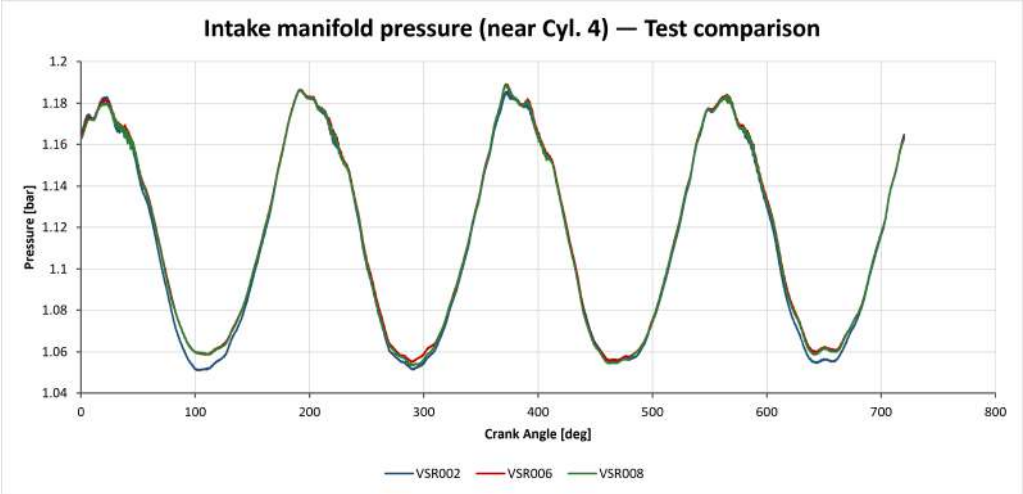


Figure E.13: Comparison of the intake manifold pressure traces on cylinder 4 for MP001.

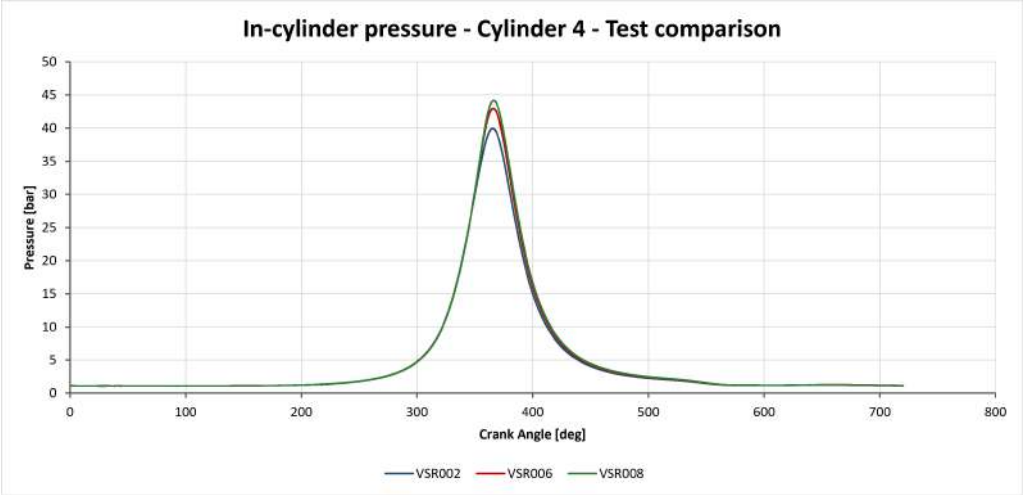


Figure E.14: Comparison of the in-cylinder pressure traces on cylinder 4 for MP001.

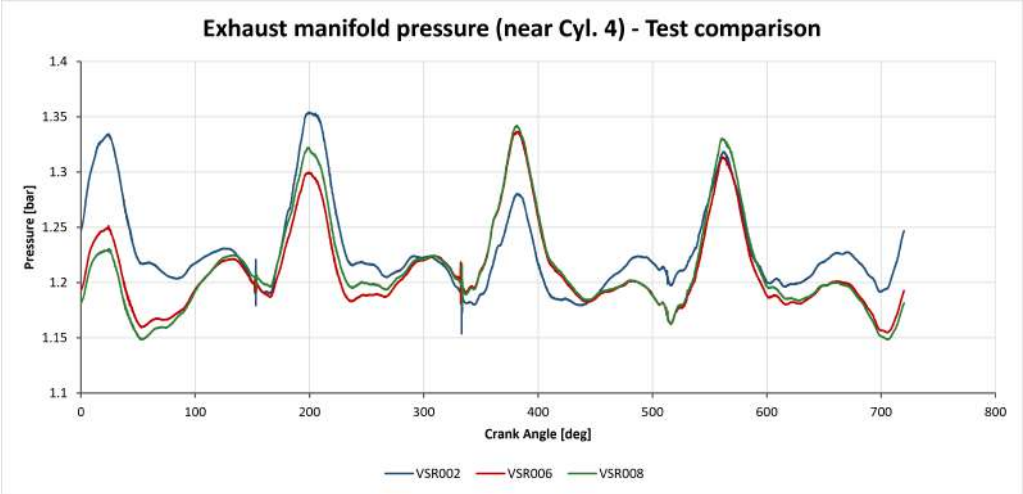


Figure E.15: Comparison of the exhaust manifold pressure traces on cylinder 4 for MP001.

E.2.2 Mid Load: MP005

At the medium-load operating point MP005 (1500 rpm and 6 bar IMEP), the effect of removing the check valve remains clearly visible in the cylinder 4 injection line. After the initial fuel delivery transient, the VSR002 pressure stabilises at an approximately constant level, whereas VSR006 and VSR008 continue to exhibit periodic pressure oscillations throughout the engine cycle. The periodicity of these oscillations is similar to that observed in the intake manifold, supporting the interpretation that removal of the check valve allows intake pressure waves to propagate back into the hydrogen line. The close agreement between VSR006 and VSR008 again indicates that this behaviour results mainly from the removal of the check valve, while the additional removal of the nozzle has a smaller influence.

The in-cylinder pressure also follows the trend observed at the other loads. VSR002 presents the lowest peak pressure, VSR006 reaches a higher value, and VSR008 produces the highest peak, while the crank-angle position of the pressure maximum remains nearly unchanged. The hardware modifications therefore affect mainly the intensity of the resulting combustion rather than producing a substantial change in combustion phasing.

The intake manifold pressure remains slightly higher for VSR002, while VSR006 presents the lowest level and VSR008 an intermediate response. The difference is more evident than at MP001, suggesting that the influence of the modified cylinder branch on the common intake system becomes more relevant as engine load increases. The distributor upstream pressure shows a similar ordering, although the overall periodic behaviour remains unchanged. In the exhaust manifold, the three configurations remain relatively close, including during the pressure pulse associated with the cylinder 4 exhaust event. Overall, the MP005 results confirm the pressure isolation function of the check valve and show that its removal has a greater influence on the fuel line dynamics and combustion response than the additional removal of the nozzle. No clear evidence of pre-ignition, knock, or an isolated intake backfire event is identified from the presented pressure traces.

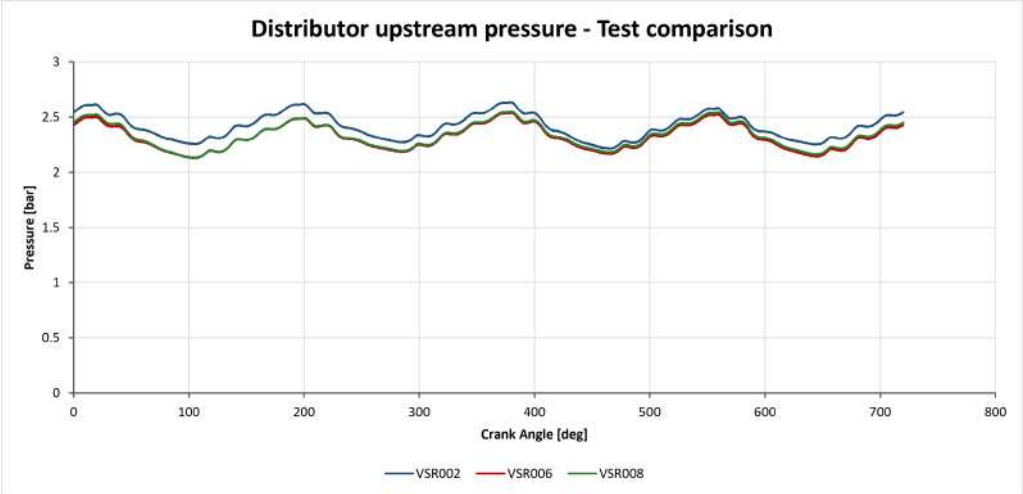


Figure E.16: Comparison of the distributor upstream pressure traces for MP005.

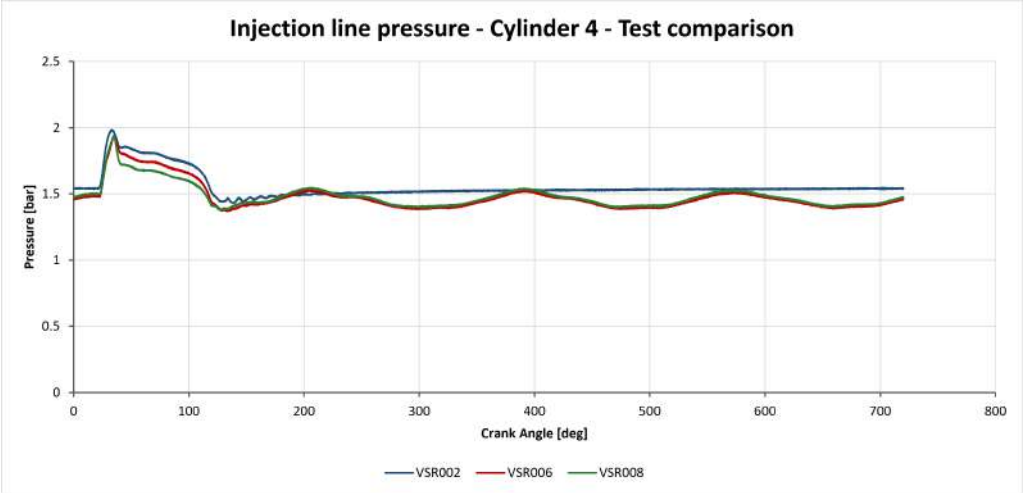


Figure E.17: Comparison of the injection line pressure traces on cylinder 4 for MP005.

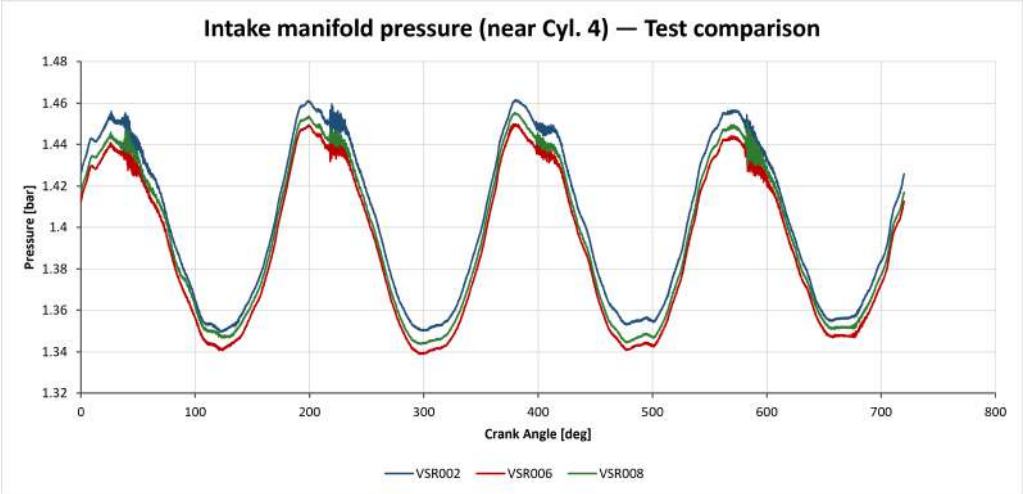


Figure E.18: Comparison of the intake manifold pressure traces on cylinder 4 for MP005.

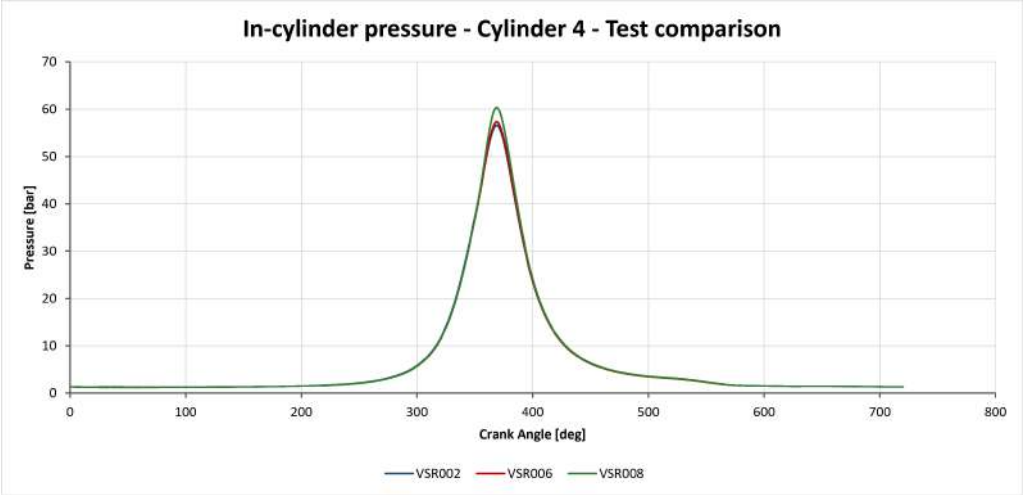


Figure E.19: Comparison of the in-cylinder pressure traces on cylinder 4 for MP005.

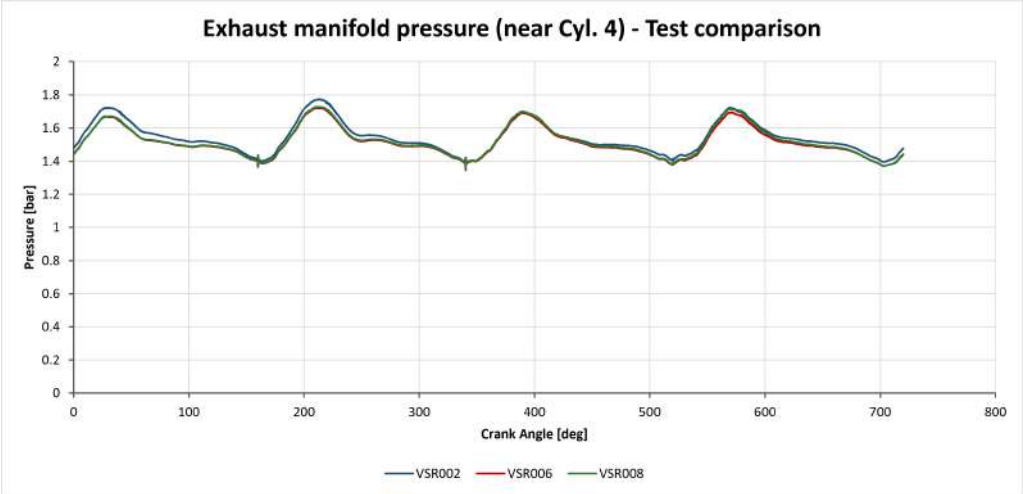


Figure E.20: Comparison of the exhaust manifold pressure traces on cylinder 4 for MP005.

E.3 njection timing Comparison

E.3.1 Low Load: MP001

At the low load operating point MP001 (1200 rpm and 3 bar IMEP), the effect of the later start of injection is clearly visible in the cylinder 4 injection line pressure. The complete fuel delivery pressure transient in VSR009 is shifted by approximately 40 dCA relative to VSR002, in agreement with the change from SOI $= -340$ dCA to SOI $= -300$ dCA. The general oscillatory character of the pressure response remains similar, indicating that the main effect of the timing modification is the displacement of the fuel delivery event rather than a fundamental change in the line dynamics.

The in-cylinder pressure in VSR009 presents a lower maximum than the baseline, while the crank angle position of the pressure peak remains very similar. Therefore, delaying the fuel injection affects the resulting combustion intensity without producing a corresponding 40 dCA shift in the main combustion phasing. This is consistent with the fact that the injection timing controls the preparation of the hydrogen-air mixture before ignition rather than directly defining the ignition event. The later injection also reduces the time available for mixture formation before combustion, which may influence the resulting mixture distribution and combustion development.

A clear reduction in intake manifold pressure is also observed in VSR009 throughout the engine cycle, although the periodic waveform associated with the four cylinders remains similar to the baseline. The distributor upstream pressure shows the expected phase displacement associated with the later fuel demand and also presents differences in absolute pressure level. In the exhaust manifold, VSR009 generally operates at a lower pressure, including during the region associated with the cylinder 4 exhaust event. This behaviour is consistent with the lower combustion pressure observed for VSR009, although the common intake and exhaust manifold measurements also depend on the overall engine and turbocharging operating condition.

Overall, the MP001 results show that delaying the start of injection mainly shifts the fuel delivery event while producing a moderate change in the resulting combustion and gas exchange conditions. No clear indication of pre-ignition, knock, or an isolated intake backfire event is evident from the presented pressure traces.

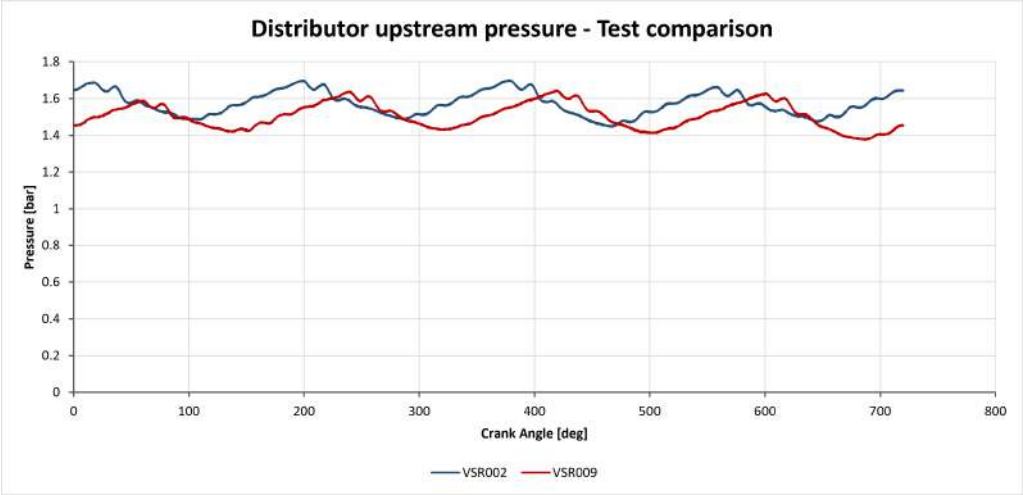


Figure E.21: Comparison of the distributor upstream pressure traces for MP001.

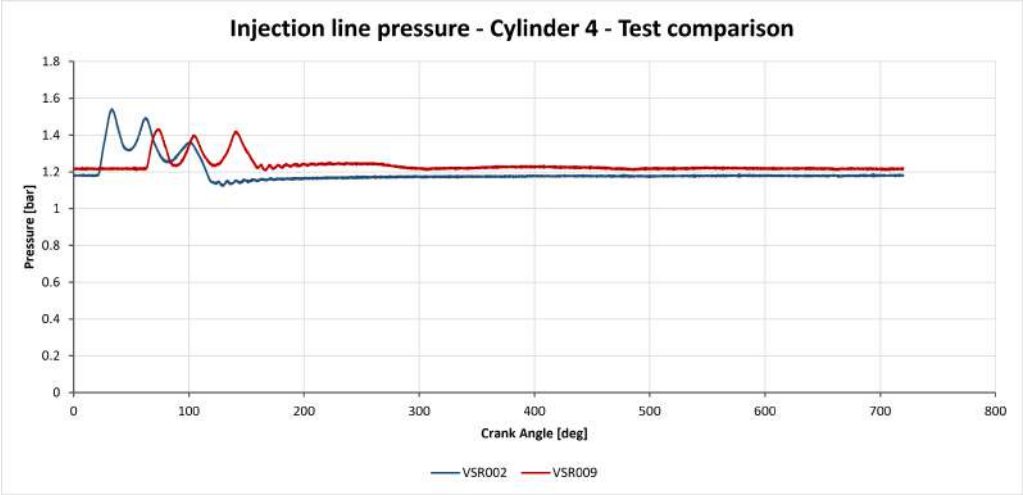


Figure E.22: Comparison of the injection line pressure traces on cylinder 4 for MP001.

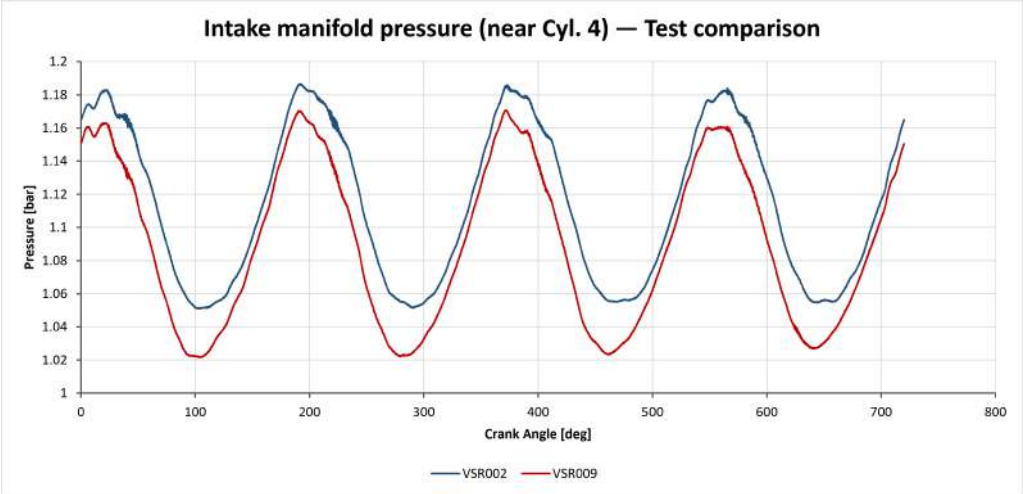


Figure E.23: Comparison of the intake manifold pressure traces on cylinder 4 for MP001.

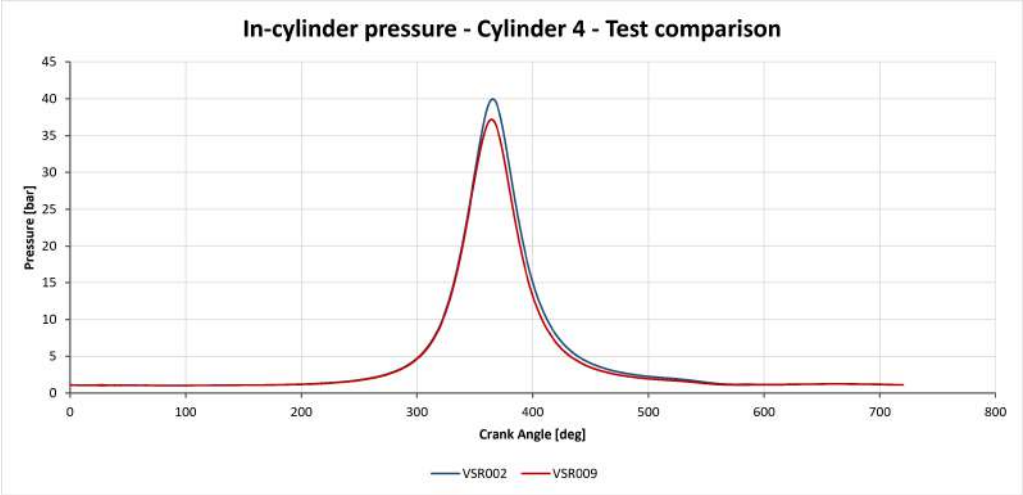


Figure E.24: Comparison of the in-cylinder pressure traces on cylinder 4 for MP001.

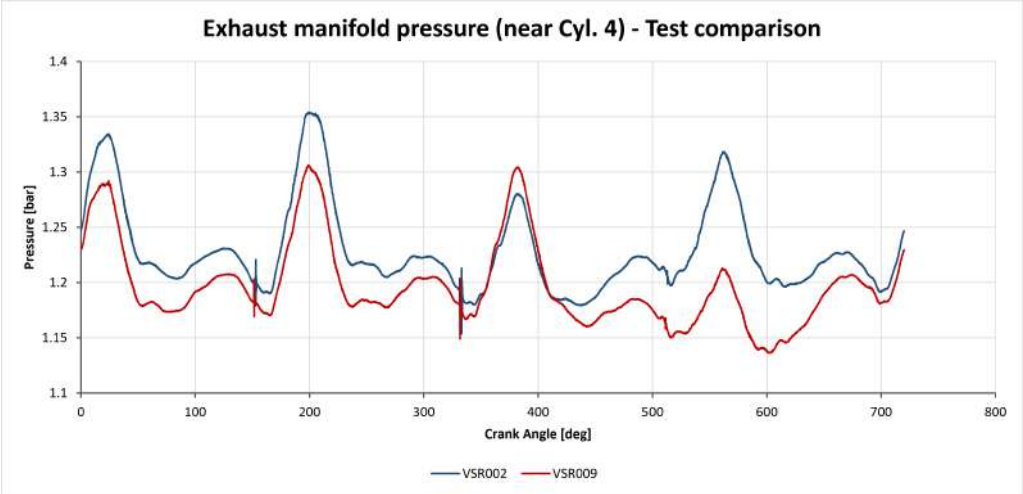


Figure E.25: Comparison of the exhaust manifold pressure traces on cylinder 4 for MP001.

E.3.2 Mid Load: MP005

At the medium-load operating point MP005 (1500 rpm and 6 bar IMEP), the effect of the later start of injection remains clearly visible in the cylinder 4 injection line pressure. The fuel delivery transient in VSR009 is displaced by approximately 40 dCA relative to VSR002, in agreement with the change from SOI $= -340$ dCA to SOI $= -300$ dCA. The general shape of the pressure response remains similar, indicating that the timing modification primarily changes the crank angle position of the injection event rather than the fundamental dynamic behaviour of the line. A corresponding phase displacement is also visible in the distributor upstream pressure, confirming that the later fuel demand affects the pressure response of the common fuel supply.

The in-cylinder pressure remains similar in shape and phasing for both campaigns, but VSR009 reaches a lower maximum pressure than VSR002. The crank-angle position of the pressure maximum remains nearly unchanged, showing that the 40 dCA delay in fuel injection does not produce an equivalent displacement of the main combustion event. The later injection therefore mainly modifies the conditions under which the hydrogen-air mixture is prepared before ignition, while the combustion phasing remains largely controlled by the ignition event.

The intake manifold pressure is consistently lower in VSR009 throughout the engine cycle, while retaining the same periodic structure associated with the four-cylinder intake process. A similar, although smaller, reduction is observed in the exhaust manifold pressure. In the region associated with the cylinder 4 exhaust event, VSR009 also presents a slightly lower pressure contribution, consistent with its lower in-cylinder pressure. Overall, the medium load results support the same behaviour observed at low and high load: delaying the start of injection shifts the fuel delivery event while producing a moderate reduction in intake, combustion, and exhaust pressure levels, without a substantial change in the crank angle position of peak cylinder pressure. No clear indication of pre-ignition, knock, or an isolated intake backfire event is evident from the presented traces.

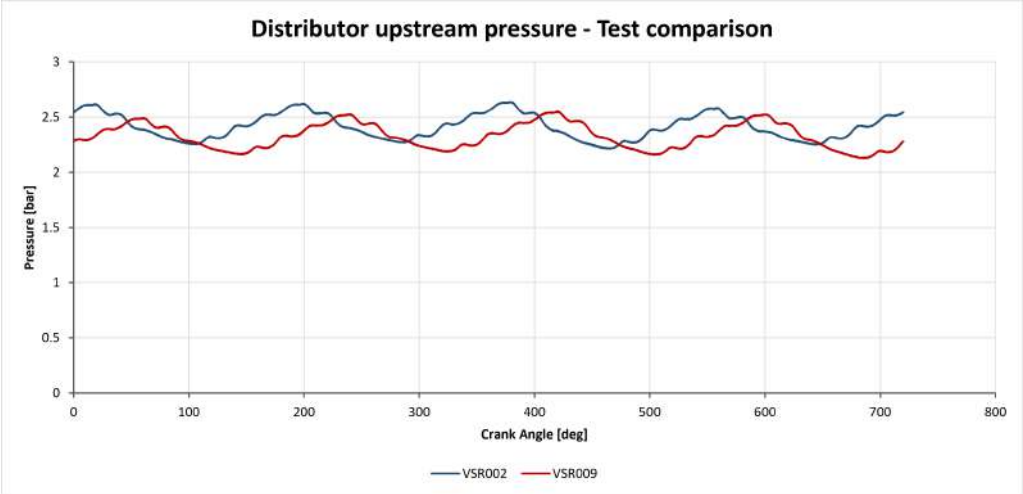


Figure E.26: Comparison of the distributor upstream pressure traces for MP005.

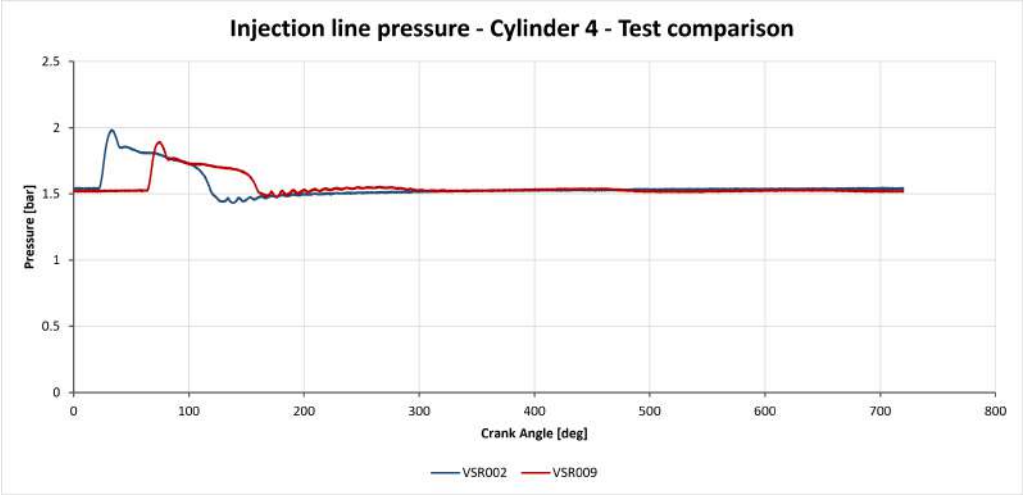


Figure E.27: Comparison of the injection line pressure traces on cylinder 4 for MP005.

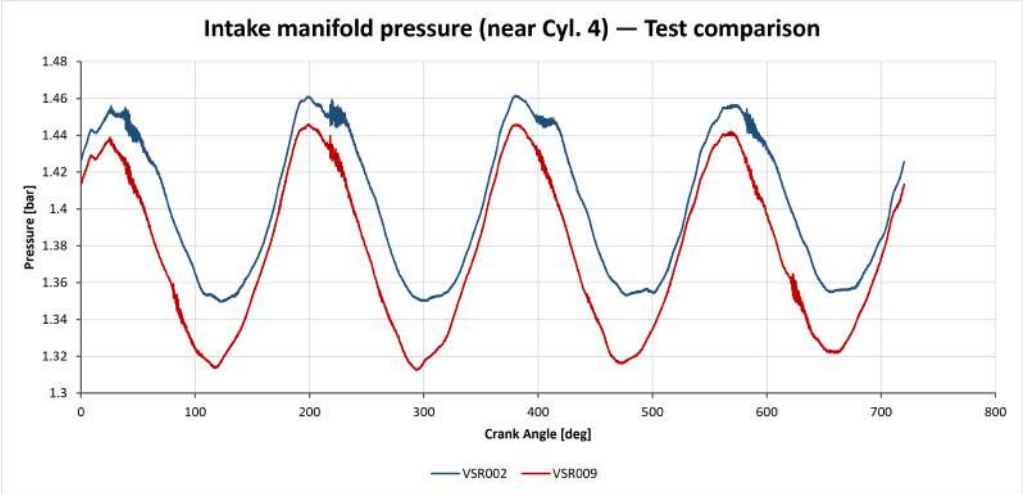


Figure E.28: Comparison of the intake manifold pressure traces on cylinder 4 for MP005.

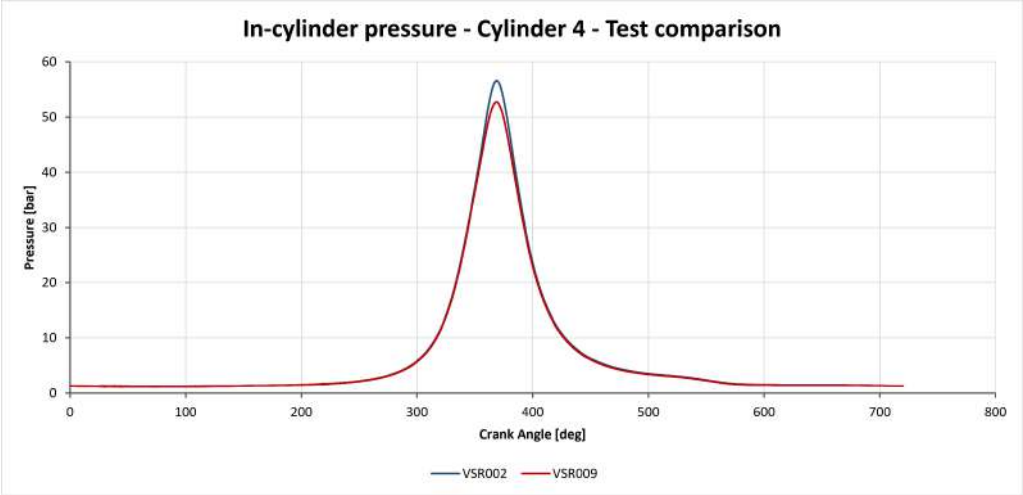


Figure E.29: Comparison of the in-cylinder pressure traces on cylinder 4 for MP005.

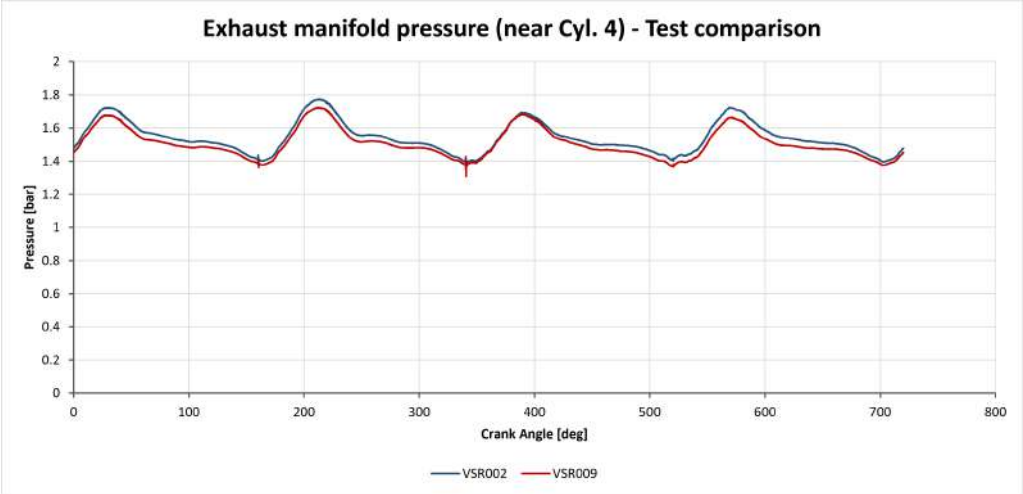


Figure E.30: Comparison of the exhaust manifold pressure traces on cylinder 4 for MP005.